Design and assessment of a Novel Electrically Driven Environmental Control System for More Electric Aircraft

M. A. Popescu 4278372

Delft University of Technology

TU Delft Delft University of Technology

Challenge the future

Design and assessment of a Novel Electrically Driven Environmental Control System for More Electric Aircraft

by

M. A. Popescu 4278372

in partial fulfillment of the requirements for the degree of

Master of Science

in Aerospace Engineering

at the Delft University of Technology,

to be defended publicly on 05.06.2020

Student number:	4278372	
Project duration:	January 15, 2019 – April 15, 2020	
Supervisor:	Dr. ir. R. Vos,	TU Delft
Thesis committee:	Prof. dr. ir. P. Colonna,	TU Delft
	Prof. dr. ir. S. A. Klein,	TU Delft

Cover image made by the author.
An electronic version of this thesis is available at http://repository.tudelft.nl/.

TU Delft

PREFACE

The current research represents the final step towards graduation from Technical University of Delft. During a time span of just more than one year I had the chance to focus my attention to the field of environmental control systems for aircraft applications. The complete process of gathering literature data, setting up simulation models for electrically driven air cycle machine systems as well as for vapour cycle refrigeration units, verifying the models using uncertainty analysis, validating models using experimental data and analysing results has been a strong foundation for my upcoming career in the aerospace industry. I hope the work performed can be valuable for future students wishing to pursue a thesis in the field of environmental control systems.

I would like to thank my supervisor dr. ir. Roelof Vos for his support and guidance provided throughout the various steps of the master thesis. I would like to also thank prof. dr. ir. P. Colonna and prof. dr. ir. S. A. Klein for being part of the thesis committee. Finally I would like to mention Phd students Andrea Giuffré and Federica Ascione for the time spent together discussing different aspects of environmental control systems.

Mihai Adrian Popescu
Delft - 13 May, 2020

SUMMARY

The significant impact of airborne cabin pressurisation and cooling systems on fuel consumption requires new technologies to be investigated. In the pursuit of decreasing fuel consumption while leveraging on the benefits of electrification, a shift was initiated from conventional bleed air driven to electric powered air cycle machines based environmental control systems. The performed research goes a step further by considering an alternative configuration in the form of an electric driven vapour cycle refrigeration unit. The system to be installed onboard a technology demonstrator is integrated at aircraft level and its impact on fuel consumption is compared to that of an electrically driven air cycle machine.

The starting point in designing environmental control systems represents setting up the boundary conditions of the system and identifying the cooling load. The latter can be estimated by means of a cabin heat model for which the contributions due to convection, conduction and radiation are considered allowing to quantify the total heat load to be removed by the environmental control system. The two environmental control systems can be sized according to the duty load which was estimated at 46.3 kW for ground operations and 40.4 kW for the cruise flight segment. In case of the vapour cycle system the corresponding refrigerant mass flow rate to meet the desired cooling duty ranges between 0.30 and 0.34 kg/s for a system using R134a refrigerant.

By means of a sensitivity study using the Morris One at a Time (MOAT) approach the system parameters belonging to each architecture were classified as either having a large impact on results or being negligible. The cabin air compressor exit pressure as well as the cabin pressure requirement were identified as parameters having large linear effect on results for both models. In case of the vapour cycle system the refrigerant mass flow rate was identified as the critical parameter having large linear effects on trip fuel. This was expected as the cooling effect to be provided by the evaporator during the latent heat transfer is a function of refrigerant mass flow rate. To make sure the systems respond correctly to varying secondary shaft power extractions required to drive the electric cabin air compressors and the refrigerant compressor, a sensitivity study of the shaft power off-takes was performed and data was validated using an alternative engine performance deck.

The aim of this research is to assess the efficiency of the novel system when integrated at aircraft level as compared to the baseline model. Analysing the performance of the two models from a thermodynamic point of view was done by quantifying their coefficient of performance. As expected the vapour cycle system resulted in a higher coefficient of performance than the air cycle machine for both ground and cruise operations when taking into account the effects of cabin air compressor pressurisation and ram air work, reaching a value of 0.28 during cruise flight operation mode as compared to the 0.12 obtained for the baseline model. Analysing the vapour cycle system as a standalone unit and neglecting effects of pressurisation, a local coefficient of performance of 2.05 was estimated. This value is essential in case the performance of the system has to be compared with other commercially available refrigeration units for ground applications which incorporate both subcooling and superheating.

Fuel consumption related results show up to 1.62 % trip fuel reduction for a baseline mission of 1000 nm and 12000 kg payload for the technology demonstrator aircraft equipped with the vapour compression cycle refrigeration system as compared to the baseline model. Even when accounting for a weight penalty of 150 kg associated with the novel system, the results show a trip fuel reduction of 1.48 %, still indicating that the vapour cycle system is more efficient than the conventional air cycle machine.

The performed study is an essential step towards a system configuration using promising technologies such as miniature centrifugal compressors. According to an investigation taking into account the required mass flow rate of approximately 0.3 kg/s and pressure ratio of 5.5 needed to meet the cooling load requirements, it was determined that using a single miniature centrifugal compressor is unfeasible. Even at high rotational speeds in excess of 250,000 rpm, the mass flow rate of such a compressor is in the range of 1 to 20 g/s while its pressure ratio can hardly reach a value of 2. This highlights the need to consider multi-stage cycles in order to determine if the weight of additional heat exchangers and piping can be offset by the weight savings associated with miniature compressors.

CONTENTS

Preface ii

Summary iv

List of Figures vii

List of Tables x

Nomenclature xii

1 Introduction 1

2 Background information 3
- 2.1 More electric aircraft technologies . . . 3
  - 2.1.1 Propulsion system configuration . . . 3
  - 2.1.2 Electric power system architectures . . . 6
- 2.2 Environmental control systems configurations . . . 8
  - 2.2.1 Air cycle applications . . . 8
  - 2.2.2 Vapour cycle applications . . . 13
  - 2.2.3 Hybrid air/vapour cycle applications . . . 14
- 2.3 Thermodynamic cycles for refrigeration systems . . . 16
  - 2.3.1 Overview of vapour compression refrigeration cycles . . . 16
  - 2.3.2 Reverse Carnot cycle . . . 16
  - 2.3.3 Ideal vapour compression cycle . . . 17
  - 2.3.4 Advanced vapour compression cycles . . . 18
  - 2.3.5 Refrigerant selection and thermophysical modelling methods . . . 21

3 Methodology 23
- 3.1 Requirements engineering . . . 23
- 3.2 System level modelling . . . 24
- 3.3 Heat load analysis . . . 32
- 3.4 Electrical loads analysis . . . 33
- 3.5 Point performance analysis . . . 35

4 Verification and Validation 37
- 4.1 Sensitivity studies using MOAT method . . . 37
  - 4.1.1 Sensitivity study for baseline model system architecture . . . 38
  - 4.1.2 Sensitivity study for technology demonstrator system architecture . . . 40
- 4.2 Sensitivity study of engine off-takes . . . 41
- 4.3 Validation of vapour cycle system . . . 43
  - 4.3.1 Validation of evaporator model . . . 43
  - 4.3.2 Validation of condenser model . . . 43
- 4.4 Validation of air cycle system . . . 44

5 Results 47
- 5.1 Heat load analysis . . . 47
- 5.2 Thermodynamic cycle analysis . . . 48
  - 5.2.1 Baseline model . . . 48
  - 5.2.2 Technology demonstrator . . . 49
- 5.3 Electric load analysis . . . 53
  - 5.3.1 Baseline model . . . 54
  - 5.3.2 Technology demonstrator . . . 54
  - 5.3.3 Comparison . . . 54

5.4 Trip fuel comparison . . . 55
5.4.1 First set of results . . . 55
5.4.2 Effect of assumptions on results . . . 55
5.4.3 Effect of weight penalty . . . 56

6 Conclusions **59**

7 Recommendations **61**
7.1 Mass flow rate requirement . . . 61
7.2 Pressure ratio requirement . . . 61
7.3 Proposed system to be investigated . . . 61

Appendices **63**

A Reference data Refrigerant R134a **63**

B Additional results **69**
B.1 Thermodynamic analysis of simple VCS . . . 69
B.2 Flight mission profile data . . . 70

C Reference data refrigerant compressors **71**

D Reference data applications of vapour cycle systems in aircraft **75**

E Sysarc Knowledge Designer **77**
E.1 Positioning EO concepts . . . 77
E.2 Argument notation: method vs function . . . 77
E.3 Heat transfer methods . . . 78
E.4 Calculations of specific enthalpy of saturated fluid (hf) and gas (hg) . . . 79

Bibliography **81**

List of Figures

2.1 RB211 - front view [Own photo - taken on November 17, 2017 at Royal Air Force Museum Cosford] 4
2.2 RB211 - back view [Own photo - taken on November 17, 2017 at Royal Air Force Museum Cosford] . . . 4
2.3 Bleed system [1] . . . 4
2.4 Bleed air extraction system architecture [2, p. 244] . . . 5
2.5 Secondary power usage: conventional versus electrical subsystem architectures [3] . . . 6
2.6 Constant frequency generator configuration [4] . . . 6
2.7 Variable frequency generator configuration [4] . . . 6
2.8 Air cycle machines [5] . . . 8
2.9 Low pressure water separator [6, p. 569] . . . 9
2.10 High pressure water separator - extraction loop [7] . . . 10
2.11 High pressure water extractor [8] . . . 10
2.12 McDonnel Douglas DC-10 ECS: Three wheel bootstrap with low pressure water separator [6, p. 574] . . . 11
2.13 A321 ECS: Three wheel bootstrap with high pressure water separator [9, p. 1199] . . . 11
2.14 Boeing 777 ECS: Four wheel bootstrap with high pressure water separator [10] . . . 12
2.15 Schematic layout of state-of-the-art electrically driven environmental control system based on traditional air cycle technology - Boeing 787 application [11] . . . 13
2.16 Boeing 707 ECS: Refrigeration unit [12, p. 22] . . . 14
2.17 Hybrid system patent [13] . . . 14
2.18 Hybrid system for military applications [14] . . . 15
2.19 Variation of coefficient of performance with cycle options [15] . . . 16
2.20 Reverse Carnot cycle [16, p. 29] . . . 17
2.21 Ideal vapour compression cycle including the components of the system (top side of figure) as well as the associated T-S and p-h diagrams (bottom side of figure) [16, p. 30] . . . 18
2.22 VCS with SLHX [15] . . . 19
2.23 Expander cycle [15] . . . 20
2.24 Ejector cycle [15] . . . 20
2.25 Multistage cycle [17] . . . 20

3.1 Baseline model . . . 23
3.2 Technology demonstrator . . . 23
3.3 Sysarc 3D view showing the cabin discretisation in three zones, arrangement of pathways and localisation of components . . . 24
3.4 Integration of baseline model electrically driven air cycle machine at aircraft level . . . 25
3.5 Electrically driven air cycle machine based ECS main components and localisation of critical points along the cycle . . . 25
3.6 Pressure-enthalpy diagram of reverse Brayton air cycle machine refrigeration system with localisation of critical points along the cycle . . . 25
3.7 Air cycle machine rotor system, copied from [18] . . . 26
3.8 Integration of vapour cycle system at aircraft level . . . 28
3.9 Vapour cycle refrigeration system main components and localisation of critical points along the cycle . . . 28
3.10 Pressure-enthalpy diagram of vapour cycle refrigeration system with localisation of critical points along the cycle . . . 28
3.11 Condenser approach diagram . . . 29
3.12 Evaporator approach diagram . . . 29
3.13 Cabin heat transfer model, adapted from Chakraborty et al. [19] . . . 32
3.14 Free body diagram showing forces acting on aircraft during ground operations, copied from [20] 35
3.15 Free body diagram showing forces acting on aircraft during flight operations, copied from [20] . 35

3.16 Altitude variation with time . . . 36

4.1 Sensitivity study for baseline model, analysing impact on the variable trip fuel . . . 39
4.2 Sensitivity study for baseline model, analysing impact on the variable trip fuel . . . 40
4.3 Sensitivity study for technology demonstrator, analysing impact on trip fuel . . . 41
4.4 Sensitivity study for technology demonstrator, analysing impact on trip fuel . . . 41
4.5 Variation of specific fuel consumption with secondary shaft power off-takes . . . 42
4.6 Variation of SFC correction factor with secondary shaft power off-takes . . . 43
4.7 T-s diagram air cycle machine . . . 44

5.1 Baseline model p-h diagram for operation at ground hot day . . . 48
5.2 Baseline model p-h diagram for operation at cruise hot day . . . 49
5.3 Pressure-enthalpy diagram for a simple VCS with evaporation temperature of 0° Celsius and condensation temperature of 58° Celsius (with isentropic compressor) $h_2 = 447.7$ kJ/kg . . . 50
5.4 Pressure-enthalpy diagram for a superheated VCS with evaporation temperature of 0° Celsius, condensation temperature of 58° Celsius and a superheat value of 10° Celsius . . . 51
5.5 Pressure-enthalpy diagram for a subcooled VCS with evaporation temperature of 0° Celsius, condensation temperature of 58° Celsius and a subcool value of 10° Celsius . . . 52
5.6 Pressure-enthalpy diagram for a superheated and subcooled VCS with evaporation temperature of 0° Celsius, condensation temperature of 58° Celsius, a superheat value of 10° Celsius and a subcool value of 10° Celsius (with isentropic compressor) . . . 53
5.7 Secondary shaft power extraction variation with mission timeline . . . 54
5.8 Delta trip fuel comparison, initial set of results . . . 55
5.9 Delta trip fuel comparison accounting for the effect of a reduced cabin air compressor exit pressure in case of the baseline model . . . 56
5.10 Delta trip fuel comparison accounting for the effect of weight penalty of 150kg applied to the VCS model . . . 57

7.1 VCS schematic proposal with a number of n miniature centrifugal compressors placed in parall and a number of m placed in series . . . 62

A.1 R134a refrigerant properties from -100 ° to 2 ° Celsius , adapted from ASHRAE 2017 Fundamentals (SI Edition) [16, p. 812] . . . 63
A.2 R134a refrigerant properties from 4 ° to 100 ° Celsius, adapted from ASHRAE 2017 Fundamentals (SI Edition) [16, p. 812] . . . 64
A.3 R134a Pressure-Enthalpy diagram, copied from ASHRAE 2017 Fundamentals (SI Edition) [16, p. 811] . . . 65
A.4 R134a refrigerant properties: constant pressure table (superheated refrigerant table) at 290 kPa (2.9 bar) . . . 66
A.5 R134a refrigerant properties: constant pressure table (superheated refrigerant table) at 1600 kPa (16 bar) . . . 67

B.1 Pressure-enthalpy diagram for a simple VCS with evaporation temperature of 0° Celsius and condensation temperature of 58° Celsius (with compressor isentropic efficiency 75%) $h_2 = 464$ kJ/kg . . . 69
B.2 Temperature-entropy diagram for a simple VCS with evaporation temperature of 0° Celsius and condensation temperature of 58° Celsius (with compressor isentropic efficiency 75%) . . . 69
B.3 Mach number variation with time . . . 70
B.4 Total propulsive power variation with time . . . 70

C.1 Compressor map for dual stage miniature centrifugal compressor with impeller diameter of 35mm, corresponding to Compressor #1 from Table C.1, copied from Krahenbuhl et al. [21] . . . 72
C.2 Compressor map for single stage miniature centrifugal compressor with impeller diameter of 21mm, corresponding to Compressor #4 from Table C.1, copied from Casey et al. [21] . . . 72
C.3 Compressor map for single stage miniature centrifugal compressor with impeller diameter of 21mm, corresponding to Compressor #5 from Table C.1, copied from Zhao et al. [22] . . . 73

C.4 Power map for single stage miniature centrifugal compressor with impeller diameter of 21mm, corresponding to Compressor #5 from Table C.1, copied from Zhao et al. [22] 73
C.5 Centrifugal compressor assembly [21] 74
C.6 Impeller with diameter of 21 mm and length of 69 mm [21] 74
C.7 Scroll compressor assembly and specifications 74

E.1 Components_Pneumatic accessable through SysArcDataStructure 77
E.2 CalcNTU method arguments 78
E.3 CalcNTU method statements 78

List of Tables

2.1 Literature review - contribution types and main aspects . . . 3
2.2 GEnx platform engine options - geometric and performance specifications . . . 5
2.3 Power ratings for constant frequency generators [4] . . . 7
2.4 N1 and N2 speed variations [4] . . . 7
2.5 Types of environmental control systems using air cycle machines [23] . . . 9
2.6 Thermo-physical properties of various refrigerants [17] . . . 21

3.1 Summary of simulated conditions . . . 24
3.2 Critical points along the electrically driven air cycle machine ECS . . . 25
3.3 Critical points along the vapour compression cycle refrigeration system . . . 28
3.4 Summary of parameters used in heat load budget calculations . . . 33

4.1 Sensitivity study data for baseline model . . . 38
4.2 Sensitivity study data for technology demonstrator model (VCS) . . . 40
4.3 Shaft power off-takes sensitivities on specific fuel consumption . . . 42
4.4 Validation data for both the condenser and evaporator models . . . 43
4.5 Validation data for air cycle machine pressure level at inlet . . . 44
4.6 Air cycle machine matching data . . . 45

5.1 Heat load budget . . . 47
5.2 Baseline model thermodynamic analysis . . . 48
5.3 Coefficient of performance calculations for baseline model . . . 49
5.4 Pressure and enthalpy data for a simple VCS with evaporation temperature of 0° Celsius and condensation temperature of 58° Celsius . . . 49
5.5 Refrigerant compressor performance data for a simple VCS cycle for two operation modes: ground and cruise . . . 50
5.6 Coefficient of performance calculations for technology demonstrator equipped with simple VCS 50
5.7 Pressure and enthalpy data for a superheated VCS with evaporation temperature of 0° Celsius, condensation temperature of 58° Celsius and a superheat value of 10° Celsius . . . 51
5.8 Pressure and enthalpy data for a subcooled VCS with evaporation temperature of 0° Celsius, condensation temperature of 58° Celsius and a subcool value of 10° Celsius . . . 51
5.9 Pressure-enthalpy diagram for a superheated and subcooled VCS with evaporation temperature of 0° Celsius, condensation temperature of 58° Celsius, a superheat value of 10° Celsius and a subcool value of 10° Celsius . . . 52
5.10 Refrigerant compressor performance data for an advanced VCS cycle with evaporation temperature of 0° Celsius, condensation temperature of 58° Celsius, a superheat value of 10° Celsius and a subcool value of 10° Celsius. Data for two operation modes: ground and cruise . . . 53
5.11 Coefficient of performance calculations for technology demonstrator equipped with an advanced VCS with evaporation temperature of 0° Celsius, condensation temperature of 58° Celsius, a superheat value of 10° Celsius and a subcool value of 10° Celsius. Data for two operation modes: ground and cruise . . . 53
5.12 Secondary power off-takes and electrical power demand during cruise flight segment . . . 55
5.13 Trip fuel comparison results with baseline model air cycle system running at $P_{cac,exit}$=2.75 bar . 55
5.14 Trip fuel comparison results with baseline model air cycle system running at $P_{cac,exit}$=1.73 bar . 56
5.15 Trip fuel comparison results with baseline model air cycle system running at $P_{cac,exit}$=2.75 bar . 56

B.1 Mission profile parameters summary . . . 70

C.1 Reference data compressors (miniature and small scale) . . . 71

D.1 Vapour cycle systems applications, data adapted from Springer and Delson [24] . . . 75

E.1 Matching arguments between method and function 78
E.2 Method to compute HXHeatTransfered 78
E.3 Method to compute HXPackHeatCapacityRate 79
E.4 Method to compute HXCoolantHeatCapacityRate 79
E.5 Formula used to compute specific enthalpy at evaporation dew point (h1s) 79
E.6 Formula used to compute specific enthalpy at condensation dew point (h2s) 80
E.7 Formula used to compute specific enthalpy at condensation bubble point (h3s) 80
E.8 Method used to compute massic enthalpy of refrigerant 80

NOMENCLATURE

LIST OF SYMBOLS

A	Area	$[m^2]$
c_p	Specific heat capacity at constant pressure	[kJ/(kg.K)]
c_v	Specific heat capacity at constant volume	[kJ/(kg.K)]
C	Heat capacity rate	[W/K]
C_L	Lift coefficient	[-]
C_D	Drag coefficient	[-]
ΔC_D	Drag coefficient increment	[-]
d_i	Elementary effect	[-]
D	Aerodynamic drag force	[N]
D_g	Ground drag force	[N]
g	Acceleration of gravity	$[m/s^2]$
h	Specific enthalpy	[kJ/kg]
k	Correction factor for drag coefficient calculation	[-]
L	Aerodynamic lift force	[N]
$\dot{m}$	Mass flow rate	[kg/s]
p	Pressure	[bar,MPa]
q"	Solar irradiance	$[W/m^2]$
$\dot{Q}$	Cooling capacity	[kW]
s	Specific entropy	[kJ/(kg.K)]
S	Surface area	$[m^2]$
T	Temperature	[°Celsius]
U	Overall heat transfer coefficient	$[W/(m^2.K)]$
V	Velocity	[m/s]
$\dot{W}$	Power	[kW]
x	Vapour quality	[-]

List of Greek symbols

α	Angle of attack	[°]
Δ	Change	[%]
β	Pressure ratio	[-]
ϵ	Recirculation ratio	[-]
ρ	Density	$[kg/m^3]$
η	Efficiency	[%]
σ	Standard deviation	[-]
μ	Mean	[-]
γ	Flight path angle	[°]

List of subscripts

amb	Ambient
cab	Cabin
c	Compressor
conv	Convection
cond	Condenser
evap	Evaporator
ef	Effective
f	Saturated fluid
g	Saturated gas
H	High pressure side
L	Low pressure side
is	Isentropic
pax	Passengers
P	Metabolic
rec	Recovery
recirc	Recirculation
r	Refrigerant
s	Saturation
s'	Iradiation
t	Turbine
wall	Fuselage wall

List of abbreviations

APD	Aircraft preliminary design
ATD	Approach temperature difference
APU	Auxiliary power unit
CAC	Cabin air compressor
CAS	Calibrated air speed
COP	Coefficient of performance
EA	Engine Alliance
ECS	Environmental control system
EO	Engineering object
FAA	Federal aviation administration
FAR	Federal aviation regulations
GE	General Electric
HX1	Primary heat exchanger
HX2	Secondary heat exchanger
IEC	International electrotechnical commission
IAE	International aero engines
IFE	In-flight entertainment
ISA	International standard atmosphere
MOAT	Morris one at a time
NEMA	National electrical manufacturers association
PACK	Pneumatic air conditioning kit
PW	Pratt and Withney
ROC	Rate of climb
ROD	Rate of descent
SFC	Specific fuel consumption
SLHX	Suction line heat exchangers
VCS	Vapour cycle system
US	United states

1

INTRODUCTION

Technological advancements in the aerospace market are continuously evolving with one of the key drivers being the research performed at various institutions around the world. Based on a collaboration between the Power and Propulsion group at Delft University of Technology and the Dutch supplier of aerospace components Aeronamic, a research project regarding the design and development of a new environmental control system (ECS) for more electric aircraft is currently underway. The novelty of this project revolves around the proposed configuration: a refrigeration system based on the vapour compression cycle in combination with a bleedless propulsion architecture. While Aeronamic is currently developing the high speed motor driven electric compressor to be used in the vapour compression cycle, the research performed at Delft University is aimed at configuring the overall system, quantifying the resulting performance related characteristics and analysing the feasibility of the proposed set-up.

The relevance and context of work at academic and applied level build on the foundation set by Eichler in 1875 who conducted one of the first simulations of an environmental control system for aircraft [25]. The proposed work can be closely linked to the fields of modelling and simulation based engineering which are also employed at applied level by manufacturers that seek to optimise their designs through simulations rather then experiments in order to reduce costs. Since the compressor to be used in the new configuration is provided by an industry supplier of aerospace components, the research outcome is capable of providing insight into possible applications of the newly developed product and thus helping the supplier company become more attractive to new potential customers. Due to the expected decrease in specific fuel consumption resulting from integrating the novel environmental control system at aircraft level, the proposed configuration has the potential to partially fulfil some of the requirements set by the European Commission for 2050, namely a 75% reduction in $C0_2$ emission per passenger kilometre and a 90% reduction in NO_x emissions and a 65 % reduction in noise compared to a baseline aircraft of year 2000 [26].

Several approaches can be thought of in order to keep under control the increased emissions and noise associated with the estimated growth of air traffic. While other studies focus on redesigning the architecture of the propulsion system by implementing hybrid electric powertrains, the focus of the current paper is to consider the environmental control system, the dominant user of secondary power onboard commercial aircraft. As the gap between the industry standard's conventional air cycle machines and the electrically driven air cycle machine was closed with the advent of the Boeing 787, it is time to go one step further and determine the feasibility of a novel environmental control system in the form of a vapour cycle compression refrigeration unit aimed towards the Airbus A320 platform.

Designing airborne refrigeration systems provides endless possibilities in terms of refrigeration medium, compressor type and architecture set-up. For the present research the design choice is fixed around a centrifugal compressor running a simple loop vapour compression cycle with R134a refrigerant. The challenge of interest represents integrating the refrigeration unit at aircraft level and making sure the system is feasible from a thermodynamic point of view. Ultimately the goal is to set-up a baseline model running an electrified air cycle machine unit and compare its performance metrics such as energy consumption and associated trip fuel for a baseline mission of 1000 nm and 12000 kg payload with those of a technology demonstrator aircraft running the vapour cycle refrigeration unit.

The following part of the thesis commences with the background information section providing a strong fundamental background about more electric aircraft technologies, electric power system architectures, environmental control systems configurations, thermodynamic cycles for refrigeration systems, advanced vapour compression cycles and refrigerant selection criteria. The methodology section contains a concise overview

of subsystem modelling and integration at aircraft level, providing the reader with the foundation required to understand the basic principles behind the two simulation models. Also part of the methodology are a heat load analysis and an electric load analysis which are invaluable tools when considering the design of refrigeration systems from an aircraft level. In the verification and validation section the sensitivities of the powerplant due to secondary power off-takes is presented, followed by the validation of the refrigeration unit itself. The results section aims to provide enough data required to answer the research questions, including quantification of secondary power extractions as well as comparison plots of fuel consumption between the baseline model and technology demonstrator. The report ends with the conclusion section based on the available data, aiming at summarising the key points of the work performed as well as providing recommendations for future research.

The research objective of the current design oriented research is defined by accounting for how different theories on environmental control systems, refrigeration cycles and more electric aircraft can be combined to support the design of a novel environmental control system and its integration at aircraft level. The starting point is looking at research methods that can be utilised as part of a thermal design methodology for aircraft thermal systems. Other aspects to be considered are the technologies related to propulsion configuration and electrical power systems having a direct impact on the functioning of the environmental control system. Additionally it is important to identify the mutual dependencies arising from coupling or decoupling the cooling, heating and pressurisation functions of the environmental control system. Following the previously mentioned steps helps to provide the required tools required to investigate how can a vapour compression refrigeration cycle be integrated into the environmental control system taking into account industry standards and certification requirements, allowing to define the following *research objective*:

"The objective of this research project is to contribute to the development of a complex subsystem for more electric aircraft by designing a new environmental control system based on the vapour compression cycle in combination with a bleed-air-free propulsion system and assessing the resulting performance benefits at aircraft level in terms of specific fuel consumption and potential trip fuel savings."

The *research questions* to be answered are the following:

1. What are the effects on aircraft performance associated with operating an electrically driven bleed-air-free air cycle system based environmental control system at aircraft level?
   (a) Which parameters have a large effect on results and which are negligible?
   (b) What are the implications of operating the refrigeration system under various conditions?
   (c) What is the trip fuel for a common design mission?
2. What are the effects on aircraft performance resulting from the integration of an electrically driven bleed-air-free vapour compression cycle based environmental control system at aircraft level?
   (a) What is the impact on the specific fuel consumption when varying the electrical power off-takes from the engine?
   (b) What are the implications of operating the refrigeration system under various conditions?
   (c) What is the impact on the trip fuel when replacing a conventional electrically driven air management system with an electrically driven vapour cycle refrigeration system?

2

BACKGROUND INFORMATION

The process of designing a novel system can only commence once the existing body of knowledge is identified and thoroughly understood. Table 2.1 provides a consolidated view of the various contributions analysed during the literature review, highlighting the main aspects relevant to the proposed research. The various contributions can be classified as modelling and simulation studies, optimisation studies, experimental studies, methodology articles and review articles.

Table 2.1: Literature review - contribution types and main aspects

Type of contribution	Main aspects
Modelling and simulation studies	• Mathematical models of components (energy or exergy based) • Simulation methods for vapour cycle systems
Optimisation studies	• Working fluid selection and impact on coefficient of performance • Thermodynamics optimum of heat exchangers • Novel control methods
Experimental studies	• Validation examples of air and vapour cycle based systems • Static and dynamic tests
Methodology articles	• Integration of novel subsystem architectures at aircraft level
Review articles	• Recent developments of miniature centrifugal compressors • Review of environmental control systems in other research fields

The background information presented in this chapter investigates data obtained from the chosen literature sample in the following order. Section 2.1 provides an overview of more electric aircraft technologies including propulsion configurations and electrical power systems. Section 2.2 presents a classification of existing environmental control system configurations with an additional consideration of novel cycles described in various patent applications, followed by fundamentals of vapour compression cycles covered in Section 2.3.

2.1. MORE ELECTRIC AIRCRAFT TECHNOLOGIES

The technologies installed on more electric aircraft having an impact on the environmental control system's functioning are related to the propulsion configuration and the electrical power systems. The major trends in propulsion configurations are presented in Subsection 2.1.1, followed by a review of electric power system architectures presented in Subsection 2.1.2.

2.1.1. PROPULSION SYSTEM CONFIGURATION

Propulsion systems have seen an increase in bypass ratio throughout their development. The highest bypass ratio in conventional gas turbine engines currently in operation is achieved in the Pratt & Whitney PW1100 G geared turbofan. By using a gearbox to decouple the fan from the compressor, a large fan with a diameter of 205 cm could be installed leading to a bypass ratio of 12:1 [1] . As the bypass ratio increases and the engine cores become more compact, there is a higher impact of bleed air extraction on the specific fuel consumption. Using the high bypass ratio RB211 turbofan presented in Figures 2.1 and 2.2 as a reference engine, a study was conducted in Britain in the period 1985-1987 under the name "Zero bleed secondary power system study". The outcome of the investigation showed a 1 % decrease in fuel consumption by eliminating the bleed systems. It must be considered that the selected reference engine was originally designed for bleed extraction

[1] URL https://www.pw.utc.com/products-and-services/products/commercial-engines/Pratt-and-Whitney-GTF-Engine/ [cited November 29, 2018]

and relatively small amounts of mechanical power extraction, thus higher saving potentials could be reached by developing propulsion units tailored to all electric applications [27].

Figure 2.1: RB211 - front view [Own photo - taken on November 17, 2017 at Royal Air Force Museum Cosford]

Figure 2.2: RB211 - back view [Own photo - taken on November 17, 2017 at Royal Air Force Museum Cosford]

To understand the effects of power off-takes on fuel consumption, a theoretical study was carried out on the CF6-80E1 reference engine. Using the exergy analysis method to model a three wheel bootstrap environmental control system, it was determined that an electrical power off take results in 2 % fuel savings as compared to using bleed air for driving the ECS if the system operates with 50 % recirculation [1]. The variation of thrust specific fuel consumption with various mission phases is presented in Figure 2.3. It can be seen that the bleed air off take has a higher impact on fuel consumption than the electrical power off take.

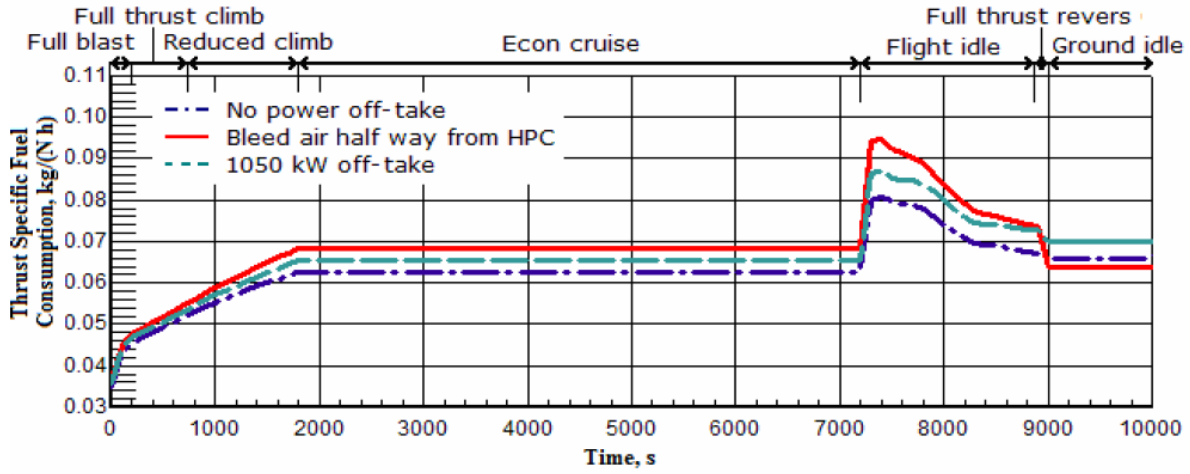

Figure 2.3: Bleed system [1]

To appreciate the potential benefits of bleed-air-free architectures it is useful to develop an understanding of the working principles behind typical bleed systems and their constituent components. Considering the bleed system presented in Figure 2.4, air can be extracted from various bleed ports such as the intermediate or high pressure stage of the compressor. This extraction is achieved by a series of non return valves, high pressure shut off valves and pressure reducing shut off valves that control the air pressure prior to entering the pre cooler . Other than meeting the pressurisation, heating and ventilation functions of the environmental control system, the bleed system can also be used to assist the engine during the start-up cycle, provide wing and engine ice protection, actuate thrust reversers or pressurise hydraulic reservoirs [2, pp. 244-258].

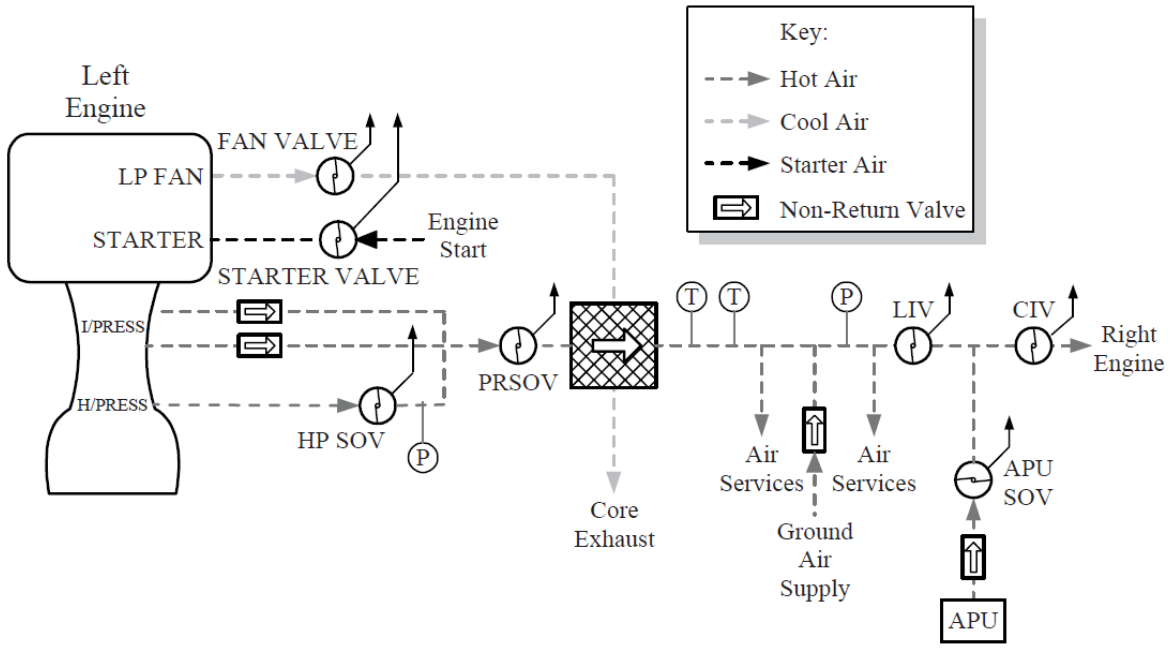

Figure 2.4: Bleed air extraction system architecture [2, p. 244]

A shift towards bleed-air-free designs is identified for the propulsion units of more electric aicraft, such as in the case of the Rolls Royce Trent 1000 [2] or the General Electric GEnx-1B [3]. Unlike the Trent family, the GEnx platform offers both a pneumatically equipped option under the name of GEnx-2B currently installed on the Boeing 747-8, as well as a bleedless variant under the name of GEnx-1B installed on the Boeing 787. Performance data of both variants including their derivatives is presented in Table 2.2 [4].

Table 2.2: GEnx platform engine options - geometric and performance specifications

GEnx General Characteristics	**-1B70 (B787-8)**	**-1B74 (B787-9)**	**-1B76 (B787-10)**	**-2B67 (B747-8)**
Takeoff thrust (lbs-force, kN)	69800, 310	74100, 329	76100, 338	66500, 296
Bypass ratio (takeoff/top-of-climb)	9.3/8.8	9.1/8.6	9.1/7.9	8.0/7.4
Overall pressure ratio (takeoff/top-of-climb)	43.8/53.3	46.3/55.4	47.4/58.1	44.7/52.4
Air mass flow (takeoff, lbs-mass/sec)	2559	2624	2658	2297
Fan diameter (in, cm)	111.1", 282	111.1", 282	111.1", 282	104.7", 266
Base engine length (in, cm)	184.7, 469	184.7, 469	184.7, 469	169.7, 431
Compressor stages (Fan/Booster/HPC)	1/4/10	1/4/10	1/4/10	1/3/10
Turbine stages (HP/LP)	2/7	2/7	2/7	2/6
Combustor	SAC/TAPS	SAC/TAPS	SAC/TAPS	SAC/TAPS
Control	FADEC III	FADEC III	FADEC III	FADEC III

[2] URL https://www.rolls-royce.com/products-and-services/civil-aerospace/airlines/trent-1000.aspx/ [cited October 20, 2018]
[3] URL https://www.geaviation.com/commercial/engines/genx-engine [cited October 20, 2018]
[4] URL https://www.geaviation.com/sites/default/files/datasheet-genx.pdf [cited October 20, 2018]

2.1.2. ELECTRIC POWER SYSTEM ARCHITECTURES

Aircraft power system architectures consist of generation systems, transformation and distribution systems and consumers. The power provided by the propulsion system can be divided into main power required for thrust and secondary power required to drive the remaining aircraft systems. As the environmental control system is dependant on secondary power it is important to understand the various ways the engine can provide it [28]. The secondary power can be divided into pneumatic, hydraulic and electric power [2, pp. 81-83]. In case of conventional aircraft the secondary power represents up to 5 % of the mission fuel [29, pp. 235-290]. With the advent of more electric aircraft the role of pneumatic and hydraulic power has been gradually replaced by electric power systems[30]. A detailed comparison between conventional and electric subsystem architectures is provided in Figure 2.5. It can be seen that in the case of electric subsystem architectures the secondary power off-takes come exclusively in the form of shaft power, thus increasing the shaft horsepower extraction penalty as compared to conventional subsystem architectures.

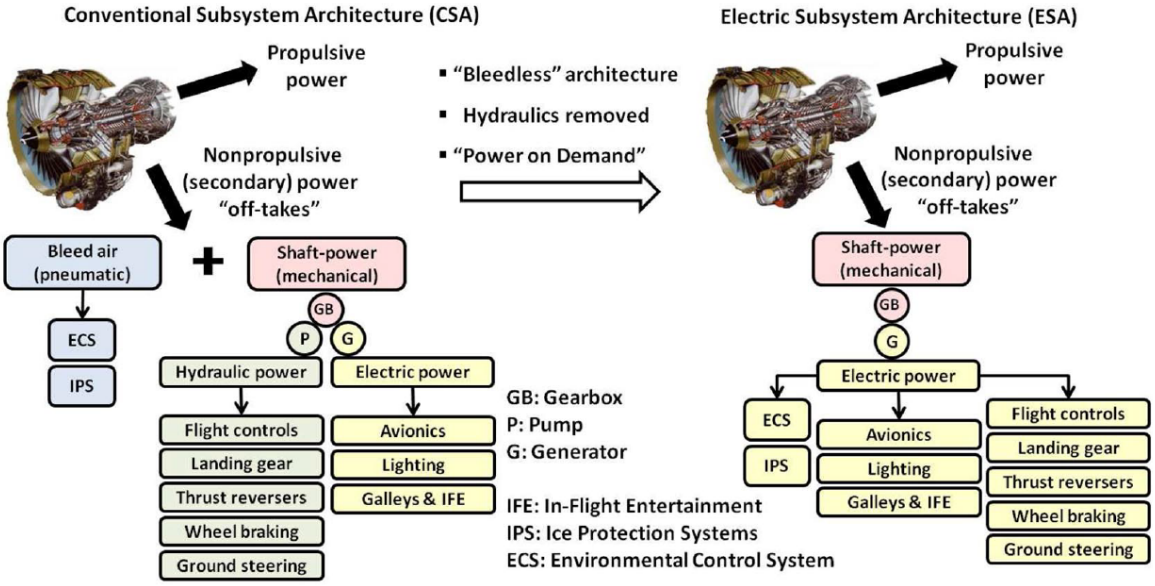

Figure 2.5: Secondary power usage: conventional versus electrical subsystem architectures [3]

Electrical power systems can be categorised as either constant or variable frequency generators. Constant frequency generators, as shown in Figure 2.6, are connected to the variable speed shaft of the engine through a constant speed drive. The constant speed drive is a variable ratio transmission gearbox used to convert the variable speed provided by the engine into constant speed required by the constant frequency generator [4]. Figure 2.7 shows an example of a variable frequency generator, with the generator being connected directly to the variable speed shaft of the engine.

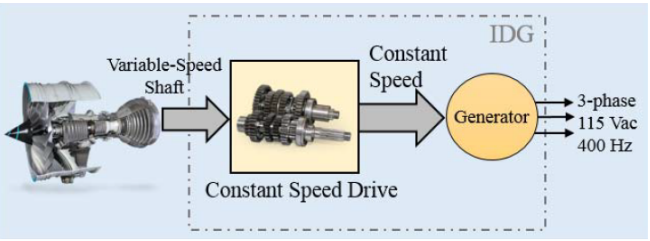

Figure 2.6: Constant frequency generator configuration [4]

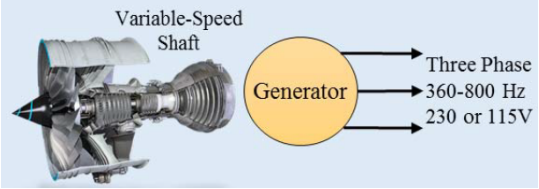

Figure 2.7: Variable frequency generator configuration [4]

The use of constant frequency systems on-board commercial transport aircraft dates back to 1958, as shown in Table 2.3 which provides a historical perspective of generator development for aerospace applications. It can be seen that a direct current (DC) constant frequency generator rated at 30 kVA was available for the Boeing 707. The highest rated constant frequency generators still used today are installed on the Boeing 777

and 767-400ER, reaching a power of 120 kVA [4]. Having two engines with one generator mounted on each of them, the total resulting power provided by the main generators equals 2x120=240 kVA.

Table 2.3: Power ratings for constant frequency generators [4]

Aircraft Model	First year of service	(Approx.) Passenger capacity	Main Generators Power (Excluding APU)
Convair B-36	1949	(Military)	4x30kVA
Boeing B-52H	1955	(Military)	4x60kVA
Boeing 707	1958	219	4x30kVA
Boeing 727	1964	189	3x38kVA
Vickers VC10	1964	151	4x40kVA
Boeing 737 (NG)	1968 (1997)	210	2x90kVA
Airbus A320	**1987**	**220**	**2x90kVA**
Boeing 747-800	1988	660	4x90kVA
Boeing 767-300ER	1988	258	2x90kVA
Airbus A340	1991	375	4x90kVA
Airbus A330	1992	335	2x115kVA
Boeing 777	1994	396	2x120kVA
Boeing 717	1999	100	2x40kVA
Boeing 767-400ER	2000	256	2x120kVA

The electrical power systems making possible the transition to more electric aircraft consist of variable frequency generators (VFG) connected to the high pressure spool of the engine. The main reason for connecting the generator to the high pressure spool (N2 shaft) instead of the low pressure spool (N1 shaft) is that the N2 shaft has a higher speed of rotation allowing to decrease the size of the generator. Another reason leading to this design choice is the speed variation of the N2 shaft which occurs in a smaller range compared to that of the N1 shaft, as shown in Table 2.4 [4].

Table 2.4: N1 and N2 speed variations [4]

Engine Series	Aircraft (example)	N1 (100%) [rpm]	N2 (100%) [rpm]	$\frac{N1_{max}}{N1_{min}}$	$\frac{N2_{max}}{N2_{min}}$
EA GP7200	A380	2467	10998	6.1	1.9
CFM56	B737	5175	14460	5.2	1.8
GEnx-2B67	B747-8	2560	11377	6.7	2.3
PW1100G	A320neo	N/A	N/A	5.7	1.8
GE CF34-8C1	Business Jet	7400	17820	N/A	1.8
IAE V2500	**A320**	**5650**	**14950**	**4**	**N/A**
PW300	Business Jet	10608	26956	N/A	1.6
GE90	B777	2261	9331	6.1	1.7

State of the art power generation architectures include the 150 kVA generator mounted on the Airbus A380 or the 250 kVA generator mounted on the Boeing 787 [4]. The *advantages* of using a variable frequency generator for generating electricity as opposed to a conventional constant frequency generator are the following:

- *Eliminating the constant speed drive.* The elimination of this gearbox in case of variable frequency generators resulted in decreasing the overall weight, increasing the reliability and increasing the energy conversion efficiency of the electrical power system [2] [31] [32] .
- *Eliminating the main engines starters.* A variable frequency starter generator (VFSC) can be operated to start the engines, eliminating the traditional air starter and associated bleed manifolds used in conventional propulsion systems, thus contributing to a decrease in the propulsion system weight [33] [34].

2.2. ENVIRONMENTAL CONTROL SYSTEMS CONFIGURATIONS

The main functions of environmental control systems for aerospace applications consist of providing cooling, heating, pressurisation, ventilation and dehumidification for the cabin, cockpit and cargo compartments [2, pp. 259-295]. Design drivers depend on the type of aircraft, commercial or military, leading to different requirements including but not limited to aspects such as mass air flow, heat load and energy consumption. The ECS itself is an assembly of subsystems [35]. Conventional ECS installed on most commercial transport aircraft flying today consists of the following systems: air distribution system (ADS), temperature control system (TCS), air conditioning system (ACS), ventilation control system (VCS) and pressure control system (PCS) [36]. The aforementioned list is not exhaustive as optional equipment may be added to the ECS according to each airline's requirements.

Depending on the form in which the secondary power is used to drive the environmental control system, various architectures can be identified. The first category consists of conventional refrigeration cycles using bleed air provided by the engines, while the second consists of electric driven refrigeration cycles that operate independently from the engines. The two architectures just mentioned can be further classified as air cycle systems or vapour cycle systems depending on the working fluid and type of refrigeration cycle used.

2.2.1. AIR CYCLE APPLICATIONS

Traditional environmental control systems for aerospace applications rely on bleed air extracted from the propulsion system in the form of pneumatic power. This is made possible by extracting air from the high pressure stage of the compressor and using it to drive subsystems such as the air cycle machine [2, pp. 240-243]. The air cycle machine can be configured in various ways depending on the number and arrangement of components as shown in Figure 2.8. The base configuration, called the simple air cycle, consists of a fan and a turbine connected on a common shaft. Replacing the fan with a compressor results in the bootstrap cycle which consists of a turbine and a compressor being connected on the same shaft [9, p. 1197]. The third option is the three wheel bootstrap cycle that consists of a compressor, a fan and a turbine mounted on the same axis and rotating at the same speed. The three basic configurations mentioned above can be seen as building blocks that can be used to construct more elaborate ECS architectures. Adding an additional cooling turbine to the three wheel bootstrap cycle, a four wheel cycle is obtained. Other components that can be added to an air cycle system include condensers, reheaters, recirculation systems, water separators, check valves and additional heat exchangers [36].

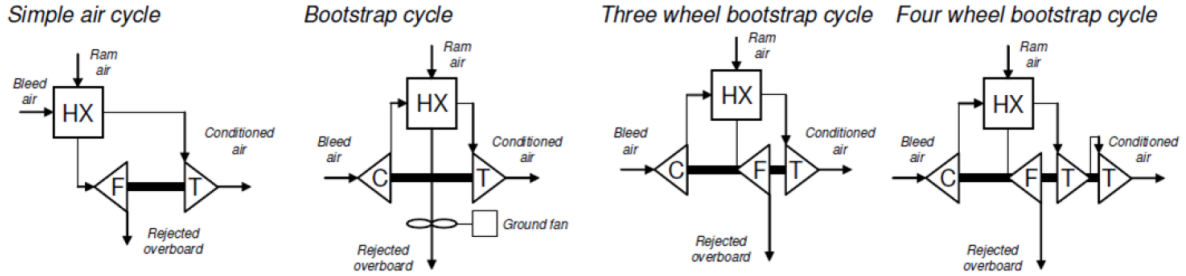

Figure 2.8: Air cycle machines [5]

Aircraft with a traditionally configured ECS based on the air cycle system can be classified according to the type of air cycle machine and water separation system used, as presented in Table 2.5. The most rudimentary form of an air cycle machine installed on-board commercial transport aircraft is the two wheel simple system which found application in the Lockheed XC-35 introduced in 1935 and being the first aircraft to employ a pressurised cabin [37, p. 36]. Since then the air cycle machines became more complex, still being used today on-board commercial aircraft in the form of two, three or four wheel bootstrap systems. The latter configuration is considered to be the most advanced as it consists of four wheels mounted on the same shaft, namely a compressor, a fan and two cooling turbines.

Table 2.5: Types of environmental control systems using air cycle machines [23]

System Type		Application Aircraft
Two-wheel Simple System		XC-35, AN-24, IL-18, IL-62, M-19, M-21fa
Two-wheel Bootstrap System	Low Pressure Water Separation	B707-300, B727, B737-300, B737-500, MD-80, MD-90, DC-9
	High Pressure Water Separation	F-18, T46A, B737-400, ATR-72
Three-wheel Bootstrap System	Low Pressure Water Separation	MD-95, A300, A310, B747-400, DC-10, L-1011, B737-600, B737-700
	High Pressure Water Separation	**A320, A330, A340, BAE-146, B737-800, B737-900, B747-800, B757, B767, B787(E-ECS)**
Four-wheel Bootstrap System		B777, A380

At this point a distinction can be made between low pressure and high pressure water separation systems [9, p. 1198]. Water separators are required to remove the moisture from the air which forms during the operation of the refrigeration unit. Low pressure water separators are mounted downstream of the cooling turbine of the air cycle machine, having a coalescer bag and a vortex generator as the main components. Looking at Figure 2.9 the air inlet leads directly to the coalescer where fine water particles contained by the humid air are converted to large water droplets. The separation process starts as the water droplets pass through the vortex generator during which a centrifugal force directs the water to the collector section of the separator. As the name suggests, air has already been expanded in the turbine and is at low pressure when entering the water extractor. The integration of a low water separation system in the environmental control system of the McDonnel Douglas DC-10 is presented in Figure 2.12.

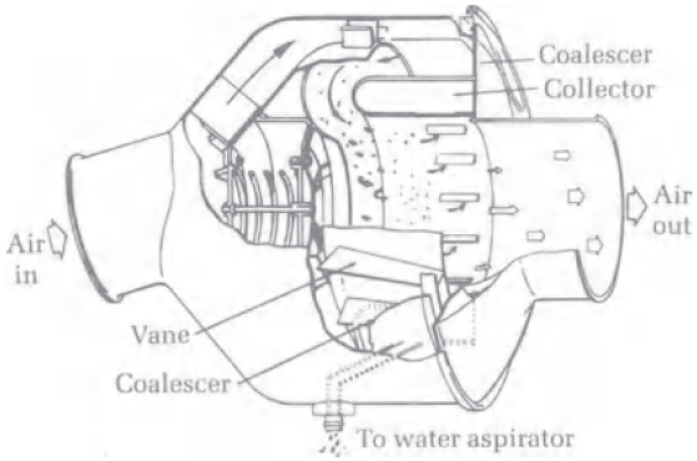

Figure 2.9: Low pressure water separator [6, p. 569]

The alternative comes in the form of a high pressure water separator system mounted upstream of the cooling turbine. This more elaborate configuration, presented in Figure 2.10, consists of a water extraction loop including a reheater, a condensing heat exchanger and a water extractor. As humid air enters the hot side of the reheater its temperature is decreased followed by further cooling taking place in the hot side of the condenser. At this point the temperature of the water mixture is decreased up to the dew point using cold air coming from the turbine's outlet. This results in the formation of water droplets that are then removed from the air/water mixture once they enter the water extractor, further detailed in Figure 2.11. Before entering the cooling turbine, the air passes through the cold side of the reheater where its temperature is increased [7]. An application of this system is presented in Figure 2.13 part of the environmental control system of the Airbus A321.

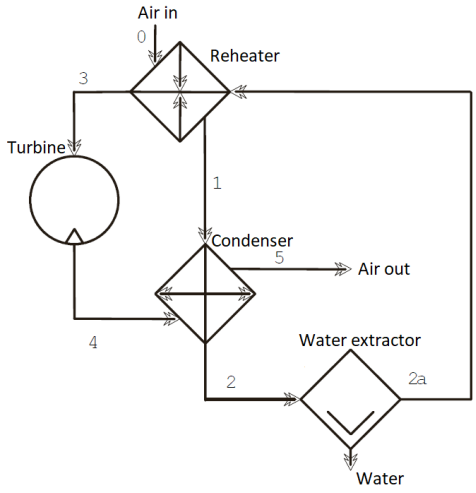

Figure 2.10: High pressure water separator - extraction loop [7]

The water extractor itself is much simpler than the one used for the low pressure water separator system. Considering the assembly depicted in Figure 2.11 the air and water mixture enters the extractor's inlet, being directed towards the swirler where the separation process takes place under the action of centrifugal force. Once removed from the mixture the water passes through the water collector. At this point two outlets are located, one for air outlet and the other for the water outlet [8]. Compared to a low pressure water separation system, the high pressure alternative is preferred as it provides a higher cooling capacity due to the fact that increased amounts of water can be compressed at higher pressure [38] .

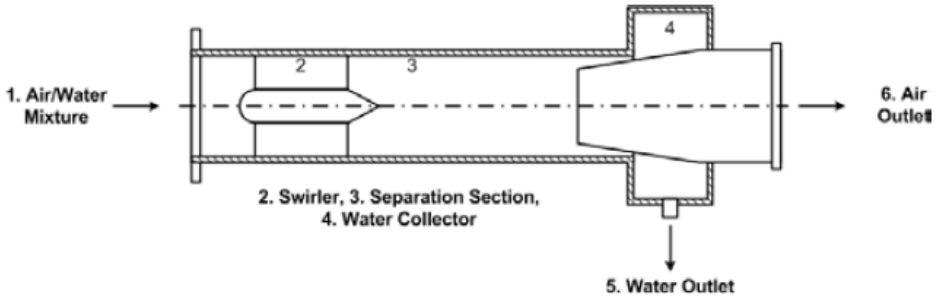

Figure 2.11: High pressure water extractor [8]

Using air as the working fluid, the reverse Brayton cycle is the basis of air cycle systems configurations. Its working principles are introduced using the environmental control unit installed on board the McDonnel Douglas DC-10 as shown in Figure 2.12. Its three wheel bootstrap air cycle machine is built around three rotating aerodynamic impellers, namely a fan, a compressor and a turbine connected on the same shaft rotating at speeds of up to 50,000 rpm. Before entering the compressor of the air cycle machine, bleed air provided by the engine is preconditioned for temperature and pressure through a series of flow control valves. Ram air powered by the fan is used as a temperature sink providing the cooling capacity of the heat exchanger installed downstream of the compressor. This is required to reduce the temperature of the air prior to entering the turbine where further cooling is achieved. Before being directed towards the cabin, humid air coming from the turbine is passed through the water separator which is of low pressure type and installed downstream of the cooling turbine. The collected water can be further used to enhance the cooling capacity of the heat exchanger by means of a channel leading to a water injector. As the system is designed to operate under various atmospheric conditions depending on different flight phases, part of the air cycle machine can be bypassed during cruise. This is possible by controlling the turbine bypass valve which allows compressed air to enter the cabin directly as conditioned air, without going through the turbine [6, pp. 573-574].

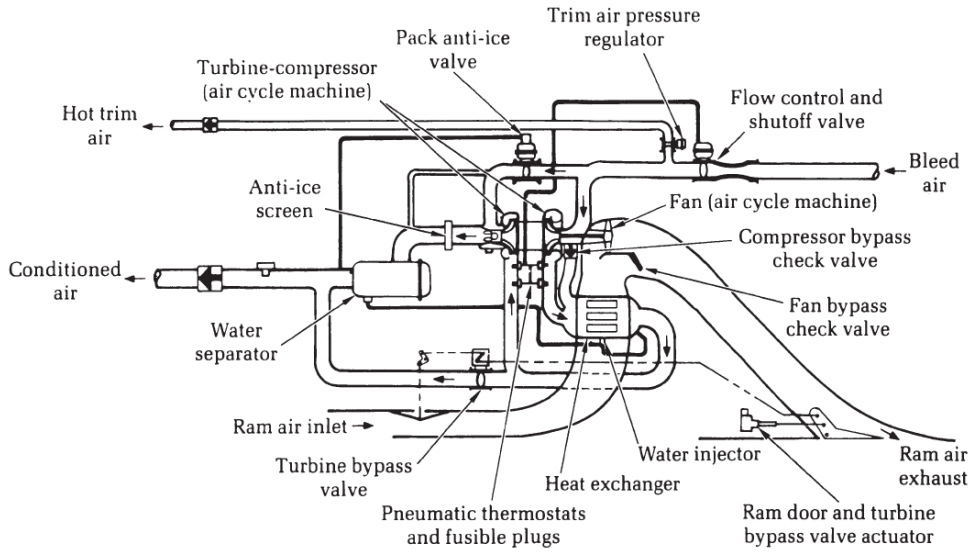

Figure 2.12: McDonnel Douglas DC-10 ECS: Three wheel bootstrap with low pressure water separator [6, p. 574]

A slightly advanced derivation of the three wheel bootstrap cycle can be found installed on the Airbus A321, featuring a high pressure water separation system. This configuration, presented in Figure 2.13, has a similar functioning principle as the three wheel system previously discussed above but its complexity is raised due to the integration of additional heat exchangers. In this case the preconditioned bleed air first goes through the main heat exchanger where its temperature is reduced prior to entering the air cycle machine. Air at high temperature and pressure coming from the compressor is directed towards a second heat exchanger, called the main heat exchanger, which removes the heat of compression. Between the compressor and the turbine the high pressure separation system is installed consisting of a reheater, a condenser and a water extractor connected in cascade. The system is considered to be more efficient than its three wheel bootstrap counterpart equipped with low pressure separation system due to the increased temperature range. Having a high pressure water separation system extends the operational envelope of the air coming from the cooling turbine up to -50° Celsius, while the temperature limit of low pressure systems is 0° Celsius [9, p. 1198].

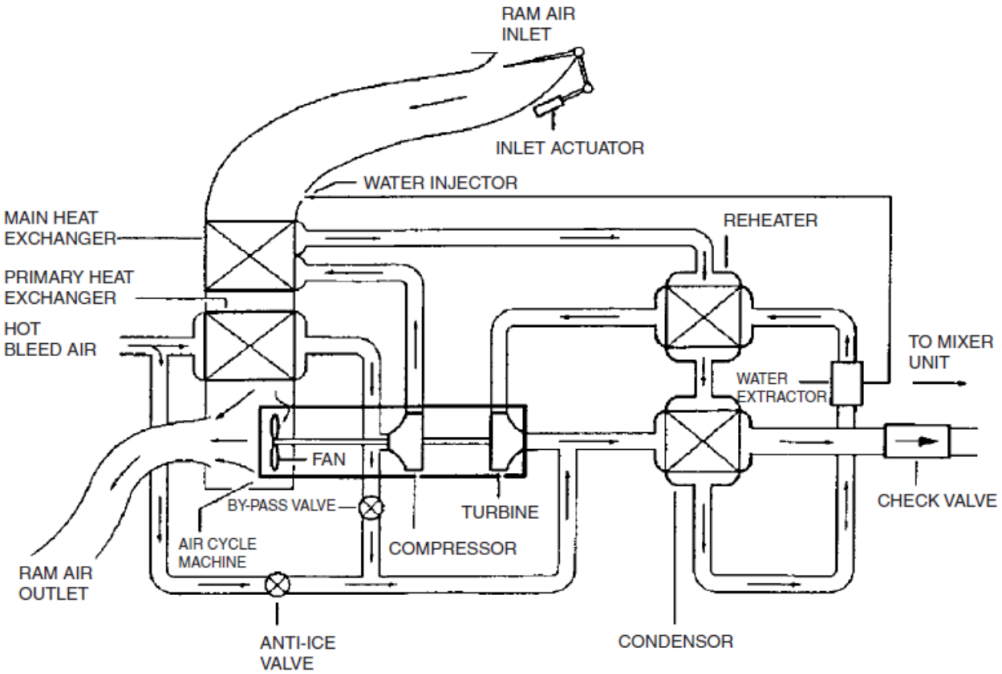

Figure 2.13: A321 ECS: Three wheel bootstrap with high pressure water separator [9, p. 1199]

Four wheel bootstrap systems include an additional turbine downstream the condenser and are considered to be more energy efficient than equivalent three wheel bootstrap systems [39]. Figure 2.14 presents the environmental control system of the Boeing 777 which involves the condensing cycle technology. Equipped with a high pressure water separator, the functioning principles of this air cycle machine are similar to the one of the Airbus A321 described above in Figure 2.13, with the only difference coming from passage of air once it exits the first stage turbine. In case of a three wheel bootstrap cycle, air exits the first stage turbine with a temperature of -40° Celsius in order to reach the required temperature of 3° Celsius after passing through the condenser and being mixed with recirculated air from the cabin. In case of the four wheel bootstrap cycle, air exits the first stage turbine with a temperature of 2° Celsius, goes through a temperature rise of up to 37° Celsius at the condenser exit and leaves the second turbine with a temperature of -12° Celsius. Not having to cool the air to -40 degrees as in the case of the three wheel bootstrap cycle leads to energy savings in the case of four wheel bootstrap cycle [10].

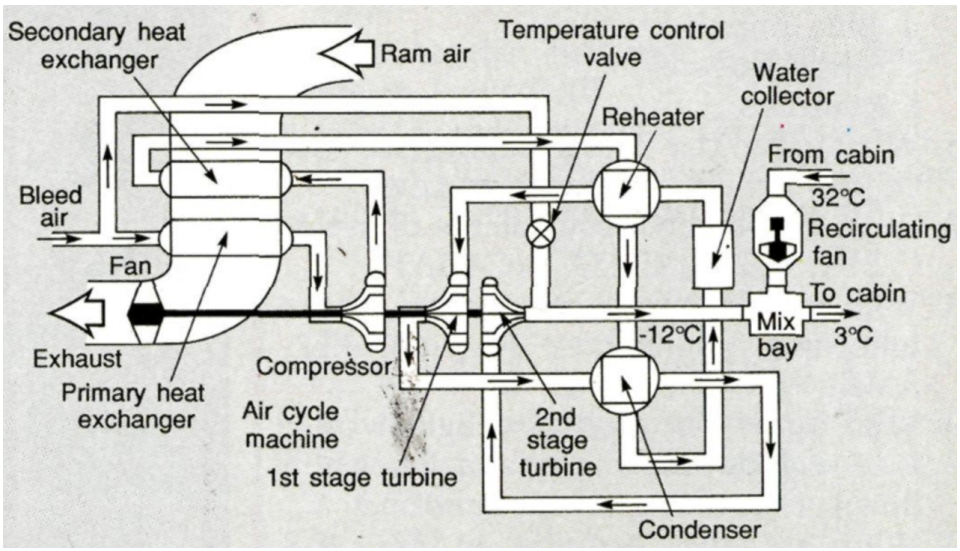

Figure 2.14: Boeing 777 ECS: Four wheel bootstrap with high pressure water separator [10]

As the aviation industry evolved towards more electric aircraft configurations, great emphasis was placed towards the benefits of bleedless propulsion based environmental control systems. Since bleed system technology relies on components such as bleed air manifold and pre-coolers that add complexity and weight to the propulsion system, the process of bleed air extraction is seen as an exergy loss that reduces the total thrust an engine could potentially produce [40]. Completely eliminating the bleed system required extracting secondary power in the form of electric power using more efficient electrical machines such as the variable frequency generators currently manufactured by UTC Aerospace Systems or Safran Electrical and Power. Shifting from pneumatic to electrical power allowed the elimination of the conventional bleed systems, allowing to leverage on the benefits of *bleed-air-free propulsion systems*. The electric air conditioning configuration originally proposed by The Boeing Company in a patent application [41] is now present in the industry as a subsystem installed on-board the Boeing 787, consisting of an air cycle system linked to a bleedless engine setup. The air cycle machine itself is a three wheel bootstrap with high water separation system, as described previously in Figure 2.13. The novelty comes from the overall system architecture which makes use of an electric driven compressor to meet the pressurisation requirement, as opposed to bleed air [42].

Considering Figure 2.15, the novelty of an all electric configuration comes from the management of air supply at the system's inlet. Fresh air enters the system at point (a) and is compressed using an electric driven air compressor up to point (1) where it enters the primary heat exchanger labelled HX1. From point (1a) onward, the working principles of the all electric system are the same as those of a conventional air cycle system coupled to a bleed based architecture. Simulation studies of a similar all electric based environmental control system revealed that the main exergy destruction was located in the main heat exchanger and the mixer [43], while in the case of configurations coupled to bleed systems the highest impact on the air cycle's coefficient of performance was determined to be the gas turbine's compressor [44].

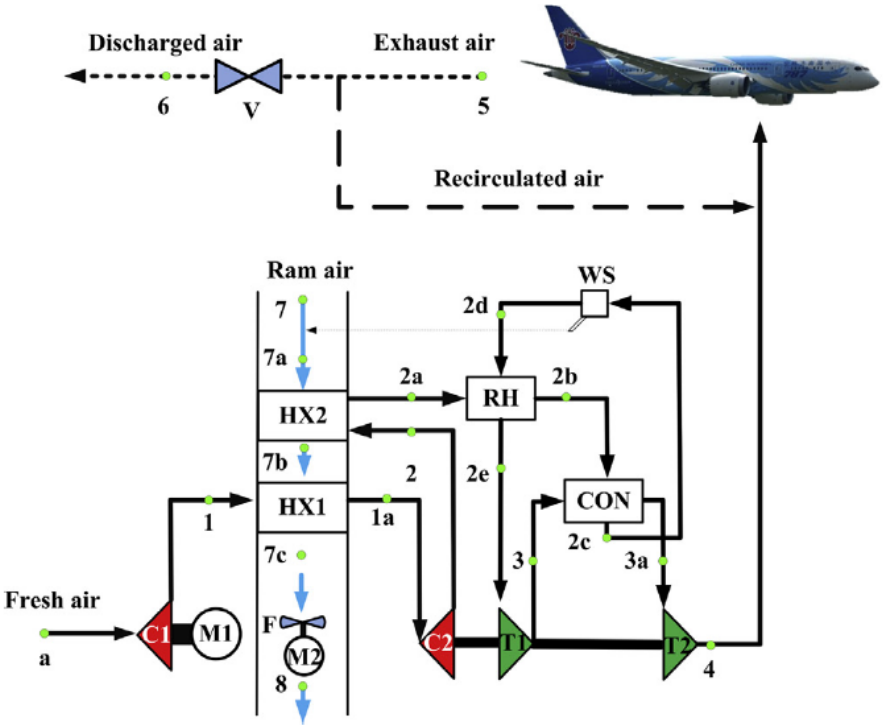

Figure 2.15: Schematic layout of state-of-the-art electrically driven environmental control system based on traditional air cycle technology - Boeing 787 application [11]

2.2.2. VAPOUR CYCLE APPLICATIONS

An alternative to using air as the working fluid comes in the form of vapour cycle system refrigeration [45, pp. 493-494]. Consisting of a vapour compression cycle in combination with a pneumatic powered configuration this option was available for older generation large transport aircraft such as the Douglas DC-8, Convair 880 and some options of the Boeing 707 and 720 [12, pp. 22-27]. The refrigeration units themselves can be classified according to the configuration of the vapour compression cycle. Depending on the components used and their arrangement, vapour cycle systems can be classified as either subcooling cycles, expansion loss recovery cycles or condensing cycles [15]. Compared to traditional air cycle systems, the coefficient of performance in case of vapour compression refrigeration units can be up to five times higher, resulting in increased thermal efficiency [2, p. 276].

Considering the refrigeration unit installed on board the Boeing 707 and 727 variants presented in Figure 2.16, the four basic components of a vapour compression cycle can be identified as the refrigerant compressor, the condenser assembly, the expansion valve and the evaporator assembly. Refrigerant in gaseous state is compressed in the compressor which raises its temperature and pressure. To remove the heat of compression, a condenser assembly is used, allowing heat transfer between refrigerant and ram air, the latter serving as the cooling medium. During condensation the refrigerant state changes from vapour to two phase flow and finally to liquid. The expansion valve is used to decrease the refrigerant's pressure and temperature prior to entering the evaporator assembly in which the temperature of the flow coming from the cabin is reduced to meet the cooling requirements. Looking at the other components of the system, a sub-cooler assembly can be identified allowing to classify the refrigeration set-up as a subcooling cycle. The sub-cooler itself is a heat exchanger allowing heat transfer between the refrigerant in liquid state prior to entering the evaporator and cold refrigerant gas coming out from the evaporator. The resulting heat transfer aims to prevent premature vaporisation of refrigerant prior to entering the evaporator [12, pp. 22-27].

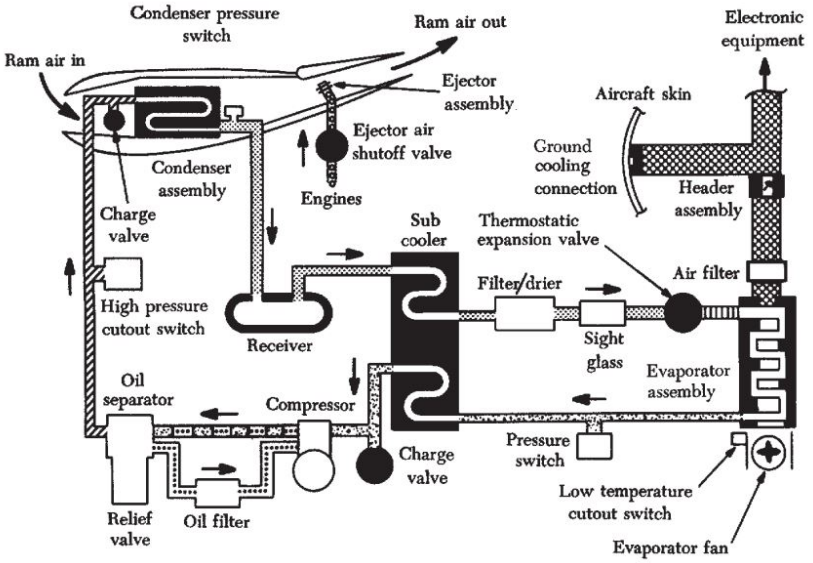

Figure 2.16: Boeing 707 ECS: Refrigeration unit [12, p. 22]

2.2.3. HYBRID AIR/VAPOUR CYCLE APPLICATIONS

Novel configurations including an air cycle system, a vapour cycle system and a traditional bleed set-up have been proposed in different patent applications [13] [46], giving birth to the so-called hybrid or integrated air and vapour cycle cooling systems. Considering US Patent 2017/0057641 A1 [13] depicted in Figure 2.17, the refrigerant compressor of the vapour cycle system is driven by the turbine of the air cycle system to which it is connected through a magnetic coupling. Although the complexity of a hybrid system is increased, its attractiveness comes from the potential to minimise the fuel penalty associated with bleed air extraction as compared to a traditional air cycle based configuration.

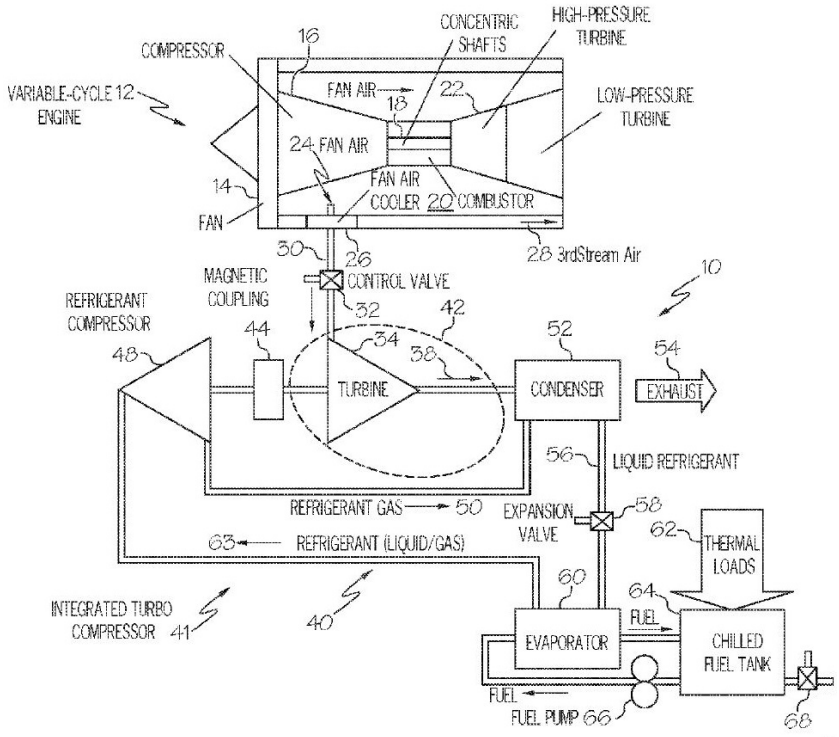

Figure 2.17: Hybrid system patent [13]

A hybrid air and vapour cycle configuration has found application in the business jet market, being currently installed in the Cessna Citation CJ4 which has a cooling system that operates independently from the pressurisation and heating systems. Similar to a traditional bootstrap configuration, the air cycle system is driven by bleed air extracted from the gas turbine's compressor, with the left engine supplying air for the flight deck and the right engine supplying air for the cabin. The vapour cycle system, used only for cooling purposes, comprises of different components installed either inside the pressurised cabin or in the tailcone. The condensing unit comprising of the refrigerant compressor and condenser assembly are installed in the tailcone, while the three evaporator assemblies together with the required cold air ducting and expansion valves are installed in the pressurised compartment of the cabin [5].

Hybrid configurations involving polyalphaolefin (PAO) loops have also been proposed for military applications in which the cooling of the cockpit is linked to that of the avionics by means of various subsystems [14]. Figure 2.18 presents such a configuration consisting of seven integrated subsystems including the 1) fuel system, 2) air cycle system, 3) vapour cycle system, 4) oil loop, 5) cold PAO loop, 6) a hot PAO loop and 7) hydraulic system. Used for meeting the cooling requirements of the cabin, the air cycle system is coupled to the vapour cycle system through a heat exchanger connected to the hot PAO loop. The cold PAO loop transports dissipated heat loads from avionics to the vapour cycle system, the heat transfer being conducted in the evaporator. The hot PAO loop transports heat rejected by the vapour cycle system to the fuel which acts as a heat sink. This strategy allows to decrease the size of the ram air ports, thus reducing the fuel penalty due to drag loss. A military application of the vapour compression system using R134a refrigerant as the working medium is currently available for the F22-Raptor fighter jet [47]. Considering the complexity of integrated systems, control strategies can have a high impact on system performance. Experimental studies comparing the superheat and capacity control strategy with the alternate cycle-based strategy identified a higher coefficient of performance in case of the latter as it did not require back pressure control valves [48].

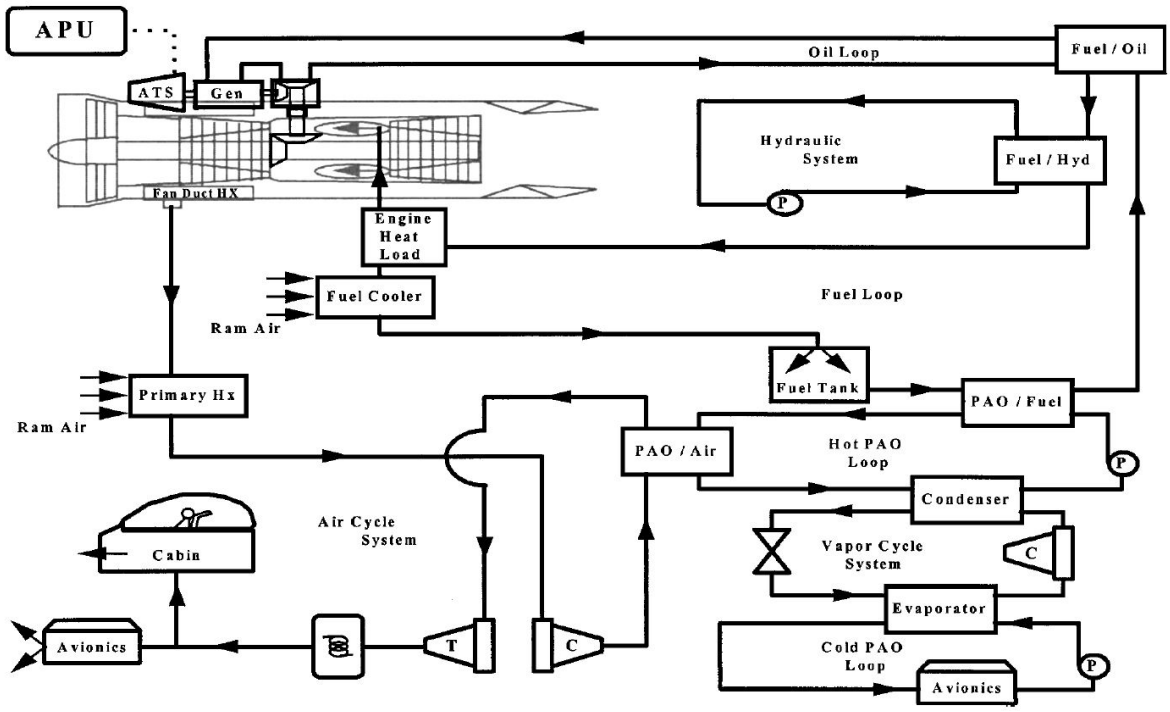

Figure 2.18: Hybrid system for military applications [14]

[5] URL http://www.omnijet.com/forsalecessna/citationcj4.pdf [cited October 20, 2018]

2.3. THERMODYNAMIC CYCLES FOR REFRIGERATION SYSTEMS

In this section the fundamentals of vapour compression refrigeration cycles are introduced. Based on the inverse Rankine cycle, the vapour compression cycle is the foundation of vapour compression refrigeration. While the reverse Brayton cycle uses air as the working medium, the vapour cycle technology make use of a refrigerant medium circulating inside a closed system. Vapour cycles can be classified into three major categories: compression, absorption and adsorption cycles. This section is focused on describing the functioning principles behind compression systems, starting with the simple reverse Carnot cycle up to more elaborate derivations including multistage cycles.

2.3.1. OVERVIEW OF VAPOUR COMPRESSION REFRIGERATION CYCLES

The starting point in analysing refrigeration systems is understanding the possible improvements that can be applied to a typical vapour compression cycle, identified as the typical VCC curve in Figure 2.19, allowing to increase its coefficient of performance up to the values associated with a theoretical Carnot cycle. The trend of coefficient of performance variation with evaporation temperature for different cycles is based on a simulation performed by Park et al [15] and shown in Figure 2.19. It can be seen that the coefficient of performance variation with evaporation temperature is dependent on the chosen cycle, thus choosing an appropriate cycle can have an impact on the thermodynamic performance of the environmental control system.

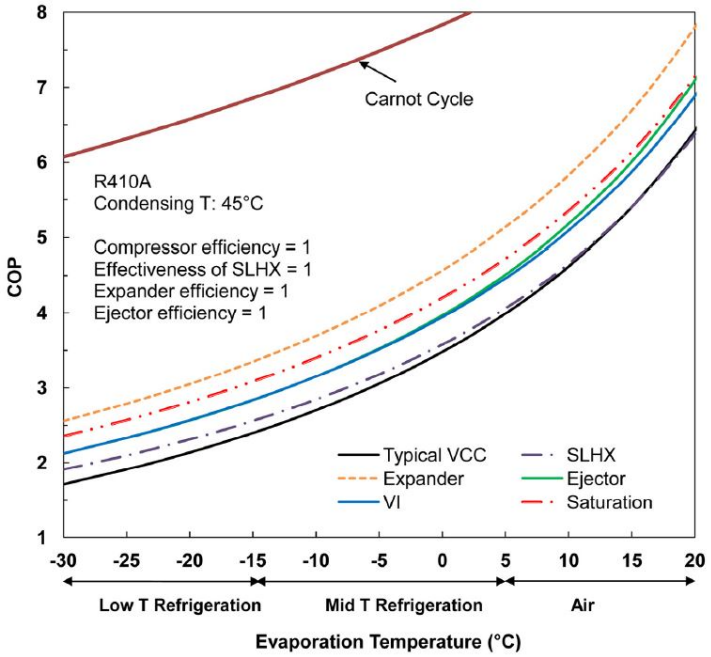

Figure 2.19: Variation of coefficient of performance with cycle options [15]

2.3.2. REVERSE CARNOT CYCLE

The first vapour compression cycle to be discussed is the reverse Carnot cycle. Presented in Figure 2.20 and also called the Carnot refrigeration cycle, it serves as the perfect model for a refrigeration cycle operating between two fixed temperatures. This is made possible by modelling all the processes as internally reversible and having no external irreversibilities between the working fluid and the environment [16, p. 29].

One component of the reverse Carnot cycle is the isentropic compressor used to raise the pressure and temperature of the gaseous refrigerant while changing its state from saturated vapour to superheated vapour. In order to maintain constant temperature during phase change, a machine operating under the reverse Carnot cycle requires an additional compressor, called an isothermal compressor. Mounted downstream the condenser, its role is to reject heat at constant ambient temperature T_0 while maintaining constant pressure in the two phase region of the refrigerant. Once in the condenser, the refrigerant changes state from vapour to saturated liquid. The process is followed by an isentropic expansion which takes place in an isentropic expander forcing the refrigerant in liquid state to transform into a mixture of liquid and vapour. In the evapora-

tor heat is withdrawn from the region to be refrigerated and the refrigerant state is transformed into saturated vapour prior to entering the isentropic compressor [16, p. 29].

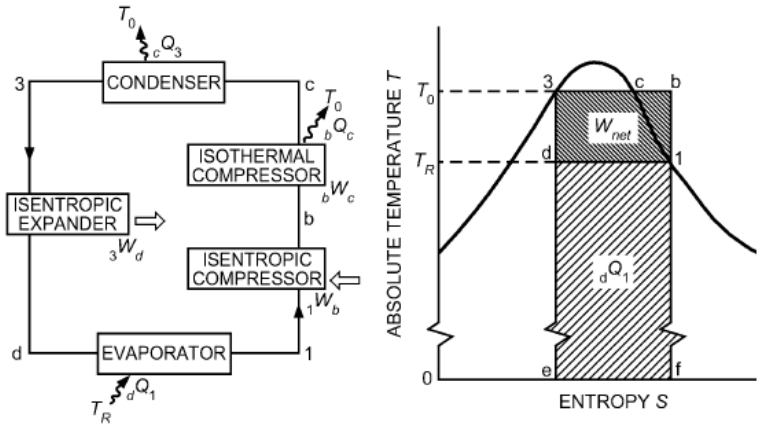

Figure 2.20: Reverse Carnot cycle [16, p. 29]

Assessing the efficiency of a refrigeration cycle can be done by computing its coefficient of performance, defined as the ratio between the useful refrigerant effect and the energy input required to operate the cycle. For a vapour compression cycle, the coefficient of performance can be obtained using Equation 2.1 [16, p. 25]. The resulting number, expected to be higher than 1 in case of a vapour cycle unit, can be interpreted in the following way: let's consider a resulting COP equal to 5. This indicates that for each kW of electricity provided to the system the result will be 5 kW of cooling.

$$COP = \frac{\textit{Useful refrigeration effect}}{\textit{Net energy supplied from external sources}} \tag{2.1}$$

At this point a distinction can be made between operating the vapour compression cycle as a refrigerator or as a heat pump. In case the system is required to provide cooling, thus operating as a refrigerator, the coefficient of performance can be calculated by dividing the heat flow in the evaporator by the net work required to operate the system, as shown in Equation 2.2. Otherwise if the system is required to provide heating, it is considered to operate as a heat pump and its coefficient of performance can be then calculated by dividing the heat flow in the condenser by the net work of the system, as shown in Equation 2.3.

$$COP_{\text{refrigerator}} = \frac{Q_L}{W_{net}} \tag{2.2}$$

$$COP_{\text{heater}} = \frac{Q_H}{W_{net}} \tag{2.3}$$

Implementing the Carnot refrigeration cycle into a practical machine would result in high initial cost and increased maintenance requirements [16, p. 29]. In the next section, a more practical system is introduced in the form of a theoretical single stage vapour compression cycle, serving as the ideal cycle for vapour compression refrigeration systems.

2.3.3. IDEAL VAPOUR COMPRESSION CYCLE

Considered to be the ideal cycle for vapour refrigeration systems, the basic vapour compression system presented in Figure 2.21 contains four basic components: an evaporator, a compressor, a condenser and an expansion valve. The system is obtained by slightly altering the reverse Carnot cycle presented above in Section 2.3.2. The main modifications aimed at making the refrigeration Carnot cycle more practical and thus transforming it into the ideal vapour compression cycle, also known as the inverse Rankine cycle, include removing the isothermal compressor and replacing the isentropic expander with a simple expansion valve. While the first modification results in a temperature drop of the refrigerant at the compressor exit prior to the phase change, the latter results in an entropy increase during expansion. Having a simple expansion device instead of a cooling turbine is motivated by the fact that operating the turbine inside the saturation curve of the working fluid would result in a relatively small amount of power produced as compared to the compressor input power, due to the low isentropic efficiency reached in the two phase mixture [49, p. 612]. The refrigerant saturation curve divides the thermodynamic cycle into different regions depending on the refrigerant state,

including saturated liquid, saturated vapour, superheated vapour, sub-cooled liquid and two phase mixture. Inside the saturation curve the refrigerant exists in a two phase state characterised by a variable 'x' named quality, ranging from 0 (pure liquid) to 1 (pure vapour).

Actual refrigeration systems differ slightly from the ideal vapour compression cycle. For example the refrigerant would enter the compressor as a superheated vapour rather than a saturated vapour. This procedure can be controlled by the degree of superheat applied to the system in order to ensure there is no liquid entering the compressor. Another aspect to be considered is the degree of subcooling applied to the system. Including additional subcooling is performed in order to have the inlet of the expansion valve operating outside the saturated liquid line, with the refrigerant in a sub-cooled liquid state.

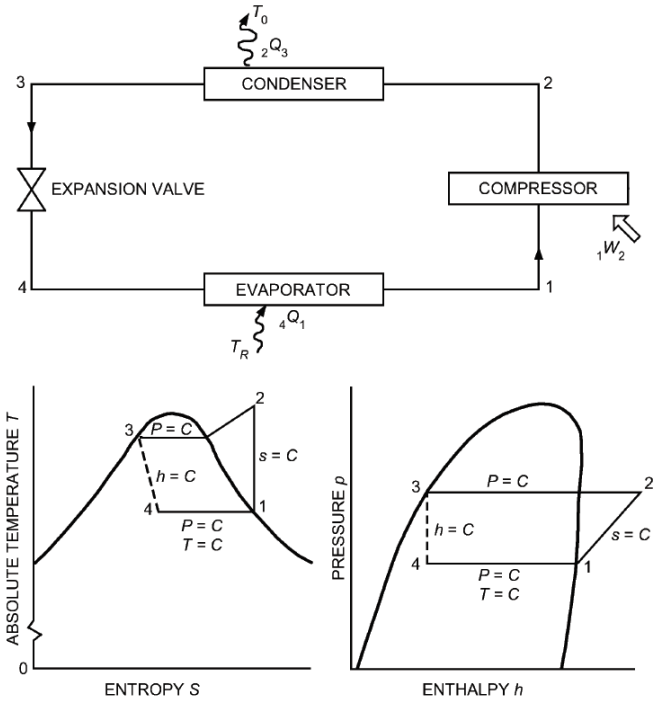

Figure 2.21: Ideal vapour compression cycle including the components of the system (top side of figure) as well as the associated T-S and p-h diagrams (bottom side of figure) [16, p. 30]

Refrigerant in a state of low pressure vapor enters the compressor at point (1). Enclosing the compressor in a control volume the resulting mass and energy rate balance equations reduce to the expression presented in Equation 2.4, allowing to calculate the work done by the compressor as a function of isentropic enthalpy rise.

$$\dot{W}_c = \dot{m}_r \, (h_2 - h_1) \tag{2.4}$$

Following the compression process, refrigerant goes in the condenser at point (2) where heat is rejected to the ambient sink at a rate shown by Equation 2.5. Notice that the heat rejected by the condenser is higher than the cooling provided by the evaporator since the vapour cycle unit needs to also dissipate the additional heat coming from the compression process. This verification can be performed by comparing the result of Equation 2.5 with that of Equation 2.6.

$$\dot{W}_{cond} = \dot{m}_r \, (h_2 - h_3) \tag{2.5}$$

$$\dot{W}_{cond} = \dot{W}_{evap} + \dot{W}_{comp} \tag{2.6}$$

2.3.4. ADVANCED VAPOUR COMPRESSION CYCLES

This section describes various configurations aimed at improving the efficiency of the ideal vapour compression cycle presented earlier in Section 2.3.3. The thermodynamic losses that are sought to be minimised by employing advanced cycle configurations cover high discharge refrigerant temperatures, high compression

work, high condenser heat release, throttling losses and low refrigerant capacity. The advanced cycles considered include subcooling, expansion loss recovery and multi-stage configurations.

Subcooling cycles make use of various components such as suction line heat exchangers, thermoelectric subcoolers or mechanical subcoolers. Suction line heat exchangers (SLHX), also known as internal heat exchangers, can be integrated into a vapour cycle system as shown in Figure 2.22. The role of the internal heat exchanger is to allow the isenthalpic process occurring in the expansion device to resemble an isentropic process. Located between the condenser outlet and the expansion valve inlet, the SLHX decreases the enthalpy at the evaporator inlet resulting in increased evaporator capacity. Based on an experiment conducted by Preissner et al [50] on an automotive air conditioning application, the resulting increase in coefficient of performance was recorded in the order of 5-10 % while using refrigerant R134a and a SLHX with effectiveness in the range of 55-65 %. Experiments conducted with different refrigerants such as R-22, R-32 and R-717 showed detrimental effects on the coefficient of performance with one responsible factor being the pressure losses in the internal heat exchanger itself, highlighting the importance of refrigerant selection for the refrigeration cycle configuration [51].

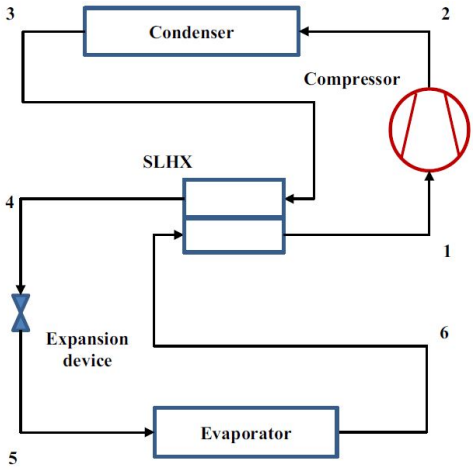

Figure 2.22: VCS with SLHX [15]

Research in the area of vapour compression refrigeration with mechanical subcooling has been performed since 1994 by Zubair [52] which aimed to increase the thermodynamic performance of refrigeration systems operating under extreme conditions with large temperature variation between the condenser and the evaporator. As the coefficient of performance degrades with increased temperature difference between the condenser and the evaporator, adding a mechanical subcooling loop allows to decrease the temperature of the liquid refrigerant coming out of the condenser. The resulting system based on an inverter-driven sub-cooler compressor resulted in 85 % reduction in power input, 65 % lower irreversibility rate and 20 % reduction in refrigerant flow rate.

Based on the Peltier effect, a thermoelectric subcooler device consisting of thermoelectric modules and two heat exchangers can be installed between the outlet of the condenser and the inlet of the expansion valve. The advantage of thermoelectric subcoolers is that they have no moving parts, thus promoting system reliability and requiring little maintenance. A simulation study performed by Winker et al [53] involving a CO_2 vapour compression system equipped with a thermoelectric subcooler showed improvements in the cooling capacity of 20 % and a 16% increase in the coefficient of performance.

Expansion loss recovery cycles consider the thermodynamic loss associated with the isenthalpic process occurring in the expansion device. To approach isentropic conditions during expansion, either an expander or an ejector can be installed instead of the typical expansion valve. Figure 2.23 presents the basic expander cycle, however it must be considered that various other configurations are available depending on how the expander is connected to the compressor. The expander device, modelled as a compressor working in reverse, helps improving the coefficient of performance by increasing the cooling capacity and reducing the compressor power consumption. First law estimations performed by Huff et al [54] for expander equipped

cycles predicted coefficient of performance improvements in the order of 40-70% and cooling capacity increments in the order of 5-15 %.

Figure 2.24 shows the integration of an ejector assembly into a basic vapour cycle system. The ejector assembly is a device composed of a nozzle, a mixing chamber and an ejector, transforming expansion losses into kinetic energy aiming to reduce compression work. Research covering ejector cycles performed by Li and Groll [55] identified the performance of the separator as having an impact on the resulting improvements of the coefficient of performance, which showed improvements of up to 16%, considering that liquid entering the compressor would increase the compressor work.

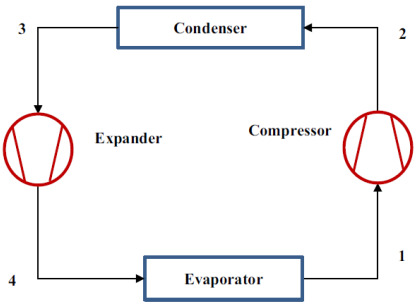

Figure 2.23: Expander cycle [15]

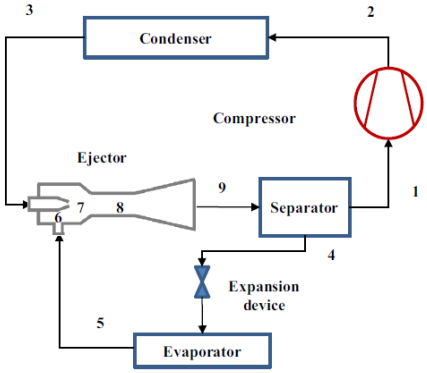

Figure 2.24: Ejector cycle [15]

Aimed at increasing the coefficient of performance of cycles operating under extreme ambient conditions, multi stage cycles allow to decrease the irreversibility during compression as compared to single stage configurations. An optimisation study conducted by Baakeem et al [17] of the two stage cycle with flash intercooling shown in Figure 2.25 considered the effect of eight different refrigerants whose properties are listed in Table 2.6. Using the conjugate directions method with sub-cooling, de-superheating parameters, evaporator and condenser temperature as the optimisation variables, the maximum coefficient of performance achieved was 6.17 for ammonia while a minimum of 4.95 was recorded for R407C, again highlighting the coupling between the coefficient of performance and refrigerant selection.

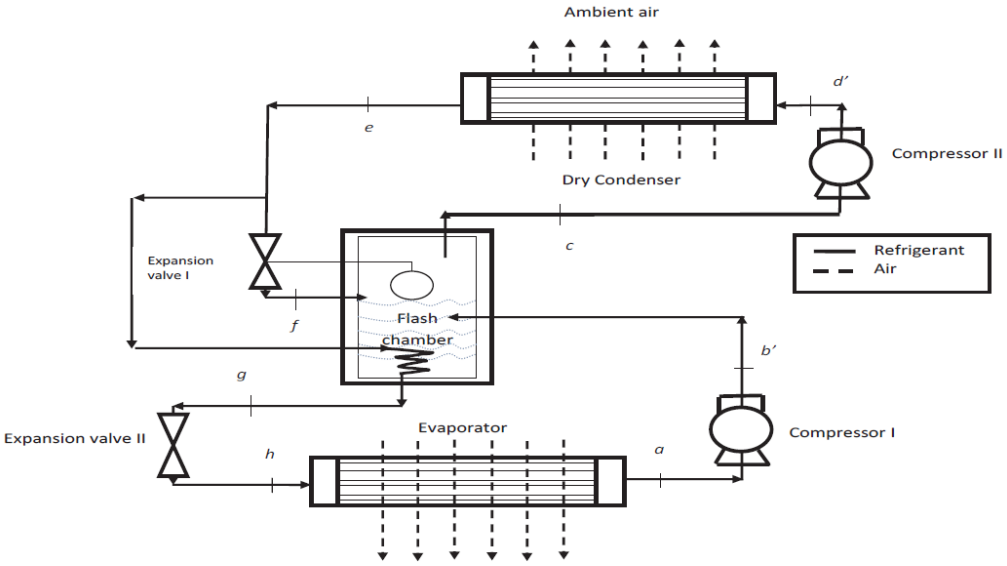

Figure 2.25: Multistage cycle [17]

2.3.5. REFRIGERANT SELECTION AND THERMOPHYSICAL MODELLING METHODS

The criteria used to select refrigerants for air-conditioning applications include performance, safety and environmental impact [49, p. 620]. Refrigerants can be characterised as single component, also known as pure refrigerants or azeotropic mixtures, or multi component, also called zeotropic mixtures. A single component refrigerant is associated with constant phase change temperature, while for multi component refrigerants a so-called temperature glide applies during phase change as opposed to truly isothermal heat transfer. Thermophysical properties of eight different refrigerants are presented in Table 2.6, with one key refrigerant to be highlighted being R134a which was used in developing the high speed compressor proposed by Aeronamic.

Table 2.6: Thermo-physical properties of various refrigerants [17]

Parameter	Latent heat ($kJ\,kg^{-1}$)		Sat. liquid specific heat ($kJ\,kg^{-1}\,K^{-1}$)		Sat. vapor specific heat ($kJ\,kg^{-1}\,K^{-1}$)		Sat. liquid density ($kg\,m^{-3}$)		Sat. vapor density ($kg\,m^{-3}$)	
Temperature (°C)	0	45	0	45	0	45	0	45	0	45
Refrigerant										
Ammonia	1262	1075	4.62	4.99	2.68	3.66	638.7	571.3	3.46	13.8
R134a	198.6	157.6	1.34	1.53	0.90	1.19	1295	1125	14.44	57.7
R1234yf	163.3	127.4	1.29	1.51	0.93	1.22	1177	1012	17.69	66.06
R22	205	160.5	1.18	1.38	0.75	1.05	1282	1106	21.24	75.5
R404A	165.8	112.9	1.39	1.85	1.00	1.65	1150	934	30.48	118
R407C	209.3	156.9	1.42	1.71	0.96	1.38	1236	1043	19.66	78.78
R410A	221.4	148.4	1.52	2.07	1.13	2.07	1170	943.8	30.58	120.3
R1234ze(E)	184.2	149.8	1.34	1.48	0.90	1.12	1241	1092	11.92	47.56

Working medium selection plays an important role in the performance of refrigeration units since the refrigerant is coupled to the type of thermodynamic cycle used. In the case of organic Rankine cycles used for electricity generation, criteria such as heat transfer area minimisation and heat recovery efficiency were proposed by Wang et al [56] part of a multi-objective optimisation model. The best performing refrigerants were determined to be R123 for the temperature range 100-180 °Celsius and R141b for temperature higher than 180°Celsius. Considering mobile refrigeration applications designed to meet both cooling and heating requirements, selection criteria such as energy efficiency are employed, with R134a as the most common refrigerant [57]. One factor affecting refrigerant selection are the regulations imposed by the European Parliament under the Kyoto protocol which recently placed a ban on fluoro-chemical refrigerants such as R134a with the chemical formula CH_2FCF_3. For automobile applications newer than 2017, the limit on the global warming potential was set at a maximum of 150 for 100 years integration. The R134a has a global warming potential of 1430 for the 100 years time horizon [6], thus exceeding the imposed limit. This should be taken into account when developing the new cycle due to the coupling between refrigerant selection and cycle performance.

Methods for calculating thermophysical properties of refrigerants were documented by Ding [58] while describing recent developments in simulation techniques for vapour compression cycles, resulting in two main categories: equation of state methods and advanced curve fitting models. For the first category accuracy is more important than stability and speed, while for the latter stability and speed are more important than accuracy. The equation of state method consist of a mathematical relation between pressure, specific volume and temperature. While it can be used for predicting thermodynamic properties of refrigerants, it is not suitable for simulations. The first method falling under the curve fitting category is the look-up table method, representing an improvement over the equation of state method. It makes use of a predefined set of properties for each refrigerant that can be accessed through simulation. Since the predefined properties are only stored for a limited number of points, linear interpolation is required to obtain the data of neighbouring state points. The disadvantage of this method is that it cannot meet the smooth requirement. Another curve fitting method is the explicit polynomial regression, based on a linear regression analysis using the least square method as the fidelity criterion [59]. The final curve fitting method to be discussed is the implicit regression and explicit calculation method. This allows to overcome the shortage in thermodynamic properties available for some refrigerants by first using implicit equations and then implementing analytical solutions to obtain explicit equations for the saturated liquid line, saturated vapour line, two phase region and superheated region [60].

[6] URL https://www.environment.gov.au/system/files/pages/78ecf1c3-b519-4bbb-b415-a45b89e51a9e/files/gwp-hfcs-and-blends.pdf [cited January 7, 2019]

3

METHODOLOGY

The design methodology used to set up a simulation model running a novel refrigeration unit can be split in a number of steps aimed at providing the required knowledge and tools needed to answer the research question. Before the design of the systems can commence, the boundary conditions are defined part of the requirements engineering process. The design procedure continues with importing a base template containing the geometric dimensions of the Airbus A320 platform into Sysarc, the design and simulation platform used in the current research. At this point the system architecture is empty and the designer can start configuring the desired network of subsystems to be used in the simulation. This is possible by selecting components and placing them at precise locations around the aircraft. This part is known as the subsystem modelling and integration at aircraft level.

The configuration of the refrigeration unit itself can start once the main requirement such as the cooling capacity of the system is known. This can be calculated by performing a heat load analysis which involves heat loads estimations and methods to compute heat transfers due to convection, convention and radiation.

To assess the impact of subsystems at aircraft level an electrical loads analysis is carried out. This way a budget for electrical power consumption can be created by accounting for various electronics categorised as either essential, utility or galley loads. Considering that electrical power is to be supplied by two engine driven generators, quantifying the electrical power demand of the system allows to assess the resulting secondary shaft power extraction which is directly related to the fuel consumption.

Once both the baseline model and the technology demonstrator models are configured, the verification process can begin. The chosen sensitivity study approach consists of the MOAT method used in order to assess the interaction between different parameters and identify those having a significant impact on results. Having verified both models a comparison study is established. For this the main aspects to be considered are the quantification of secondary power extraction in each case and the resulting trip fuel required for a baseline mission of 1000 nm and a payload of 12000 kg.

Figure 3.1: Baseline model

Figure 3.2: Technology demonstrator

3.1. REQUIREMENTS ENGINEERING

The requirements engineering process allows to identify the boundary conditions used to size the environmental control system(ECS) depending on the functionalities the system has to provide. The three main functions of the ECS considered in the current research programme are the following:

1. temperature control: the cabin temperature to be maintained between 18° and 23 °Celsius [1]
2. pressure control: a maximum cabin altitude of 8000 ft (0.75 bar) is imposed by regulations with lower cabin altitudes such as 6000 ft (0.81 bar) being currently achieved to increase passenger comfort [61]

3. ventilation control: to keep contaminants under control and to provide sufficient oxygen levels a minimum volume airflow rate of 10 ft^3/min is imposed by FAR requirements [62]. In practice US airliners provide ventilation rates of up to 40 ft^3/min [63]

Knowing from the start the ambient related operating conditions allows to size the systems accordingly. Since it is desired to have a system working throughout the complete operational envelope of the aircraft it must be ensured that the ECS works on ground as well as during flight. Two critical sizing conditions are selected, one hot day at ground level with T_{amb} = 39 °Celsius and P_{amb} = 1 bar and one hot day at cruise level at 35000 ft corresponding to T_{amb} = -35 °Celsius and P_{amb} = 0.2 bar. The latter sizing condition is directly linked to the proposed research question aimed to analyse the impact of different system architectures on trip fuel consumption for a common design mission of 1000 nm and 12000 kg payload. An overview of simulated conditions is presented in Table 3.1

Table 3.1: Summary of simulated conditions

Operation mode	**Temperature profile**	T_{amb}	p_{amb}	$N_{pax}+N_{crew}$
Ground	ISA Hot day	39 °Celsius	1 bar	180+6
Cruise	ISA Hot day	-35 °Celsius	0.2 bar	180+6

3.2. SYSTEM LEVEL MODELLING

The cabin is discretised in three compartments, namely the flight deck, the forward cabin compartment and the aft cabin compartment, as can be seen in Figure 3.3. Creating the system's architecture is done by placing the desired components at specific points across the aircraft, assigning permissible pathways and triggering a routing algorithm. The black lines running across the fuselage are called pathways and represent possible circuits along which connections between different components can be established. The actual connections such as pneumatic, hydraulic or electric lines are represented as green lines which go along the pathways, each having physical properties associated with it such as dimensions and weight.

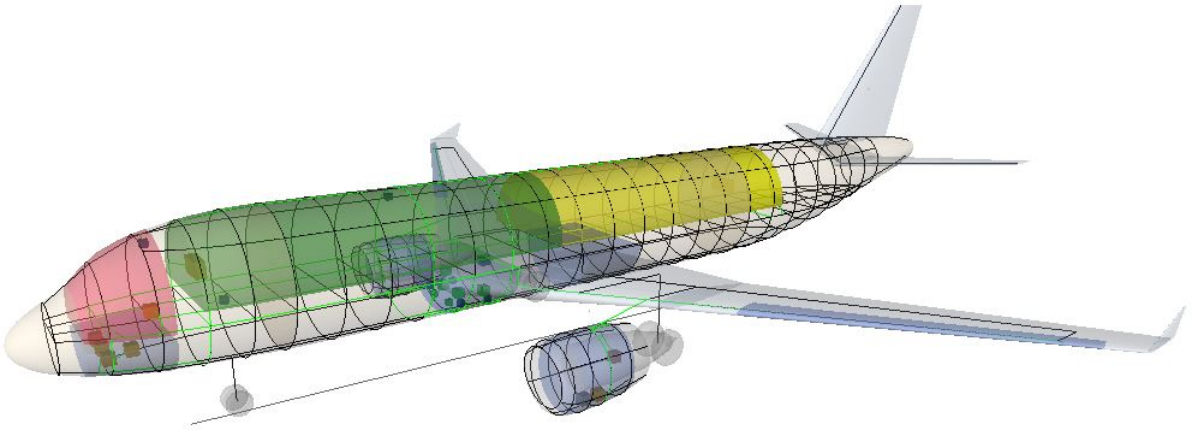

Figure 3.3: Sysarc 3D view showing the cabin discretisation in three zones, arrangement of pathways and localisation of components

BASELINE MODEL SYSTEM ARCHITECTURE

The integration of the baseline model refrigeration unit at aircraft level can be seen from the diagram presented in Figure 3.4. The secondary power extraction is done through the Out Rotational port of the powerplant, in this case the turbofan engine. Power is supplied to the cabin air compressor which feeds the In Pack pneumatic port of the ECS Pack. The ECS Pack engineering object contains thermodynamic data modelling a dual heat exchanger air cycle machine aimed to provide air conditioned for temperature and pressure through its pneumatic outlet port Out Pack towards the mix manifold system. One key parameter defined as a user input for the ECS Pack is the turbine exit temperature which represents the temperature of the fresh air to be directed towards the mix manifold where it comes into contact with recirculated air coming from the

regulated compartment.

A component schematic of the electrically driven air cycle machine eECS is presented in Figure 3.5 with a selection of critical points along the thermodynamic cycle summarised in Table 3.2 and plotted in the form of a pressure-enthalpy diagram in Figure 3.6.

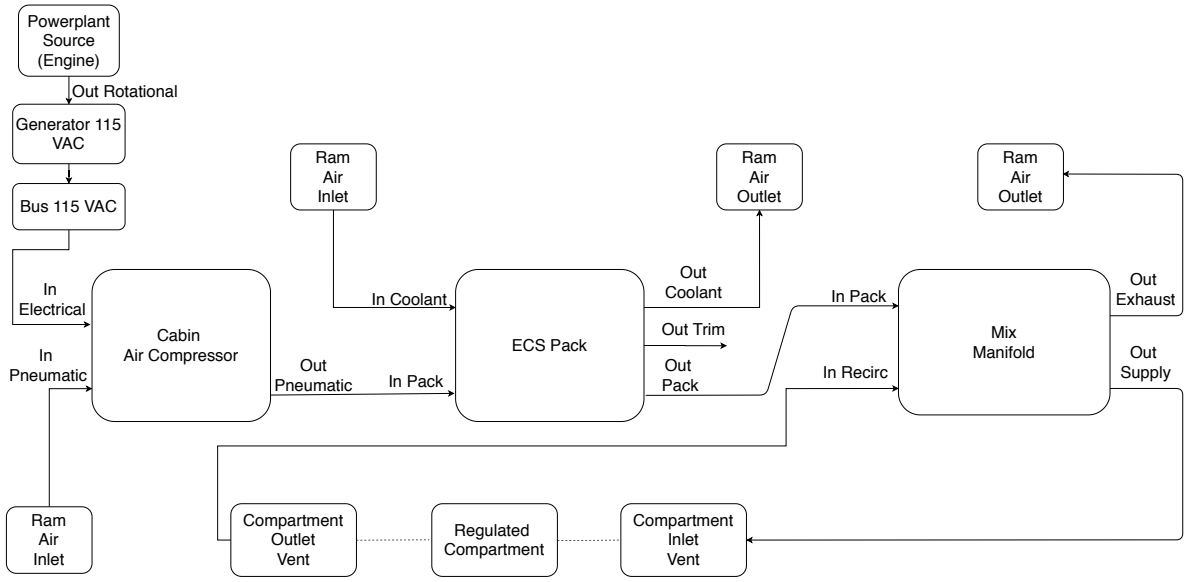

Figure 3.4: Integration of baseline model electrically driven air cycle machine at aircraft level

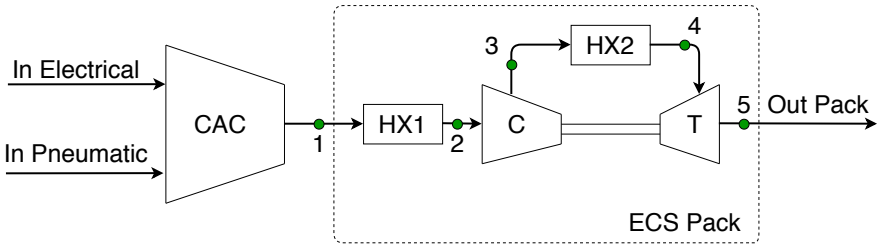

Figure 3.5: Electrically driven air cycle machine based ECS main components and localisation of critical points along the cycle

Table 3.2: Critical points along the electrically driven air cycle machine ECS

Point	Description
0	CAC inlet
1	CAC outlet; primary heat exchanger inlet
2	Primary heat exchanger outlet; auxiliary compressor inlet
3	Auxiliary compressor outlet; secondary heat exchanger inlet
4	Secondary heat exchanger outlet; cooling turbine inlet
5	Cooling turbine outlet

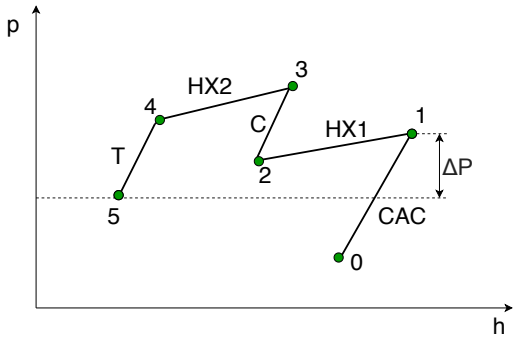

Figure 3.6: Pressure-enthalpy diagram of reverse Brayton air cycle machine refrigeration system with localisation of critical points along the cycle

The two heat exchangers HX1 and HX2 employed are compact heat exchangers with plate fin geometry, off

set strip fins and counter-flow arrangement. According to Zohuri [64, pp. 227-228] this is the most commonly used set-up for air to air heat exchangers due to higher achievable temperature change as compared to cross flow or parallel flow configurations. Having selected the geometry and flow arrangement of the heat exchanger, the remaining parameters of interest consist of the overall heat transfer coefficient, heat transfer area and relative pressure drop. The overall heat transfer coefficient value is set at 80 $W/m^2/K$ considering that for the chosen heat exchanger type typical values are in the range of 60 to 180 $W/m^2/K$ [65]. The heat transfer area is correlated to the exchanger effectiveness which is in the range of 75% to 85% for single pass counter-flow arrangements, the requirement which is met with a selected minimum heat transfer area of 15 m^2 [66, p. 605]. The pressure drop values can be assumed zero for ideal cycles however to have a more realistic model a 6% value was used which is in the range of 4% to 6% obtained from various textbook worked out examples for plate fin heat exchangers [66, pp. 608-630].

Air cycle machine matching has to be considered since the auxiliary compressor and the turbine of the air cycle system refrigeration unit are connected through the same shaft as depicted in Figure 3.7. Consequently the work output of the turbine must equal the work input to the compressor as shown by the energy balance presented in Equation 3.1. Taking into account the compressor and turbine efficiencies, the energy balance can be rewritten in the form of Equation 3.2. Once the temperatures at the key points of the systems are obtained and the enthalpy values estimated, Equation 3.3 can be used for verification purposes to make sure the energy balance of the air cycle system is preserved.

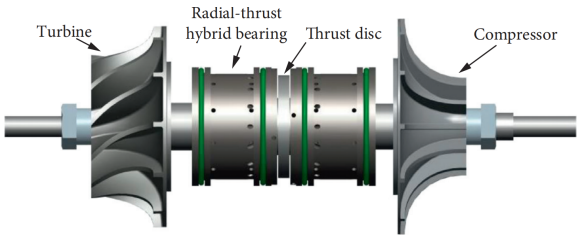

Figure 3.7: Air cycle machine rotor system, copied from [18]

$$\dot{W}_c = \dot{W}_t \tag{3.1}$$

$$\frac{\dot{m}c_p\,(T_3 - T_2)}{\eta_c} = \dot{m}c_p\,(T_4 - T_5)\cdot\eta_t \tag{3.2}$$

$$h_3 - h_2 = h_4 - h_5 \tag{3.3}$$

The mass flow rate of air to be provided by the cooling turbine denoted as $\dot{m}_{\text{Mix Manifold, Out Supply}}$ can be calculated using Equation 3.4 as a function of recirculation ratio ϵ_{recirc}. Starting from the energy balance presented in Equation 3.5, the temperature at the cooling turbine outlet is a function of the minimum allowable supplied temperature to the cabin and can be calculated using Equation 3.6

$$\dot{m}_{\text{ECS Pack, Out Pack}} = \dot{m}_{\text{Mix Manifold, Out Supply}}\,(1 - \epsilon_{\text{recirc}}) \tag{3.4}$$

$$(1-\epsilon_{recirc})\,\dot{m}\cdot c_p \cdot T_{\text{ECS Pack, Out Pack}} = \dot{m}\cdot c_p \cdot T_{\text{Mix Manifold, Out Supply}} - \epsilon_{recirc}\cdot\dot{m}\cdot c_p \cdot T_{\text{Cabin}} \tag{3.5}$$

$$T_{\text{ECS Pack, Out Pack}} = \frac{T_{\text{Mix manifold, Out Supply}} - \epsilon_{\text{recirc}}\cdot T_{\text{cabin}}}{1-\epsilon_{\text{recirc}}} \tag{3.6}$$

Considering the integration of systems at aircraft level, one interesting aspect to be mentioned is the relation between the powerplant, cabin air compressor, mix manifold and regulated compartment. The link between these components is the recirculation ratio, a parameter defined as part of the mix manifold. A zero recirculation ratio requires the cabin air compressor to work at full capacity resulting in a maximum air mass flow rate and electrical power demand. As the recirculation ratio is increased, the burden on the cabin air compressor is reduced as part of the air to be provided by the mix manifold is already available from the regulated

compartment, ultimately resulting in a decreased secondary power extraction from the engine. Additional information about the working principles behind the cabin air compressors are given in Section 3.4 part of the electric load analysis which provides guidelines aimed at constructing a power budget in order to assess the cabin air compressor power demand.

The efficiency of the air cycle machine refrigeration unit coupled to a cabin air compressor can be assessed by calculating the coefficient of performance defined as the cooling load divided by the work input as shown by Equation 3.7.

$$COP_{\text{System}} = \frac{\text{Cooling load}}{\text{Net work input}} = \frac{\dot{Q}_{\text{c}}}{\dot{W}_{\text{net}}} = \frac{\dot{Q}_{\text{cooling load}}}{\dot{W}_{\text{ram}} + \dot{W}_{\text{CAC}}} \tag{3.7}$$

The cooling load is calculated by multiplying the air mass flow rate by the enthalpy difference between the desired cabin temperature and the cooling turbine outlet temperature, as given by Equation 3.8. In practice this parameter corresponds to the total heat load which is obtained from the heat load analysis.

$$\dot{Q}_{\text{cooling load}} = \dot{m}(h_{\text{cabin}} - h_{\text{cooling turbine outlet}}) \tag{3.8}$$

The ram air work can be computed using Equation 3.9 multiplying the mass flow rate of air passing through the ram air inlet by the enthalpy difference across it.

$$\dot{W}_{\text{ram}} = \dot{m}(h_{\text{ram air outlet}} - h_{\text{ram air inlet}}) \tag{3.9}$$

The work done by the cabin air compressor can be computed using Equation 3.10 multiplying the mass flow rate of air passing through the cabin air compressor by the enthalpy difference across it.

$$\dot{W}_{\text{CAC}} = \dot{m}(h_{\text{CAC outlet}} - h_{\text{CAC inlet}}) \tag{3.10}$$

The pressure at the exit of the cabin air compressor resembles the pressure of bleed air used in conventional bleed air driven bootstrap refrigeration systems, this being the only source of energy driving the air cycle machine assembly. According to standard bleed driven environmental control systems the state of compressor bleed air varies according to the flight condition, from a minimum pressure of 50 psi (3.4 bar) during ground idle, up to 150 psi (10.3 bar) during cruise. By means of a pressure reducing shut-off valve, the bleed air pressure is reduced to around 40 psi (2.75 bar), representing the amount of pressure required to drive the air cycle machine [2, pp. 241-246]. This pressure value will be used in the simulation of the baseline model representing the boundary condition of the bootstrap cooling system, namely the pressure at the primary heat exchanger inlet. In order for the cabin air compressor to provide the required exit pressure of 2.75 bar, its pressure ratio will vary depending on the selected operating condition due to the ambient pressure variation with each flight case. Quantifying the resulting power demand allows to assess the secondary power extractions, thus contributing towards answering the proposed research questions.

TECHNOLOGY DEMONSTRATOR SYSTEM ARCHITECTURE

The integration of the the vapour cycle unit at aircraft level is presented in Figure 3.8. The design methodology behind the VCS Pack, shown schematically in Figure 3.9, is based on the calculation of variables required to quantify the thermophysical properties of the cycle at the critical points summarised in Table 3.3, allowing to draw the pressure-enthalpy diagram qualitatively shown in Figure 3.10. The refrigerant properties of R134a are stored in multidimensional data tables in the Sysarc Knowledge Designer database, the data consisting of enthalpy and entropy values in the range between -100° to 100°Celsius. The first set of data contains the properties along the saturation curve, while the second set is obtained from constant pressure tables.

Just as in the case of the air cycle machine configuration, the type of heat exchangers chosen for the vapour cycle system has to be justified. For both the condenser and the evaporator, air cooled compact heat exchangers are selected with a tube and fins geometry. This is considered to be the most common setup for air to liquid heat exchangers, more specifically with a plain flat fin arrangement which can achieve a lower pressure drop compared to other arrangements [66, pp. 697-698]. To simplify the simulation model the effects of pressure drop were not taken into account, thus the obtained system resembles an ideal vapour compression cycle.

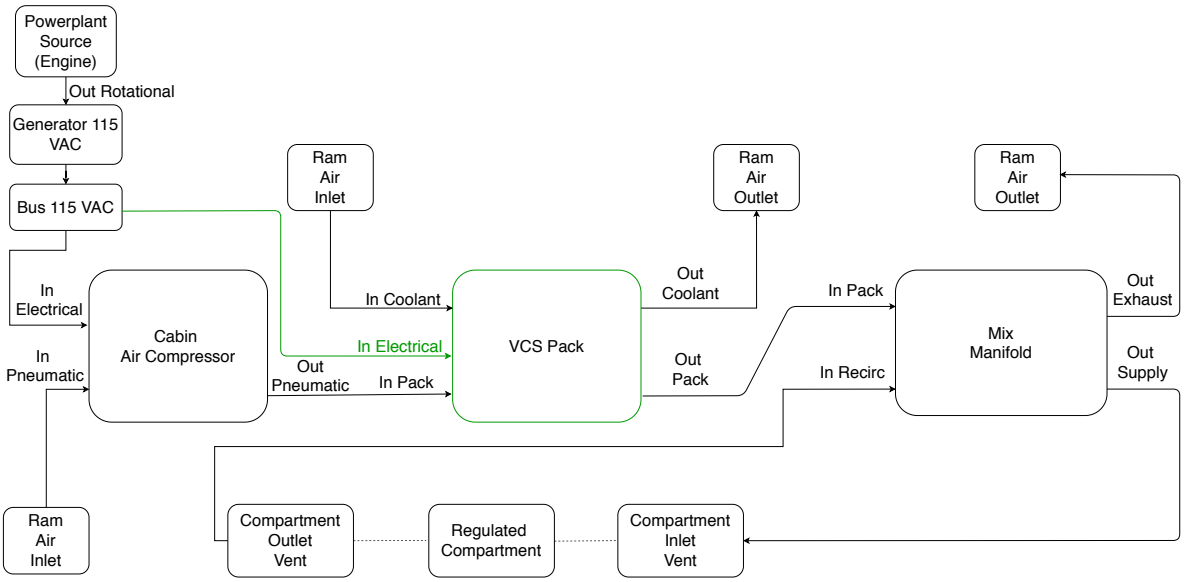

Figure 3.8: Integration of vapour cycle system at aircraft level

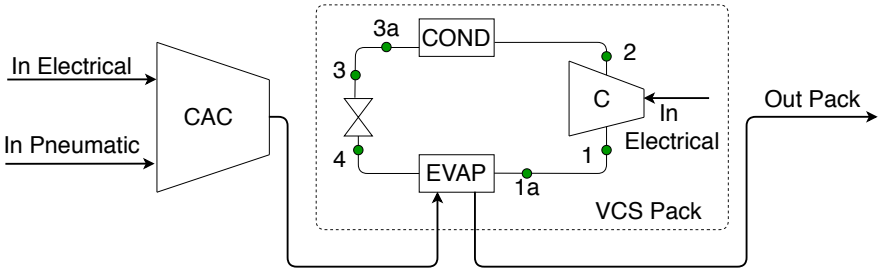

Figure 3.9: Vapour cycle refrigeration system main components and localisation of critical points along the cycle

Table 3.3: Critical points along the vapour compression cycle refrigeration system

Point	Description
1	Compressor suction
2	Compressor discharge (isentropic)
2s	Condensation dew point
3s	Condensation bubble point
3a	Condenser outlet
3	Including additional subcooling
4	Expansion valve outlet
4s	Evaporation bubble point
1s	Evaporation dew point
1a	Evaporator outlet

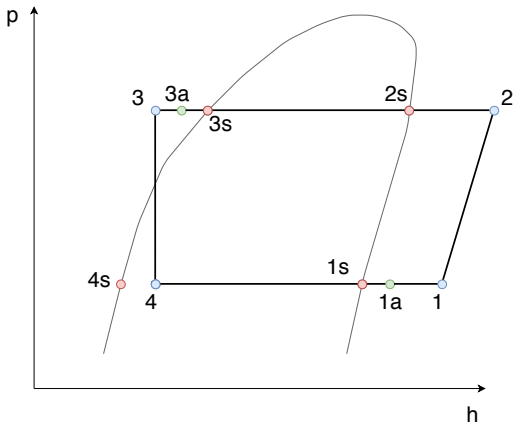

Figure 3.10: Pressure-enthalpy diagram of vapour cycle refrigeration system with localisation of critical points along the cycle

Using the condenser approach diagram qualitatively presented in Figure 3.11 the condensing temperature of the cycle can be chosen considering the rise in temperature of coolant for air cooled systems is in the range of 8-15 K [67, pp. 397-398]. For the hot day ground design case the ambient temperature is 39 °Celsius. Taking the critical 15 K rise in coolant temperature, this results in a coolant exit temperature of 54 °Celsius resulting in a minimum approach temperature difference of 4 °Celsius for a condensation temperature of 58 °Celsius.

For cruise conditions the condensation temperature of the cycle is kept fixed at 58 °Celsius, the only difference being the lower ambient coolant temperature, resulting in a higher approach temperature difference. Another parameter that can be obtained at this point is the refrigerant compressor discharge pressure. For a condensing temperature of 58 °Celsius the corresponding saturation pressure is 16 bar.

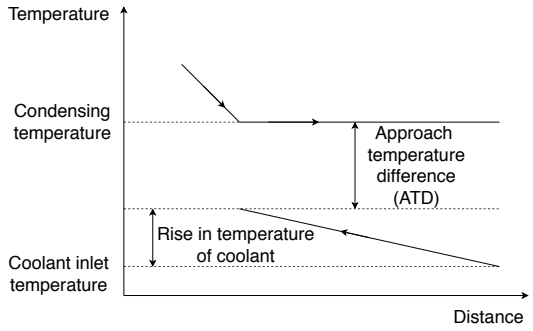

Figure 3.11: Condenser approach diagram

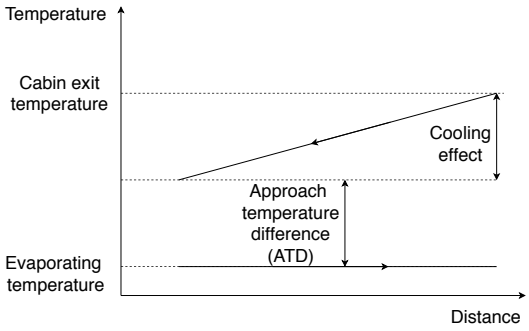

Figure 3.12: Evaporator approach diagram

For the evaporator design, the evaporator approach diagram qualitatively presented in Figure 3.12 is used to set the evaporating temperature. Considering the temperature regulation requirements of the system the cabin minimum temperature is 18 °Celsius. A minimum approach temperature of 5 K is recommended for water cooled evaporators with higher values applicable to air cooled evaporators [67, p. 405]. Setting the evaporating temperature at 0 °Celsius results in an approach temperature difference of 18 °Celsius. Having selected the evaporator temperature allows to obtain the refrigerant compressor suction pressure from the temperature table of R134a refrigerant. For an evaporating temperature of 0 °Celsius, the corresponding pressure equals 2.9 bar.

One variable of interest in case of the vapour cycle system is the global coefficient of performance, named COP_{System} which can be calculated using Equation 3.11, with methods for calculating the ram air work and the cabin air compressor work already introduced in the preceding section. The variable COP_{System} is defined by taking into account the effects of pressurisation and ram air work, thus it will be used when making a comparison between the air cycle system and the vapour cycle system.

$$COP_{\text{System}} = \frac{\text{Cooling load}}{\text{Net work input}} = \frac{\dot{Q}_{\text{c}}}{\dot{W}_{\text{net}}} = \frac{\dot{Q}_{\text{c}}}{\dot{W}_{\text{ram}} + \dot{W}_{\text{CAC}} + \dot{W}_{\text{refrigerant compressor}}} \tag{3.11}$$

When analysing the performance of the vapour refrigeration system on its own, the effects of pressurisation and ram air work can be ignored, allowing to defined a local coefficient of performance variable called COP_{Local}, as defined in Equation 3.12.

$$COP_{\text{Local}} = \frac{\text{Cooling load}}{\text{Net work input}} = \frac{\dot{Q}_{\text{c}}}{\dot{W}_{\text{net}}} = \frac{\dot{Q}_{\text{c}}}{\dot{W}_{\text{refrigerant compressor}}} \tag{3.12}$$

The refrigerant compressor modelling consists of quantifying the power required for isentropic compression using Equation 3.13. The refrigerant mass flow rate $\dot{m}_r$ is an user input while the enthalpies at the compressor discharge and suction points, namely h_2 and h_1, are extracted from superheated refrigerant tables which give a variation of enthalpy with temperature for a constant pressure.

$$\dot{W}_{\text{refrigerant compressor,is}} = \dot{m}_r \, (h_2 - h_1) \tag{3.13}$$

At this point a distinction between isentropic compression and effective power can be introduced. The latter can be calculated using Equation 3.14 which accounts for a certain isentropic efficiency η_{is} assumed to be 75 % as in the case of other centrifugal compressors [68].

$$\dot{W}_{\text{refrigerant compressor,ef}} = \frac{\dot{W}_{\text{refrigerant compressor,is}}}{\eta_{is}} \tag{3.14}$$

For the first design iteration the compression process is modelled as isentropic, thus the entropy at the compressor outlet equals that at the compressor inlet ($s_2 = s_1$). For a known compressor discharge pressure and entropy, the corresponding value of h_2 can be obtained from the superheated refrigerant table using linear interpolation.

In case of a non-isentropic compressor the enthalpy at the compressor discharge point can be calculated using the definition of isentropic efficiency as shown by Equation 3.15. The only unknown variable is then the actual enthalpy at the compressor discharge point which can be calculated using Equation 3.16.

$$\eta_{is} = \frac{h_{2is} - h_1}{h_2 - h_1} \tag{3.15}$$

$$h_2 = h_1 + \frac{h_{2is} - h_1}{\eta_{is}} \tag{3.16}$$

To understand how the cooling load is calculated the modelling of the evaporator is briefly introduced. The evaporator assembly is discretised in two zones allowing to account for both the two phase and the superheated zone of the cycle. The cooling capacity of the two phase zone can be calculated using Equation 3.17. The value for the enthalpy at the evaporation dew point h_{1s} corresponds to the saturated vapour enthalpy h_g which can be directly extracted from the R134a refrigerant properties table. At the expansion valve outlet the enthalpy h_4 has the same value as the enthalpy of the refrigerant prior to entering the expansion valve h_3 since the assumption of isenthalpic expansion applies. To simplify the preliminary calculation process, a system with no additional subcooling is considered thus allowing to set the enthalpy at the entrance of the expansion valve equal to that at the condensation bubble point h_{3s}. This allows to read directly the value of h_{3s} from the saturated liquid line. For a simple VCS cycle with no superheating the saturated vapour entropy at the compressor's inlet, s_1, can also be obtained from the refrigerant temperature table.

$$\dot{Q}_{\text{evap1}} = \dot{m}_r \, (h_{1s} - h_4) \tag{3.17}$$

The cooling capacity of the superheated zone is computed using Equation 3.18. The specific heat capacity values at constant pressure $c_{p,r}$ for the R134a refrigerant in superheated state are implemented in Sysarc according to data obtained from a constant pressure table, for a certain predefined pressure, in this case 2.9 bar. The degree of superheat ($T_1 - T_{1s}$) is a parameter calculated based on the selected T_1 and T_{1s} values. Other parameters that can be extracted from the constant pressure table are the enthalpy and entropy values at the compression suction point.

$$\dot{Q}_{\text{evap2}} = \dot{m}_r \cdot c_{p,r} \, (T_1 - T_{1s}) \tag{3.18}$$

The total cooling capacity of the evaporator Q_{evap_total} can be computed by adding the contributions from the two phase zone Q_{evap1} and from the superheated zone Q_{evap2} as shown by Equation 3.19.

$$\dot{Q}_{\text{evap\_total}} = \dot{Q}_{\text{evap1}} + \dot{Q}_{\text{evap2}} \tag{3.19}$$

To calculate the entropy at the evaporator inlet, s_4, first the quality of the refrigerant at the evaporator's inlet needs to be computed using Equation 3.20, then the entropy can be obtained using Equation 3.21.

$$x_4 = \frac{h_4 - h_f}{h_g - h_f} \tag{3.20}$$

$$s_4 = s_f + x_4 \cdot \left(s_g - s_f\right) \tag{3.21}$$

Although not required in calculating the coefficient of performance for cooling, the method used for the condenser modelling is also worth mentioning. The condenser assembly was discretised in three zones in order to account for the sensible heat transfer occurring as the refrigerant exits the compressor up to the condensation dew point ($\dot{Q}_{\text{cond1}}$), the latent heat transfer occurring inside the two phase region of the refrigerant saturation curve between the condensation dew point and the condensation bubble point ($\dot{Q}_{\text{cond2}}$) and the sensible heat transfer associated with the additional subcooling occurring in the saturated liquid region ($\dot{Q}_{\text{cond3}}$) [15].

In the first part of the condenser heat transfer is calculated using Equation 3.22. The condensing temperature has the same value at the condensation dew point and the condensation bubble point, thus T_{2s} is set equal to T_{3s}. At the compressor discharge point the temperature T_2 can be either calculated or set as an input. The calculation is possible by reading T_2 from a superheated refrigerant table as a function of pressure and entropy assuming the suction pressure of the compressor is set, the pressure ratio is known and the compression is isentropic. In the Sysarc model the $\dot{m}_r$, T_2 and T_{2s} variables are set as inputs that can be user defined, while the specific heat capacity $c_{p,r}$ for the R134a refrigerant in superheated state is taken is taken from a superheated chart as a function of temperature for a predefined discharge pressure.

$$\dot{Q}_{\text{cond1}} = \dot{m}_r \cdot c_{p,r} \left(T_2 - T_{2s}\right) = \dot{m}_r \cdot c_{p,r} \left(T_2 - T_{3s}\right) \tag{3.22}$$

In the two phase region of the condenser heat transfer can be computed using Equation 3.23 by taking the difference between the enthalpy at the condensation dew point and the enthalpy at the condensation bubble point.

$$\dot{Q}_{\text{cond2}} = \dot{m}_r \left(h_{2s} - h_{3s}\right) \tag{3.23}$$

The third part of the condenser is called the subcooler and represents an additional heat exchanger placed downstream the main condenser used to further cool down the saturated refrigerant before entering the expansion valve. The heat transfer in the subcooler can be computed using Equation 3.24 which takes into account the degree of subcooling of the system $(T_{3s} - T_3)$. Obtaining the enthalpy at the condensation dew point (point 3s) is straightforward as this point is located on the saturated liquid line and its value can be extracted from a temperature table at the desired temperature. However the subcooler outlet is located in the region of subcooled liquid. Whereas constant pressure tables are available for the region of superheated vapour, no data is available for the subcooled liquid zone. The trick of obtaining the enthalpy at this location is to consider the isenthalpic process associated with the expansion valve, meaning the enthalpy is constant between points 3 and 4. This means that the enthalpy at point 3 is the same as the enthalpy of saturated liquid at a temperature equal to that of the condensation bubble point minus the degree of superheat.

$$\dot{Q}_{\text{cond3}} = \dot{m}_r \left(h_{3s} - h_3\right) \tag{3.24}$$

Adding the contribution of the three condenser zones mentioned above, the total condensing capacity of the system can be estimated using Equation 3.25.

$$\dot{Q}_{\text{cond\_total}} = \dot{Q}_{\text{cond1}} + \dot{Q}_{\text{cond2}} + \dot{Q}_{\text{cond3}} \tag{3.25}$$

Having discretised the condenser and evaporator in multiple zones allows to model the effects of subcooling and superheating on the coefficient of performance. As a starting point a simple vapour cycle system with no subcooling and no superheating will be implemented and its impact at aircraft level will be assessed by quantifying the resulting power demand of the refrigerant compressor.

The method used to adjust the cooling load is to vary the refrigerant mass flow rate until the evaporator capacity matches the heat load requirement. While adding a degree of superheat and subcooling the variation in cooling capacity will be monitored while simultaneously varying the refrigerant mass flow rate in order to decrease the power consumption of the system. The reason behind adding a superheat degree involves protecting the refrigerant compressor by avoiding the phenomenon of wet compression, with superheat degrees in the range of 5-20 K considered desirable [67, p. 109]. Regarding subcooling this approach is desirable from a practical point of view in order to make sure the refrigerant enters the expansion valve in the form of subcooled liquid, with subcooling degrees in the range of 5-10 K used in industry [67, p. 108].

The mass flow rate of the refrigerant can be obtained by rewriting the energy balance over the evaporator in the form of Equation 3.26. The resulting expression is also known as the refrigerant side energy balance or the refrigerant enthalpy method. The parameter appearing in the nominator is cooling capacity of the system to be provided by the evaporator. The required cooling capacity is obtained from the cabin model explained in Section 3.3.

$$\dot{m}_r = \frac{\dot{Q}_{\text{evap\_total}}}{\Delta h_{evap}} \tag{3.26}$$

The pressure ratio of the system is obtained by dividing the discharge pressure of the compressor by its suction pressure, as shown by Equation 3.27.

$$\beta = \frac{p_2}{p_1} \tag{3.27}$$

COMPARISON OF THE TWO REFRIGERATION CYCLES FROM A THERMODYNAMIC PERSPECTIVE

To make a direct comparison between the baseline model and the technology demonstrator the power demand of the two configurations has to be quantified and compared. For the eECS configuration the energy source required to drive the air cycle machine is the pressure of the air coming from the cabin air compressor. In this case the cabin air compressor has to provide enough power to meet both the cooling and pressurisation requirements. In case of the VCS configuration the refrigeration effect is obtained by running the vapour cycle system which requires a certain amount of power for the refrigeration compressor. The cabin air compressor is then only used to meet the pressurisation requirements and is expected to have a lower power demand compared to the eECS configuration.

In order for the vapour cycle system to be more efficient than the air cycle machine configuration, the summation of cabin air compressor and refrigeration compressor power demand of the VCS has to be less than that of the power demand of the cabin air compressor of the eECS. Keeping all other parameters of the system constant, the variable of interest identified as having a direct impact on the cabin air compressor's power demand is its pressure ratio. An in depth investigation aimed at quantifying the power demand for the cabin air compressor is provided in the electrical load analysis presented in Section 3.4.

3.3. HEAT LOAD ANALYSIS

The amount of heat that needs to be removed by the environmental control system depends on the flight condition. The refrigeration system is configured according to the off-design condition consisting of the worst hot day scenario. Taking into account the internal heat generation and heat loss, a heat transfer model as shown in Figure 3.13 is used to account for the heat transfer due to solar and fuselage radiation, in addition to the heat transfer across the fuselage wall. The aim is to create a heat load budget in order to estimate the total heat load.

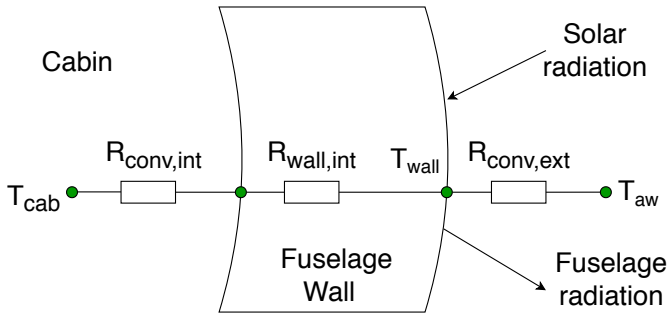

Figure 3.13: Cabin heat transfer model, adapted from Chakraborty et al. [19]

TOTAL INTERNAL HEAT LOAD

The *internal heat generation* can be estimated using Equation 3.28, having three components: the human metabolic heat load $\dot{Q}_p$, heat load due to in flight entertainment systems $\dot{Q}_{IFE}$ and heat load due to galley systems $\dot{Q}_{galley}$. The last two parameters are accounted for in the form of a miscellaneous heat load $\dot{Q}_{miscellaneous}$ which is set as an user defined input.

$$\dot{Q}_{gen} = N_{pax}\left(\dot{Q}_p + \dot{Q}_{IFE} + \dot{Q}_{galley}\right) = N_{pax} \cdot \dot{Q}_p + \dot{Q}_{miscellaneous} \tag{3.28}$$

TOTAL EXTERNAL HEAT LOAD

The heat transfer due to *solar radiation* can be computed using Equation 3.29, being defined as the product between the solar irradiance, q''_{solar}, and the irradiated area, A_s, taken as half of the total fuselage area. The solar irradiance is dependent on atmospheric conditions varying from 500 W/m^2 during a cloudy day at sea level up to 1350 W/m^2 at cruise altitude.

$$\dot{Q}_{solar,radiation} = q''_{solar} \cdot A_{s'} \tag{3.29}$$

TOTAL HEAT TRANSFER

As the cabin is in contact with the fuselage, the internal heat is dissipated to the fuselage external wall in the form of convection and conduction. This *internal heat loss* can be estimated by dividing the temperature difference between the wall and the cabin by the summation of the wall's conduction heat resistance $R_{cond,wall}$ and the internal convection heat resistance $R_{conv,int}$ as described in Equation 3.30.

$$\dot{Q}_{in,loss} = \frac{T_{cab} - T_{wall}}{R_{cond,wall} + R_{conv,int}} \tag{3.30}$$

The total *external heat loss* is a summation of heat transfers due to external heat convection and fuselage radiation as shown in Equation 3.31. The cabin model used in Sysarc is simplified by considering the fuselage radiation to be negligible, thus the total external heat loss depends only on the external heat convection, with T_{rec} representing the recovery temperature, a variable defined as a function of Mach number.

$$\dot{Q}_{ext,loss} = \dot{Q}_{ext,conv} + \dot{Q}_{fuselage,radiation} = \frac{T_{wall} - T_{rec}}{R_{conv,ext}} \tag{3.31}$$

TOTAL HEAT LOAD

Taking into account the total internal and external heat loads as well as the total heat transfer, a heat budget can be obtained which allows to calculate the total ECS thermal load by adding the contributions from each cabin zone followed by obtaining the sum. An overview of parameters used in the heat load budget calculation is presented in Table 3.4. The last three parameters in the table refer to the cabin wall thermal resistance consisting of the internal convection resistance, external convection resistance and the conductive resistance of the cabin wall. Based on a study taking into account different literature sources, the resulting parameters are selected [69].

Table 3.4: Summary of parameters used in heat load budget calculations

Parameter	Unit	Value
$N_{\text{pax}} + N_{\text{crew}}$	-	180+6
$\dot{Q}_p$	W	94
$\dot{Q}_{miscellaneous}$	kW	0
$\dot{Q}_{solar,radiation}$	kW	24(sea level); 30(cruise conditions)
$R_{conv,int}$	$W/m^2/K$	5
$R_{conv,ext}$	$W/m^2/K$	68.3
$R_{cond,wall}$	$W/m^2/K$	2.5

3.4. ELECTRICAL LOADS ANALYSIS

An electrical load analysis is a tool used to analyse the current power demand of onboard systems as a function of installed generating capacity. This is done by splitting electrical loads into galley, utility and essential loads, followed by differentiating the power demand along the various segments of the flight mission. The actual A320 electrical system is based on two 90kVA generators and an additional 90kVa generator connected to the auxiliary power unit. In the current design methodology it is assumed that the installed generating capacity is limited to the power provided by the engine mounted generators, thus not accounting for the APU capacity [70].

Another aspect to be considered is a possible power budget exceedance. Since the electrical platform used for this investigation is of a classical type (Airbus A320), while the architecture to be installed corresponds to the "more electric aircraft" type, there is a chance that the additional utility loads required to operate the refrigeration systems might exceed the maximum installed generator capacity. The remedy in this case would be to increase the nominal power of the generators, which is currently set to 90 kVa. According to the current industry state of the art power generating machines such as the 250 kVa generators installed on-board the Boeing 787, it is feasible to allow a power increase of each generator from 90 kVa up to a maximum of 250 kVa in order to accommodate the additional power demand required by the utility loads.

BASELINE MODEL

In case of the baseline model, the *utility loads* consist of two cabin air compressors each with its own power demand defined as part of the electrical port In115VAC. The resulting power demand of the cabin air compressor is a function of the variable *Electrical Power Input* defined as shown in Equation 3.32. The *motor drive efficiency* of electric motors is an indication of the energy lost associated with heat losses and friction during conversion from electrical to mechanical power. The motor drive efficiency is a function of rated output power, frequency and number of poles. According to NEMA guidelines covered by standard IEC 60034–30:2008, for an electrical motor operating at 60Hz with a rated power output in the range of 15 to 30 kW, motor drive efficiency values range between 90 % and 94 % [71, pp. 53-57].

$$\text{Electrical Power Input} = \frac{\text{Shaft Power Input}}{\text{Motor Drive Efficiency}} \tag{3.32}$$

While the mechanical efficiency is a user defined input, the variable *Shaft Power Input* is calculated as a function of compression work and mechanical efficiency, as shown in Equation 3.33.

$$\text{Shaft Power Input} = \frac{\text{Compression Work}}{\text{Mechanical Efficiency}} \tag{3.33}$$

The methods used to control the power demand of the cabin air compressor in order to alter the overall secondary shaft power extraction of the engine is to identify which parameters are used in the definition of the compression work. This is done by looking at the compression work formula which is a function of the following three parameters:

1. mass flow rate (can be controlled by altering the recirculation ratio of the mix manifold which is set at a value of 50%)
2. entry temperature (representing the boundary condition of the system and depending on the temperature of the stream coming from the upstream component, namely the ram air inlet)
3. exit temperature (a function of exit pressure of the cabin air compressor which is set at a value of 2.75 bar)

One method of controlling the power demand of the cabin air compressor is to alter the mass flow rate. The limitation of the model is that when all the components are connected together, the mass flow rate variable is no longer an input and cannot be varied directly, as it is a function of the mix manifold recirculation ratio.

Another method would be to look at the exit temperature required, which is a function of exit pressure. The exit pressure of the cabin air compressor has to be set at a pressure high enough to account for the pressure drop in the downstream components such as the primary and secondary heat exchangers, as well as accounting for any losses occurring in the compressor-turbine assembly of the air cycle machine.

TECHNOLOGY DEMONSTRATOR

When establishing the electrical load analysis of the technology demonstrator, the *essential loads* and *galley loads* are the same as the ones defined for the baseline model. The difference comes from the set-up of the utility loads, in this case the power demand of the two cabin air compressors as well as the power demand of the electrically driven vapour cycle compressor. The working principle of the cabin air compressor is the same as in the case of the baseline model, for which a detailed quantification of power demand was presented in the precedent subsection. Since in this case the cabin air compressor is only used to meet the pressurisation requirement its pressure ratio is expected to be less than in the case of the baseline model, thus resulting in a lower power demand.

Considering the electrically driven refrigerant compressor, the required electrical power input can also be computed as a function of shaft power input and motor drive efficiency. The shaft power input can be computed by dividing the required compression work by the mechanical efficiency. The compression work can be calculated by multiplying the refrigerant mass flow rate with the enthalpy difference across the refrigerant compressor.

3.5. POINT PERFORMANCE ANALYSIS

In order to generate a flight mission report, a flight profile is defined and the physical quantities at all time steps are calculated by means of a point performance analysis. The key parameters to be calculated include lift, drag, fuel flow, specific fuel consumption, rate of climb or specific air range of the aircraft for all flight cases. The three types of forces considered when deriving the equations of motion originate from gravity, aerodynamics and propulsion. When solving the equations of motion certain assumptions are made depending on the flight case considered. A set of assumptions applicable to an aircraft during the taxi flight phase can be differentiated from another assumption set corresponding to an aircraft operating in air part of flight segments such as take-off, cruise, descent and landing.

For an aircraft operating on ground the corresponding free body diagram is presented in Figure 3.14.

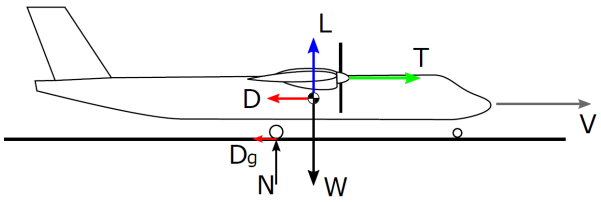

Figure 3.14: Free body diagram showing forces acting on aircraft during ground operations, copied from [20]

Force equilibrium in the horizontal direction is established using Equation 3.34 which equates the product of mass and acceleration of the vehicle to the summation of thrust, aerodynamic drag force and ground friction drag force D_g. The aerodynamic drag force D can be computed using Equation 3.35 with the aerodynamic coefficient C_D computed using Equation 3.36. The ground friction, D_g, can be computed using Equation 3.37 as the product of the runway friction coefficient μ and the normal force N. The lift coefficient C_L can be estimated using Equation 3.38.

$$F = m \cdot \frac{dV}{dt} = T - D - D_g \tag{3.34}$$

$$D = \frac{1}{2} \rho \cdot V^2 \cdot S \cdot C_D \tag{3.35}$$

$$C_D = C_{D,0} + k \cdot C_L^2 + \Delta C_D \tag{3.36}$$

$$D_g = \mu \cdot N = \mu (W - L) = \mu \left(m \cdot g - \frac{1}{2} \rho \cdot V^2 \cdot S \cdot C_L \right) \tag{3.37}$$

$$C_L = C_{L,0} + C_{L,\alpha} \cdot \alpha + \Delta C_{L,\text{flap}} \tag{3.38}$$

The free body diagram of an aircraft during flight is presented in Figure 3.15 with γ the angle between the velocity vector V and the horizontal plane, also called the flight path angle.

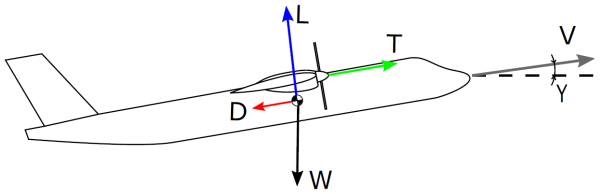

Figure 3.15: Free body diagram showing forces acting on aircraft during flight operations, copied from [20]

Force equilibrium along the velocity vector corresponds to Equation 3.39. The drag force can be computed using Equation 3.40 while the lift force can be computed using Equation 3.41.

$$F = m \cdot \frac{dV}{dt} = T - D - m \cdot g \cdot cos(\gamma) \tag{3.39}$$

$$D = \frac{1}{2}\rho \cdot V^2 \cdot S \cdot C_D \tag{3.40}$$

$$L = \frac{1}{2}\rho \cdot V^2 \cdot S \cdot C_L = m \cdot g \cdot sin(\gamma) \tag{3.41}$$

To solve the equations of motion corresponding to an aircraft during flight, different assumptions need to be made depending on each of the following flight segments:

1. **Take-off**: For the takeoff segment the flight path angle γ as well as the engine power rating are assumed to be constant. The takeoff segment is defined to end at an elevation of 1500 ft with respect to the airfield and a calibrated air speed (CAS) of 250 kt.

2. **Climb**: The climb segment is divided in two main parts. First the CAS is assumed constant up to the point when the aircraft reaches the cruise mach number which is set at 0.78 Mach. From that point onwards up to the top of climb defined as 35000 ft, the Mach number is assumed to be constant.

3. **Cruise**: For the cruise segment there are three possible modes available including a flat cruise, a climb cruise or a step cruise. The simulations performed are based on the flat cruise mode, meaning the altitude throughout the cruise segment is kept constant. The first assumption is a steady state motion, thus the acceleration is set equal to zero ($m \cdot \frac{dV}{dt} = 0$). The second assumption consist of maintaining a constant altitude throughout the complete cruise phase ($\gamma = 0$). In case a step cruise mode is selected, the altitude is maintained constant at a defined level up to a certain time, then it is increased to a higher altitude up to the end of the cruise segment.

4. **Descent**: For the descent segment a constant rate of climb (ROC) and calibrated air speed (CAS) are assumed.

5. **Landing**: For the airborne part of the landing segment the first assumption is a constant approach speed. The second assumption is a constant approach angle.

Solving the above equations of motion allows to calculate the total propulsive power, as defined by Equation 3.42, measured in either $N \cdot$ m/s, kW or hp(1000 $N \cdot$ m/s=1 kW=1.34 shp). The variable T represents the total thrust defined as the summation of thrust provided by the left and right powerplants.

$$P_{\text{propulsive}} = T \cdot V \tag{3.42}$$

The altitude variation with time for the chosen flight mission profile simulated is presented in Figure 3.16. It takes approximately 150 minutes to cover all the flight segments for a standard mission of 1000 nm, the cruise time duration being approximately 103 minutes. Additional flight profile related data can be found in Appendix B including the mach number and the propulsive power variation for both models for all flight segments.

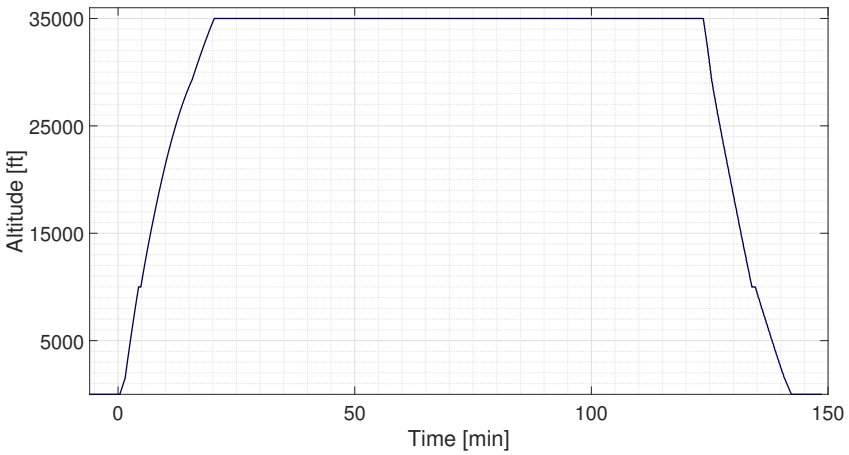

Figure 3.16: Altitude variation with time

4

VERIFICATION AND VALIDATION

Verification of the models is performed in the form of a sensitivity study during which the effects of each input variable on the output is analysed. Using the Morris One at A Time (MOAT) method the parameters belonging to the system architectures of both the baseline model and technology demonstrator can be verified. Another verification performed is a sensitivity study for secondary engine power off-takes to make sure the specific fuel consumption varies accordingly with varying power off-takes.

Validation of the vapour cycle system corresponding to the technology demonstrator was done using experimentally obtained data to assess the duty capacity of the system. This allowed to separately validate the condenser and evaporator capacities taking into account also the degree of superheat and subcooling. For the air cycle system the pressure level at the inlet of the air cycle machine was validated by comparing it to values taken from literature and experimental studies. Another aspect considered in the case of the air cycle system is the matching of the air cycle machine, required to satisfy the energy balance between the auxiliary compressor and the cooling turbine.

4.1. SENSITIVITY STUDIES USING MOAT METHOD

Once the system architectures have been defined and all the system's components are connected to each other it is important to identify what is the impact of parameters belonging to each component on the fuel consumption. By means of a Morris One At A Time (MOAT) study an uncertainty analysis is carried out allowing to classify parameters in the following three categories [72] [73]:

1. parameters having a negligible impact on results
2. parameters having large linear effects on results but not interactions with other parameters
3. parameters having large non-linear effects on results and/or interactions with other parameters

The MOAT study consists of calculating for each parameter of interest an elementary effect, a modified mean and a modified standard deviation. The standard deviation is an indication of non-linear effects and/or interactions with other parameters, while the mean quantifies the effect of the input on the output. Parameters with a low mean and low standard deviation have a negligible impact on results. Parameters with the standard deviation's order of magnitude less than that of the mean, but having a significant mean value have large linear effects on results but no interactions with other parameters. Parameters with a high mean and high standard deviation have a large non-linear effect on results and/or interactions with other parameters.

The first step of setting up the MOAT study consists of calculating the elementary effect, $d_i(x)$, using Equation 4.1. This is then used in the calculation of the modified mean, μ^*, as shown by Equation 4.2. Finally the modified standard deviation, σ^*, can be computed using Equation 4.3 [73].

$$d_i(x) = \frac{y(x + \Delta e_i) - y(x)}{\Delta} \tag{4.1}$$

$$\mu^* = \sum_{i=1}^{r} \frac{|d_i|}{r} \tag{4.2}$$

$$\sigma^* = \sqrt{\sum_{i=1}^{r} \frac{(d_i - \mu^*)^2}{r}} \tag{4.3}$$

4.1.1. SENSITIVITY STUDY FOR BASELINE MODEL SYSTEM ARCHITECTURE

The parameters used in the sensitivity study for the baseline model are summarised in Table 4.1. The selection was made by identifying parameters belonging to various system components that affect the functioning of the ECS Pack, thus potentially having an impact on the resulting fuel consumption. The results of the sensitivity study are presented in Figures 4.1 and 4.2.

Table 4.1: Sensitivity study data for baseline model

Parameter	Name	Unit	Default value	Lower bound	Upper bound
	Mix manifold				
1	Recirculation ratio	%	50	30	90
	Regulated compartment				
2	Air cycle time	min	2	0.5	2.5
3	Target temperature	° Celsius	20	18	26
4	Minimum supply temperature	° Celsius	2	0	8
5	Airflow per occupant	ft^3/min	10	10	50
6	Cabin pressure	bar	0.81	0.75	0.95
	ECS Pack				
7	HX pressure drop	%	6	2	10
8	HX overall heat transfer coefficient	$W/m^2/K$	150	60	180
9	HX heat transfer area	m^2	80	60	100
	CAC				
10	Exit pressure	bar	2.75	1	3

The air cycle time of the cabin compartment, parameter 2, has a standard deviation approximately two times higher than the mean indicating large non-linear effects on fuel consumption. As the air cycle time is defined as the period of time in which the entire compartment's air needs to be changed, a lower air cycle time corresponds to in an increased fresh mass air flow rate to be provided by the cabin air compressors, thus increasing their power demand. Extreme power consumption rates in excess of 100 kW were required for air cycle times less than one minute, while for air cycle times of over one minute the power demand from each cabin air compressor was stable around 80 kW.

Another parameter belonging to the cabin compartment and having a significant impact on results is the target temperature, parameter 3. Varying this parameter in the range between 18° and 26° Celsius results in a relatively high value of standard deviation in relation to the mean. This has to do with interactions with other components. A first interaction was observed with respect to the power demand of the cabin air compressor, where lower target temperatures for the cabin component resulted in increased power demand from the cabin air compressors as the mass flow rate of cold air coming from the ram air inlets had to be increased in order to provide the increased refrigeration effect, thus lowering the cabin temperature. It was noticed that the output temperature of the cabin air compressors was kept constant at approximately 64° Celsius. This could only be possible if refrigeration parameters belonging to the ECS Pack were affected. Further investigations showed that varying the target temperature of the cabin resulted in variations of the output temperature parameter belonging to the ECS Pack refrigeration unit.

The mix manifold recirculation ratio, parameter 1, has non-linear effects on the fuel consumption as well as an impact on other parameters. This has to due with the fact that the recirculation ratio affects the value of the total fresh air required to be provided by the cabin air compressors. This then affects the power demand of the cabin air compressors which translates into an impact on the secondary power extraction.

An example of a variable having large linear effects on results is the minimum supply air temperature of the cabin compartment, parameter 4. A trade-off between this parameter and the mass flow rate was identified. As the minimum supply air temperature was increased, an increase in the required mass flow rate of the mix manifold was recorded. Setting the minimum supply air temperature above 10° Celsius resulted in the mass flow rate coming from the Out Supply port of the mix manifold to exceed the imposed value of 5 kg/s, causing

no convergence at system level.

Parameter 5, the airflow per occupant, has been varied from the minimum FAR requirement of 10 ft^3/min up to 50 ft^3/min, a value just in excess of the industry attained level of 40 ft^3/min. From 10 ft^3/min to 30 ft^3/min, the ventilation demand was met with no significant impact on trip fuel. It was noticed that over 30 ft^3/min the required cabin air compressor power demand increased, resulting in higher recorded trip fuel values, however the overall impact of this parameter on trip fuel is considered to be negligible based on the low mean and standard deviation values as compared to other parameters.

Parameter 6, the cabin pressure, has been varied from a minimum FAR requirement cabin altitude of 6000 ft corresponding to a cabin pressure of 0.75 bar, up to a upper bound pressure value of 0.95 bar. According to the significant mean values and standard deviation's order of magnitude less than the mean, it can be said that this parameter has a large linear impact on results but no interaction with other parameters. This is confirmed by the fact that the higher the pressure selected in the cabin can be achieved by increasing the pressure ratio of the cabin air compressor, resulting in a linear increase in power demand thus a linear impact on trip fuel

The first parameter belonging to the ECS Pack included in the sensitivity study is the pressure drop of the heat exchangers, parameter 7. The recorded low values of modified mean (0.87) and standard deviation (0.2) indicate the pressured drop impact on trip fuel is negligible when varied between 2% and 10% as the additional work required by the cabin air compressor to overcome the resulting pressure drop values is minimal.

The second parameter of the ECS Pack investigated is the overall heat transfer coefficient, parameter 8. Varying this parameter in the range of 60 to 180 $W/m^2/K$ results in a maximum temperature change of 1 °Celsius achievable by the two heat exchangers, with no impact on trip fuel.

The third and last parameter of the ECS pack investigated is the heat transfer area of the heat exchangers, parameter 9. Varying this parameter in the range of 60 to 100 m^2 shows an insignificant variation of achievable temperature change of the heat exchangers, thus no impact on trip fuel.

For the cabin air compressor the exit pressure, parameter 10, the positioning of the standard deviation and modified mean indicate that this parameter has a large linear effect on results. As the air cycle system can operate under different conditions of cabin air compressor exit temperature, it is essential to quantify the effect on results for various pressure levels when calculating the trip fuel.

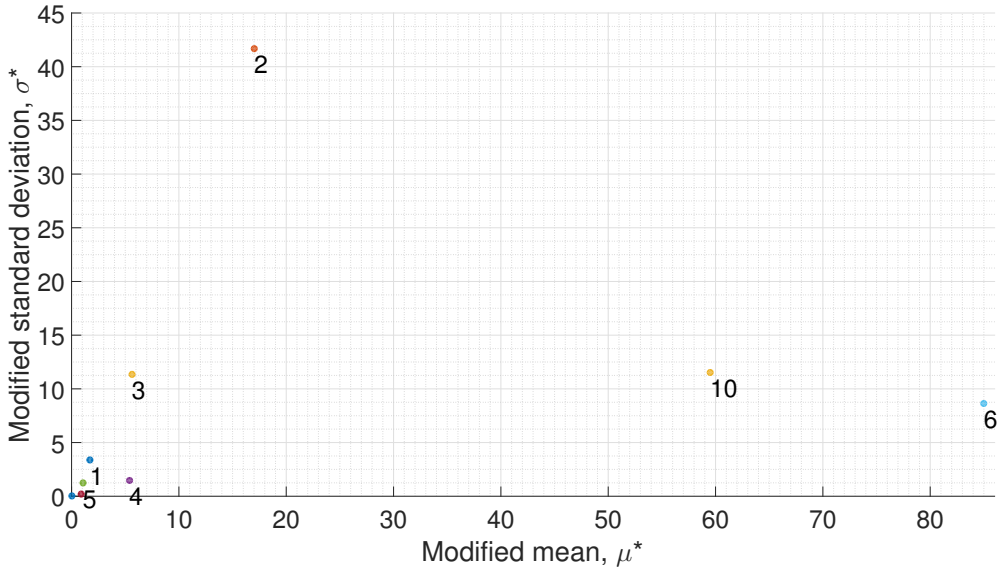

Figure 4.1: Sensitivity study for baseline model, analysing impact on the variable trip fuel

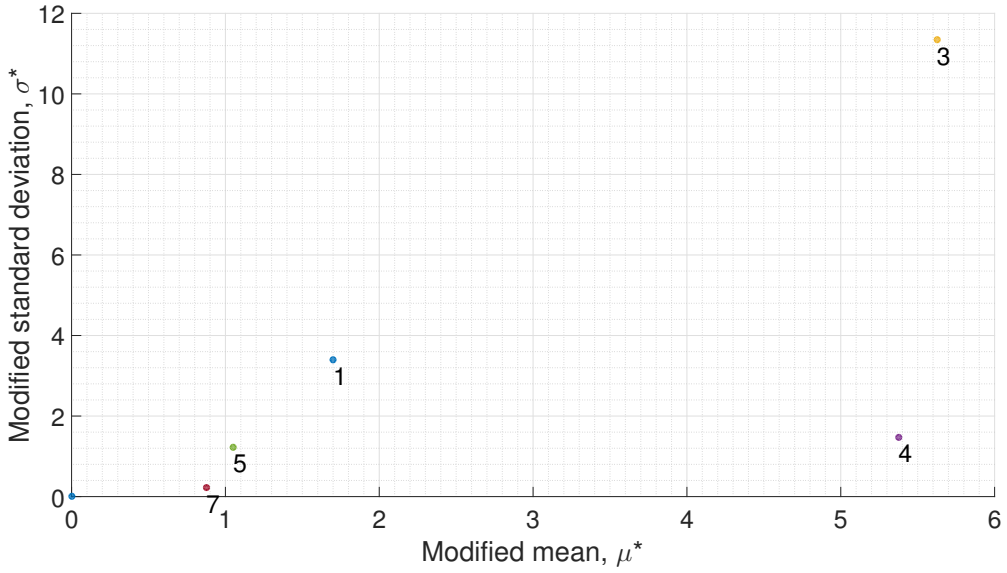

Figure 4.2: Sensitivity study for baseline model, analysing impact on the variable trip fuel

4.1.2. SENSITIVITY STUDY FOR TECHNOLOGY DEMONSTRATOR SYSTEM ARCHITECTURE

In case of the technology demonstrator the parameters selected for the sensitivity study are summarised in Table 4.2. Only parameters belonging to the VCS Pack were considered since the resulting system architecture is identical to that of the baseline model.

Table 4.2: Sensitivity study data for technology demonstrator model (VCS)

Parameter	Name	Unit	Default value	Lower bound	Upper bound
	VCS Pack				
1	Refrigerant compressor mass flow rate	kg/s	0.2	0.2	1
2	Refrigerant compressor isentropic efficiency	%	75	70	90
3	Degree of superheat	K	5	5	20
4	Degree of subcool	K	10	5	10
5	Evaporator capacity	kW	35	30	190

The first parameter studied is the mass flow rate of the refrigerant compressor which was varied between 0.2 kg/s and 1 kg/s. Considering Figure 4.3 the recorded standard deviation order of magnitude is less than that of a mean and the mean has a significant value, this allows to classify the refrigerant mass flow rate as a parameter having large linear effects on results.

Looking at Figure 4.4, the second parameter studied is the refrigerant compressor isentropic efficiency which was varied from 70 to 90 %. The resulting low modified mean and standard deviation values indicate that this parameter has a negligible impact on results.

The third parameter studied, the degree of superheat, was varied from 5 to 20 K showing both an increased in cooling capacity and work done by the compressor. In absolute terms the increase in cooling capacity was much greater than the increase in work done by the compressor. The impact on fuel consumption is negligible as shown by the low standard deviation and mean values.

Parameter 4, the degree of subcool, was varied from 5 to 10 K. As adding a subcooler increases the cooling capacity of the system with no effect on compression work, this parameter has a negligible effect on trip fuel as confirmed by the recorded low standard deviation and mean values.

Regarding parameter 5, the evaporator capacity, there are various strategies leading to its augmentation, including adding a degree of superheat, adding a degree of subcooling or increasing the refrigerant mass flow rate. For the sensitivity study the latter strategy is chosen, namely the increase in refrigerant mass flow rate and monitoring the resulting power demand of the compressor in order to see the effect on trip fuel.

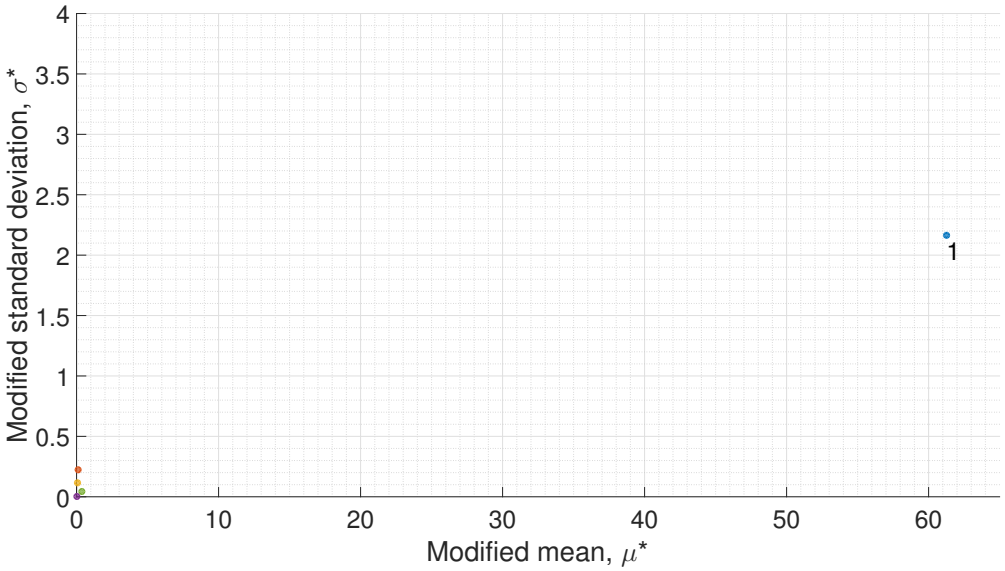

Figure 4.3: Sensitivity study for technology demonstrator, analysing impact on trip fuel

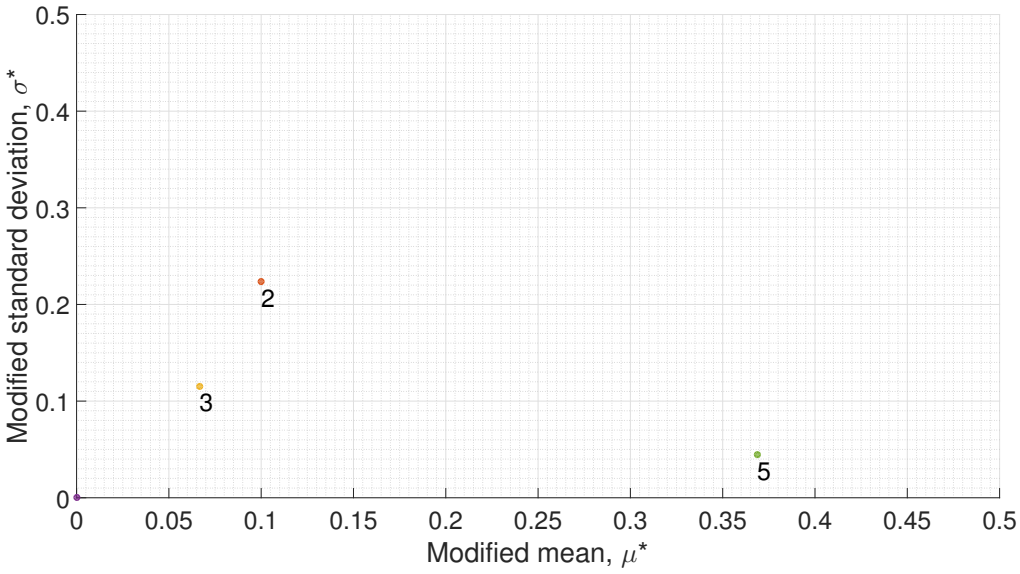

Figure 4.4: Sensitivity study for technology demonstrator, analysing impact on trip fuel

4.2. SENSITIVITY STUDY OF ENGINE OFF-TAKES

To make sure the performance dataset of the CFM56-A1 engine model used in the simulation takes into account secondary off-takes, a sensitivity study was carried out by varying the Out Rotational power from 0 to 300 shp and recording the resulting values of fuel flow, total thrust and specific fuel consumption. Knowing the actual fuel flow at zero extraction it is convenient to express the Δ Fuel flow for each extraction level using Equation 4.4. Table 4.3 presents the recorded values which are used to plot specific fuel consumption as a function of shaft power off-takes shown in Figure 4.5. The recorded specific fuel consumption ranging from

16.71 g/(kN.s) to 17.11 g/(kN.s) are in accordance with the fuel consumption of the Airbus A320 during cruise flight which ranges between 15.4 g/(kN.s) and 18.9 g/(kN.s) [74].

$$\Delta\text{Fuel flow} = \text{Fuel flow} - \text{Fuel flow at zero extraction} \tag{4.4}$$

Table 4.3: Shaft power off-takes sensitivities on specific fuel consumption

Out Rotational [shp]	Fuel Flow [kg/s]	ΔFuel flow [kg/s]	Total Thrust [kN]	SFC [g/(kN.s)]
0	1.44	0	85.88	16.71
50	1.44	0.58 E-2	85.88	16.78
100	1.45	1.16 E-2	85.88	16.85
150	1.45	1.73 E-2	85.88	16.91
200	1.46	2.31 E-2	85.88	16.98
250	1.46	2.88 E-2	85.88	17.05
300	1.47	3.46 E-2	85.88	17.11

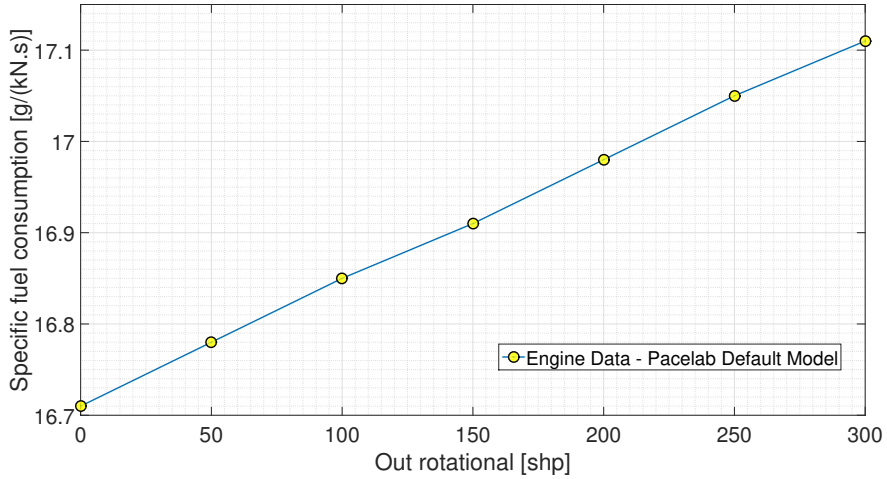

Figure 4.5: Variation of specific fuel consumption with secondary shaft power off-takes

To make sure the change in specific fuel consumption resembles the performance of an actual engine, the slope of the line from Figure 4.5 has to be verified. This was done by considering the variation of the specific fuel consumption correction factor of the engine data belonging to the Pacelab default model engine deck and comparing it to data obtained from a second engine deck serving as the verification model. The same verification engine deck as used in a previous study was selected as it contained data in an altitude range from 0 to 39000 ft as a function of Mach number varying from 0 to 0.8 [69]. In Pacelab Sysarc the specific fuel consumption taking into account system architecture is computed by taking the value of SFC from the APD model and altering it by means of a correction factor defined in a multidimensional data table (MDT). Both the thrust correction factor, f_{sfc} and the fuel flow correction factor, f_{fuelflow} are defined part of the engine performance deck MDT as a function of altitude, mach number, shaft power and bleed air extraction levels. It is then possible to calculate the SFC correction factor, f_{sfc}, using Equation 4.5 and plot its variation as a function of shaft power extraction as shown in Figure 4.6. Although the results show a step difference between the Pacelab default model and the verification model due to the fact that the two engine performance datasets are not identical, a similar trend of f_{sfc} variation with out rotational power is observed. Even though a small error remains, its influence on the trip fuel results will be negligible since it will be present in both the baseline model and technology demonstrator.

$$f_{\text{sfc}} = \frac{f_{\text{fuelflow}}}{f_{\text{thrust}}} \tag{4.5}$$

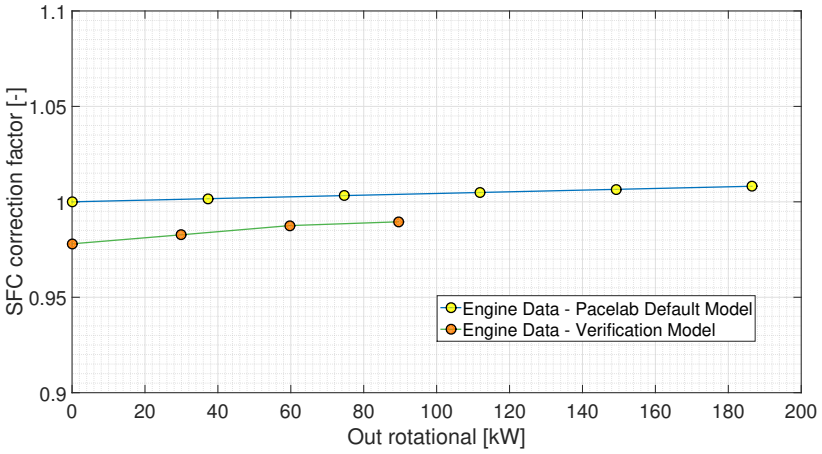

Figure 4.6: Variation of SFC correction factor with secondary shaft power off-takes

4.3. VALIDATION OF VAPOUR CYCLE SYSTEM

Validation of the refrigeration system unit is achieved by comparing data obtained from the engineering object modelled in Sysarc with experimental data provided by a commercial software for preliminary design of refrigeration applications called CoolSelector offered by Danfoss. A summary of the validation data used during the validation process is presented in Table 4.4.

4.3.1. VALIDATION OF EVAPORATOR MODEL

The two phase part of the evaporator, named EVAP1 in Sysarc, is validated by comparing its cooling capacity with that predicted by Coolselector. Validation input data is the same for both Sysarc and Coolselector, namely a refrigerant mass flow rate of 0.6 kg/s, an evaporation temperature of 0° Celsius and a condensation temperature of 58° Celsius. Comparing the obtained cooling capacity from Coolselector of 68.08 kW with that obtained from the Sysarc model of 68.6 kW, a difference of only 0.76 % is noticed.

The overall evaporator's cooling capacity is validated by adding a degree of superheat to the system. In Coolselector this variable is called "Useful superheat". A similar variable of type temperature interval was defined in Sysarc under the name *deltaT_superheat*. Setting the superheat value to 10 K results in a cooling capacity of 73.45 kW predicted by Coolselector and a value of 73.85 kW calculated in Sysarc, with a difference of only 0.54 % between the two.

4.3.2. VALIDATION OF CONDENSER MODEL

The condenser model is validated by comparing the heating capacity obtained in Coolselector with that obtained in Sysarc. For the same input set of data as for the validation of the evaporator, namely a refrigerant mass flow rate of 0.6 kg/s, an evaporation temperature of 0° Celsius and a condensation temperature of 58° Celsius, a heating capacity predicted in Coolselector is obtained as 98.07 kW for a specified compressor discharge temperature of 75° Celsius. Using the same data in Sysarc, a condenser capacity of 97.94 kW is obtained, resulting in a difference of only 0.13 % between the two models.

Table 4.4: Validation data for both the condenser and evaporator models

Parameter	Unit	Sysarc	Coolselector	Percentage difference
$\dot{m}_r$	kg/s	0.6	0.6	-
T_{1s} (Evaporation temperature)	° Celsius	0	0	-
T_{3s} (Condensation temperature)	° Celsius	58	58	-
T_2 (Compressor discharge temperature)	° Celsius	75	75	-
Q_{evap1} (Cooling capacity)	kW	68.60	68.08	0.76 %
Q_{evap_total} (Cooling capacity)	kW	73.85	73.45	0.54 %
Q_{cond_total} (Heating capacity)	kW	97.94	98.07	0.13 %

4.4. VALIDATION OF AIR CYCLE SYSTEM

For the air cycle system validation the pressure level at the inlet of the air cycle machine, p_1, was compared to that obtained from literature and experimental studies for different operating scenarios. As a first estimate, the pressure at the exit of the cabin air compressor was set to resemble that of conventional bleed air. The pressure of the bleed air is a function of the operating condition of the engine, reaching up to 10.3 bar during cruise. After passing through a pressure reducing valve, bleed air is usually supplied for operating secondary pneumatic systems such as the air cycle machine with a pressure value of 2.75 bar [2, pp. 241-246]. From literature worked out examples analysing the thermodynamic performance of bootstrap air-refrigeration cycles for aircraft applications, the actual pressure at the inlet of the air cycle machine is set equal to 4 bar [67, pp. 79-82]. Another case considered is a study of the transient model validation of an air cycle machine for which the pressure level at the boundary condition of the air cycle machine equals 1.73 bar [75]. Having identified various pressure levels linked to the operating of the air cycle machine and knowing from the verification study that the cabin air compressor exit pressure is a parameter having large linear impact on results, the impact of various pressure levels on the trip fuel will be investigated when making a comparison between the baseline model and technology demonstrator.

Table 4.5: Validation data for air cycle machine pressure level at inlet

Parameter	p_1		
Value	1.73 bar [75]	2.75 bar [2, pp. 241-246]	4 bar [67, pp. 79-82]

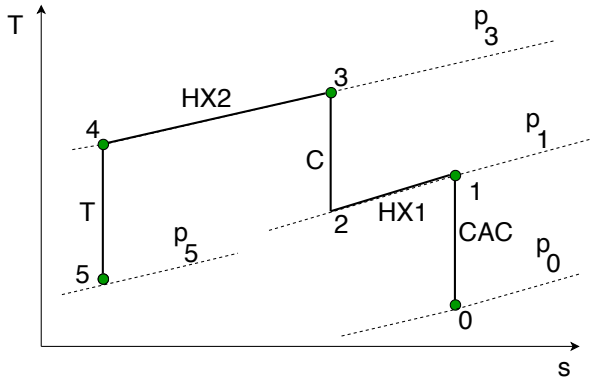

Figure 4.7: T-s diagram air cycle machine

To make sure the air cycle machine respects the work balance required between the auxiliary compressor and the cooling turbine, the Equations 4.6, 4.7 and 4.8 must be respected. This verification is carried out based on the data presented in Table 4.6, comparing data from the simulation model to that obtained from a textbook worked out example.

$$\dot{W}_c = \dot{W}_t \tag{4.6}$$

$$\frac{\dot{m}c_p(T_3 - T_2)}{\eta_c} = \dot{m}c_p(T_4 - T_5)\eta_t \tag{4.7}$$

$$h_3 - h_2 = h_4 - h_5 \tag{4.8}$$

The aim is to start from the same boundary conditions, namely a pressure level of 4 bar at the inlet of the air cycle machine and a temperature value of 128 K at the end of the cooling turbine, and verify if the work balance from Equation 4.8 is satisfied. The turbine efficiency in case of the simulation model was set to 99 % instead of 100 % to avoid a non converge error. The results obtained in Sysarc show the pressure at the high level point of the cycle, p_3, closely resembles the value used for verification purposes. Due to lack of available data regarding the heat exchangers used in the verification model, the heat exchanger area of the simulation model was continuously varied until the enthalpy values at key parameters resembled those of

the verification model. The resulting heat exchanger area allowing to compare the two models was identified as 14 m^2. Another aspect considered is the difference across the accessory compressor that must be equal to that across the cooling turbine. Since this equality holds true for both models it can be said that the air cycle machine used in the simulation model works as expected, thus guaranteeing the air cycle machine matching is met.

Table 4.6: Air cycle machine matching data

Parameter	Unit	Sysarc	Textbook example [67, pp. 79-82]	Percentage difference
p_1	bar	4	4	-
η_c	%	100	100	-
η_t	%	100	99	1 %
p_3	bar	19.5	19.4	0.51 %
h_2	kJ/kg	291	300	2.99 %
h_3	kJ/kg	457	471	2.97 %
h_4	kJ/kg	295	300	1.67 %
h_5	kJ/kg	128	128	-
h_3 - h_2	kJ/kg	166	171	2.92 %
h_4 - h_5	kJ/kg	166	171	2.92 %

5
RESULTS

The first part of the results consist of the data obtained from the heat load analysis. This provides the total heat load for ground and cruise operations, representing the cooling load used to size both the air cycle and the vapour cycle systems.

Data belonging to the newly designed vapour cycle unit as well as the air cycle system is investigated in the form of a thermodynamic cycle analysis. For the technology demonstrator this allows to quantify the pressure and specific enthalpy at key points in the thermodynamic cycle such as the compressor suction and discharge, condensation dew point, condenser outlet and expansion valve outlet. Having control over system parameters results in sufficient data required to execute a performance analysis in order to see what is the coefficient of performance of the system running at a specific cooling capacity and also what is the associated work done by the compressor.

For the baseline model the variables used to draw the p-h diagram of the cycle are quantified at all stages of the cycle starting from the properties of air collected through the ram air inlet up to the temperature, enthalpy and pressure of air provided by the cooling turbine.

The electrical load analysis serves as a base for comparison between the two systems. Here the emphasis is placed on establishing a power generation architecture that can be applied to both the baseline model as well as to the technology demonstrator. The key parameters quantified belong to one of the three main classes such as utility, essential and galley loads. The aim here is to set up a platform of identical galley and essential loads, allowing to focus on the differences in power consumption of the utility loads, namely the power consumption of the cabin air compressors as well as that of the refrigerant compressor.

Another investigation performed is the comparison in trip fuel between the baseline model and technology demonstrator, allowing to see which one is more efficient from a flight mission stand point of view. As a classification of assumptions were already established using the MOAT study method, the effect of parameters having a large impact on results is investigated.

5.1. HEAT LOAD ANALYSIS

Taking into account all the heat transfer mechanisms mentioned in Section 3.3 except the heat transfer due to fuselage radiation which is assumed to be negligible, a heat transfer budget can be created with differentiation for the cockpit and two cabin zones as presented in Table 5.1. The heat budget contains data for both ground and cruise conditions resulting in a total heat load of 46.3 kW at ground and 40.4 kW at cruise.

Table 5.1: Heat load budget

Compartment	**Total internal heat load [kW]**		**Total external heat load [kw]**		**Total heat transfer [kW]**		**Total heat load [kW]**	
	Ground	Cruise	Ground	Cruise	Ground	Cruise	Ground	Cruise
Flight deck	0.19	0.19	1.50	2	0.37	-0.55	2.06	1.64
Cabin compartment forward	8.65	8.65	11.25	14	2.22	-3.30	22.12	19.37
Cabin compartment aft	8.65	8.65	11.25	14	2.20	-3.28	22.10	19.37
Sum	17.5	17.5	24	30	4.8	-7.1	46.3	40.4

5.2. THERMODYNAMIC CYCLE ANALYSIS

The thermodynamic cycle analysis consists of quantifying parameters such as pressure and enthalpy at key points. This is performed for both the baseline model and technology demonstrator.

5.2.1. BASELINE MODEL

In case of the baseline model the thermodynamic cycle analysis serves to obtain the pressure and enthalpy data along the critical points of the cycle with the aim of quantifying the required cabin air compressor's power demand which has a direct impact on the fuel consumption. The thermodynamic data summarised in Table 5.2 is obtained using the primary and secondary heat exchanger properties selected in the methodology section.

Using the thermodynamic data summarised in Table 5.2 the pressure-enthalpy diagrams obtained are plotted in Figure 5.1 for the ground condition and in Figure 5.2 for the cruise segment. For both cases the turbine outlet operating conditions are fixed at 0.81 bar and 257 K while the cabin air compressor inlet conditions vary from 1.02 bar at ground level to 0.35 bar at cruise altitude.

The resulting performance calculations aimed at quantifying the coefficient of performance of the cycle are summarised in Table 5.3, showing a COP of 0.26 for the ground condition and 0.12 for the cruise condition. The coefficient of performance is lower in case of the cruise condition as it also accounts for pressurisation, with higher compression power required by the cabin air compressor during cruise.

Table 5.2: Baseline model thermodynamic analysis

Point	**Description**	**Ground**		**Cruise**	
		p [bar]	h [kJ/kg]	p [bar]	h [kJ/kg]
0	CAC inlet	1.02	313	0.35	266
1	CAC outlet; primary heat exchanger inlet	2.75	433	2.75	519
2	Primary heat exchanger outlet; auxiliary compressor inlet	2.58	351	2.58	313
3	Auxiliary compressor outlet; secondary heat exchanger inlet	6.36	488	7.60	465
4	Secondary heat exchanger outlet; cooling turbine inlet	5.98	394	7.20	409
5	Cooling turbine outlet	0.81	257	0.81	257

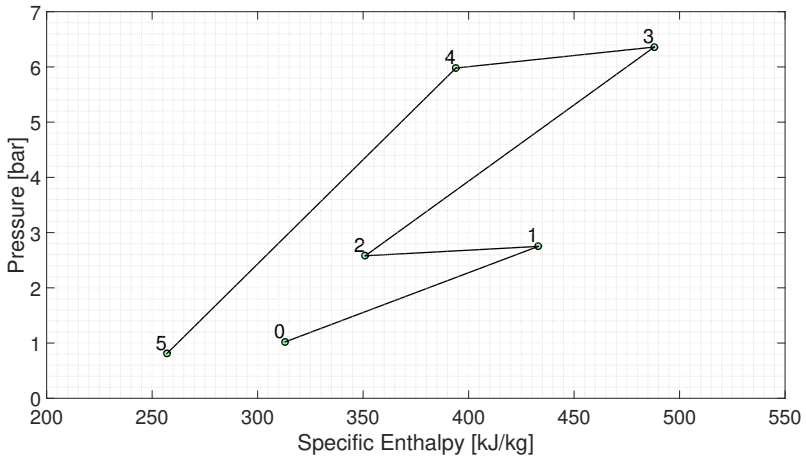

Figure 5.1: Baseline model p-h diagram for operation at ground hot day

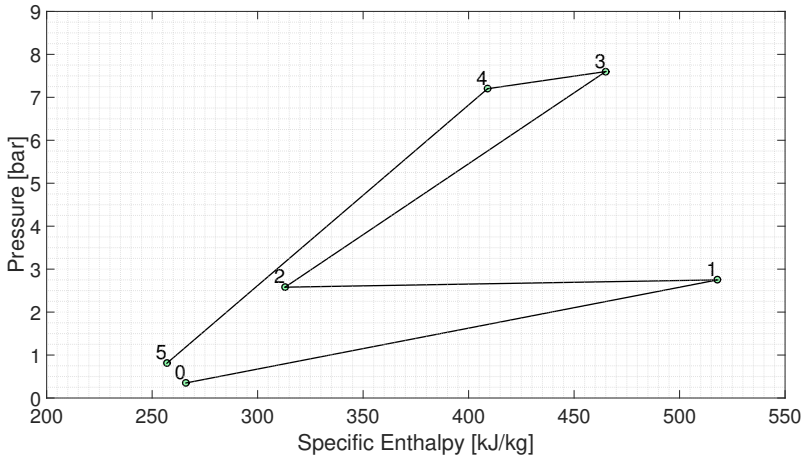

Figure 5.2: Baseline model p-h diagram for operation at cruise hot day

Table 5.3: Coefficient of performance calculations for baseline model

Parameter	Unit	Ground	Cruise
$\dot{Q}_c$	kW	46.28	40.36
$\dot{W}_{ram}$	kW	0.77	32.44
$\dot{W}_{CAC}$	kW	173.56	316.80
COP_{System}	-	0.26	0.12

5.2.2. TECHNOLOGY DEMONSTRATOR

For the technology demonstrator three different designs are investigated. The first one is a simple VCS cycle. The second one is a superheated cycle. The third is a subcooled cycle. The fourth is a superheated and subcooled cycle.

SIMPLE VCS

A simple vapour cycle system with an evaporation temperature of 0° Celsius, a condensation temperature of 58° Celsius, a compressor suction pressure of 290 kPa and a compressor discharge pressure of 1600 kPa represents the base configuration. The pressure and enthalpy values at various points across the cycle are presented in Table 5.4.

Table 5.4: Pressure and enthalpy data for a simple VCS with evaporation temperature of 0° Celsius and condensation temperature of 58° Celsius

Point	Description	Pressure [kPa]	Specific Enthalpy [kJ/kg]
1	Compressor suction	290	398.6
2	Compressor discharge	1600	447.7
2s	Condensation dew point	1600	426.1
3	Condenser outlet	1600	284.3
4	Expansion valve outlet	290	284.3

The pressure-enthalpy diagram of the simple VCS equipped with an isentropic compressor is presented in Figure 5.3. In case a non-isentropic compressor is considered, the corresponding p-h and t-s diagrams can be found in Appendix B.

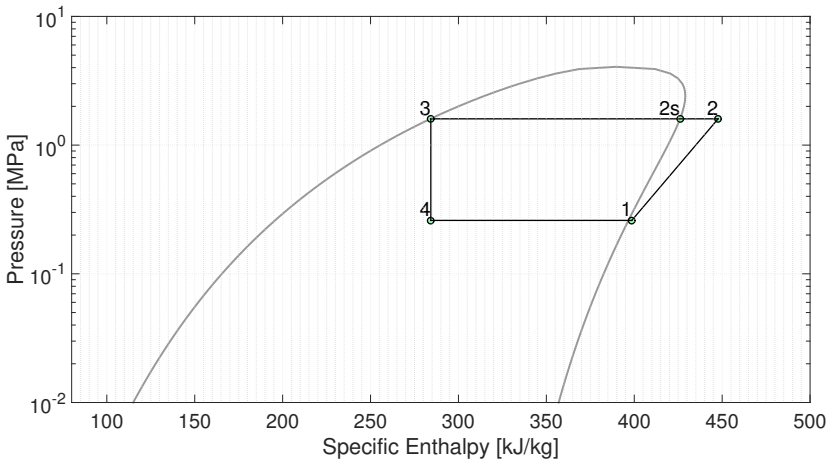

Figure 5.3: Pressure-enthalpy diagram for a simple VCS with evaporation temperature of 0° Celsius and condensation temperature of 58° Celsius (with isentropic compressor) h_2 = 447.7 kJ/kg

The cooling capacity of the system depends directly on the refrigerant mass flow rate and is summarised in Table 5.5 together with the performance data of the refrigerant compressor. The data presented applies to an ideal cycle having a cooling capacity that closely matches the thermal heat loads of the cabin. For redundancy the simulation model consists of two VCS packs each running at half of the cooling capacity, thus the refrigerant mass flow rate and compressor power consumption of each pack set at half of the values presented.

Table 5.5: Refrigerant compressor performance data for a simple VCS cycle for two operation modes: ground and cruise

Parameter	Unit	Ground	Cruise
Refrigerant mass flow rate	kg/s	0.41	0.36
Cooling capacity	kW	46.88	41.16
Condensing temperature	°Celsius	58	58
Evaporating temperature	°Celsius	0	0
Compression work, isentropic	kW	19.68	17.28
Isentropic efficiency	%	75	75
Compression work, effective	kW	26.24	23.04
Mechanical efficiency	%	90	90
Shaft power input	kW	29.16	25.60
Motor drive efficiency	%	90	90
Electrical power input	kW	32.40	28.44

The efficiency of the simple VCS cycle can be assessed using the coefficient of performance calculations. Considering the data presented in Table 5.6 and taking the pressurisation effect into account, the resulting COP for a simple VCS integrated at aircraft level equals 1.16 for ground operations and 0.28 for the cruise phase. Neglecting the pressurisation effect and integration at aircraft level, the coefficient of performance of the standalone simple VCS is also be computed under the name COP_{Local}, for which only the isentropic efficiency is considered. The resulting local COP has a value of 1.79 for both ground and cruise operations.

Table 5.6: Coefficient of performance calculations for technology demonstrator equipped with simple VCS

Parameter	Unit	Ground	Cruise
$\dot{Q}_{\text{c}}$	kW	46.88	41.16
$\dot{W}_{\text{ram}}$	kW	0.60	26.60
$\dot{W}_{\text{CAC}}$	kW	8.96	92.88
$\dot{W}_{\text{Refrigerant compressor}}$	kW	32.40	28.44
COP_{System}	-	1.16	0.28
COP_{Local}	-	1.78	1.78

VCS WITH SUPERHEATING

Based on the simple VCS presented above, a modified refrigeration cycle is obtained by adding a 10° Celsius superheat. The corresponding thermophysical data and pressure-enthalpy diagrams can be seen below in Table 5.7 and Figure 5.4 respectively. Any difference in a parameter such as an increase or decrease with respect to the simple VCS is represented in the table as a percentage difference.

Table 5.7: Pressure and enthalpy data for a superheated VCS with evaporation temperature of 0° Celsius, condensation temperature of 58° Celsius and a superheat value of 10° Celsius

Point	Description	Pressure [kPa]	Specific Enthalpy [kJ/kg]
1s	Evaporation dew point	290	398.6
1	Compressor suction	290	408.5
2	Compressor discharge	1600	457.9 (+2.2%)
2s	Condensation dew point	1600	426.1
3	Condenser outlet	1600	284.3
4	Expansion valve outlet	290	284.3

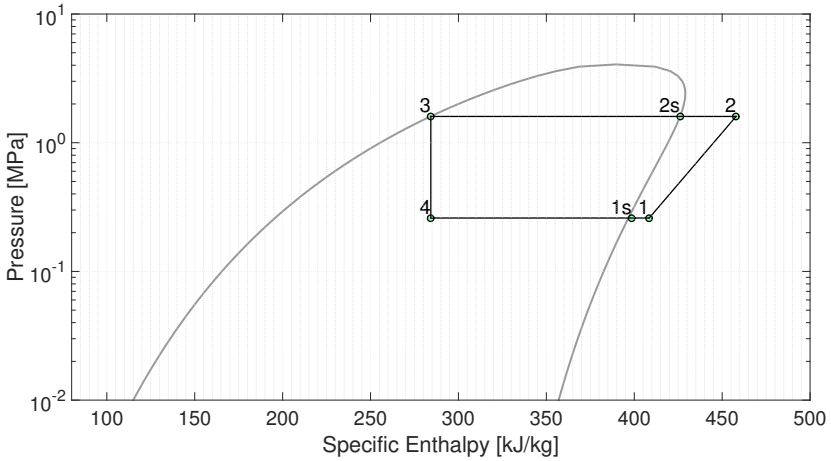

Figure 5.4: Pressure-enthalpy diagram for a superheated VCS with evaporation temperature of 0° Celsius, condensation temperature of 58° Celsius and a superheat value of 10° Celsius

Compared to a simple VCS, adding a 10 °Celsius superheat increases the cooling capacity of the system. The drawback is an increased work done by the compressor. Overall the effect of enhancing the cycle with a degree of superheat results in a slight improvement in the coefficient of performance because in absolute terms the increase in cooling capacity is much greater than the increase in compression work.

VCS WITH SUBCOOLING

In this section the effects of subcooling will be analysed and the results will be compared to those of a simple VCS previously presented. The corresponding pressure and enthalpy data belonging to a subcooled cycle with a degree of subcooling of 10 °Celsius is presented in Table 5.8. The corresponding pressure-enthalpy diagram is presented in Figure 5.5.

Table 5.8: Pressure and enthalpy data for a subcooled VCS with evaporation temperature of 0° Celsius, condensation temperature of 58° Celsius and a subcool value of 10° Celsius

Point	Description	Pressure [kPa]	Specific Enthalpy [kJ/kg]
1	Compressor suction	290	398.6
2	Compressor discharge	1600	447.7
2s	Condensation dew point	1600	426.1
3s	Condensation bubble point	1600	284.3
3	Condenser outlet including additional subcooling	1600	268.5
4	Expansion valve outlet	290	268.5

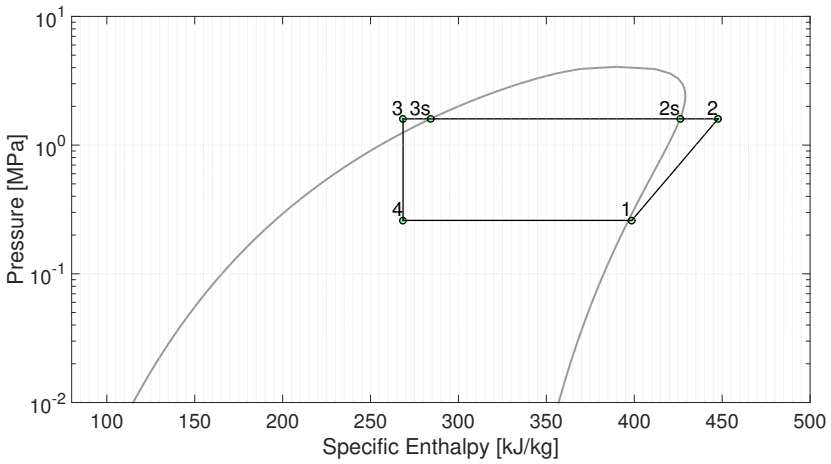

Figure 5.5: Pressure-enthalpy diagram for a subcooled VCS with evaporation temperature of 0° Celsius, condensation temperature of 58° Celsius and a subcool value of 10° Celsius

The main effect of subcooling as compared to a simple VCS cycle is an increased cooling capacity of the system, resulting in a higher coefficient of performance. This is possible since the work done by the compressor is not affected when adding a subcooler.

VCS WITH SUPERHEATING AND SUBCOOLING

At this point a simple vapour cycle system that meets the requirements has been designed and both the effects of superheating and subcooling were investigated separately. It is now possible to design an advanced VCS cycle by adding a 10° Celsius superheat and a 10° Celsius subcooling degree simultaneously while monitoring the effect on the coefficient of performance. The changes with respect to the simple VCS are also indicated by means of percentage differences in the following data tables, starting with Table 5.9 showing the updated thermodynamic cycle data of the advanced cycle.

Table 5.9: Pressure-enthalpy diagram for a superheated and subcooled VCS with evaporation temperature of 0° Celsius, condensation temperature of 58° Celsius, a superheat value of 10° Celsius and a subcool value of 10° Celsius

Point	Description	Pressure [kPa]	Specific Enthalpy[kJ/kg]
1s	Evaporation dew point	290	398.6
1	Compressor suction	290	408.5
2	Compressor discharge	1600	457.9 (+2.2%)
2s	Condensation dew point	1600	426.1
3s	Condensation bubble point	1600	284.3
3	Condenser outlet including additional subcooling	1600	268.5
4	Expansion valve outlet	290	268.5

Corresponding the pressure-enthalpy diagram shown in Figure 5.6, as a degree of 10° Celsius superheat is added to the cycle, the effect is an increased evaporator capacity. Since the cooling capacity can be kept fixed around the total heat load to be cooled down, the benefit of adding a degree of superheat is the possibility of reducing the mass flow rate of the refrigerant with the aim of minimising the work done by the refrigerant compressor. The same principle applies to the degree of subcooling which would again increase the cooling capacity of the cycle, however it is preferred to further reduce the refrigerant mass flow rate instead. The results are summarised in Table 5.10 showing reduced refrigerant mass flow rates, ultimately leading to reduced electrical power input values to be provided to the refrigerant compressor.

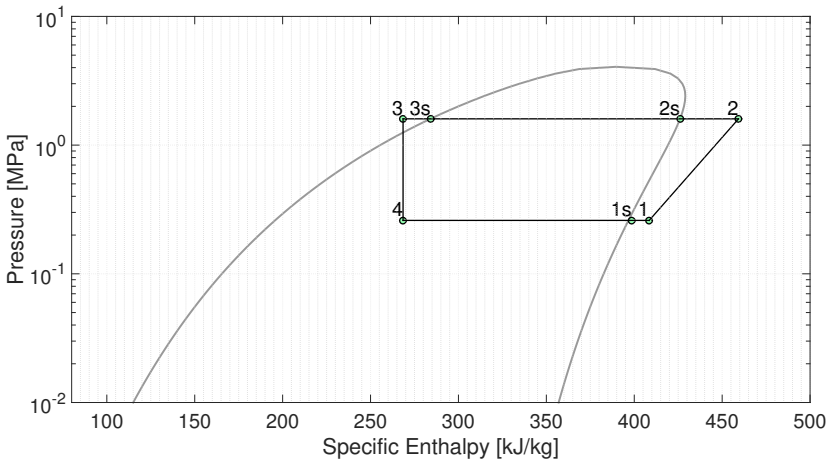

Figure 5.6: Pressure-enthalpy diagram for a superheated and subcooled VCS with evaporation temperature of 0° Celsius, condensation temperature of 58° Celsius, a superheat value of 10° Celsius and a subcool value of 10° Celsius (with isentropic compressor)

Table 5.10: Refrigerant compressor performance data for an advanced VCS cycle with evaporation temperature of 0° Celsius, condensation temperature of 58° Celsius, a superheat value of 10° Celsius and a subcool value of 10° Celsius. Data for two operation modes: ground and cruise

Parameter	Unit	Ground	Cruise
Refrigerant mass flow rate	kg/s	0.34 (-18.4%)	0.30 (-18.2%)
Cooling capacity	kW	47.20	41.65
Condensing temperature	°Celsius	58	58
Evaporating temperature	°Celsius	0	0
Compression work, isentropic	kW	17.27	15.24
Isentropic efficiency	%	75	75
Compression work, effective	kW	23.03	20.32
Mechanical efficiency	%	90	90
Shaft power input	kW	25.59	22.85
Motor drive efficiency	%	90	90
Electrical power input	kW	28.43 (-13%)	25.09 (-12.5%)

The resulting performance related data of the improved cycle is summarised in Table 5.11 showing increased coefficient of performance values for both ground and cruise conditions. This is made possible due to the reduction in required refrigerant mass flow rate, resulting in decreased refrigerant compressor power demand.

Table 5.11: Coefficient of performance calculations for technology demonstrator equipped with an advanced VCS with evaporation temperature of 0° Celsius, condensation temperature of 58° Celsius, a superheat value of 10° Celsius and a subcool value of 10° Celsius. Data for two operation modes: ground and cruise

Parameter	Unit	Ground	Cruise
$\dot{Q}_c$	kW	47.20	41.65
$\dot{W}_{ram}$	kW	0.60	26.60
$\dot{W}_{CAC}$	kW	8.96	92.88
$\dot{W}_{Refrigerant\ compressor}$	kW	28.43 (-13%)	25.09 (-12.5%)
COP_{System}	-	1.24 (+6.7%)	0.29 (+3.5%)
COP_{Local}	-	2.05 (+14%)	2.05 (+14%)

5.3. ELECTRIC LOAD ANALYSIS

Based on the proposed methodology regarding the electric loads analysis presented in Section 3.4, a power budget is created for both the baseline model and the technology demonstrator, followed by a comparison between the two. To make a fair comparison between the two models, the values for the essential loads and

the galley loads shall be the same for both models. The *essential load* considered is the cockpit avionics electrical load, assumed to have a nominal power demand of 10 kW constant throughout all the flight phases. The *galley loads* considered consist of the forward galley load and the aft galley load, each with a nominal power demand of 40 kW. This value can be adjusted by altering the OperatingRatio parameter in the assumptions list prior to triggering the performance envelope. An operating ratio of 50% corresponding to 40 kW is assumed during pre-flight, taxi, descent and landing. For cruise conditions an operating ratio of 100 % is assumed, corresponding to a total maximum power demand of 80 kW. For the take-off and climb an operating ratio of 75 % is assumed, resulting in a power demand of 60 kW.

5.3.1. BASELINE MODEL

As discussed in the methodology section, it is possible to control the power demand of the cabin air compressors as a function of the mix manifold recirculation ratio and the exit pressure of the cabin air compressor. For a cabin air compressor exit pressure during both flight and cruise conditions of 2.75 bar in combination with a recirculation ratio of 50%, the utility loads can be quantified. Comparing ground to cruise operations, lower utility loads are recorded in the former case due to a lower operating pressure ratio of the cabin air compressor. For ground operations the pressure of the air at the inlet of the cabin air compressor has a pressure of 1 bar as compared to approximately 0.35 bar as in the case of cruise at 35000 ft. To simplify the diagram the utility loads during the remaining flight cases such as take-off, cruise, descent and landing are set equal to those required during the critical condition identified as the cruise segment.

5.3.2. TECHNOLOGY DEMONSTRATOR

The power budget corresponding to the electrical load analysis of the technology demonstrator slightly differs from that of the baseline model due to different utility loads. As opposed to the air cycle machine, in case of the vapour cycle system the cabin air compressor has to meet only the pressurisation requirement, thus its exit pressure is set to a value just above the required cabin altitude. Thus for the ground condition the exit pressure of the cabin air compressor is set to 1.1 bar, while for the cruise segment the chosen exit pressure is set equal to 0.9 bar, just above the cabin altitude requirement of 6000 ft. For the remaining flight segments the operating condition of the cabin air compressor is set equal to the condition selected for the cruise segment, allowing to simplify the electrical load analysis diagram and focusing on the chosen critical design points, namely the ground and cruise flight segments.

5.3.3. COMPARISON

Having obtained the electrical load analysis for the two configurations a comparison of secondary power off-takes and electrical power demand can be performed. To make sure the newly designed refrigeration system copes with all flight conditions, the flight phase corresponding to the highest power demand shall be used in rating the total installed electrical power generation required. Table 5.12 shows a summary of the critical secondary power off-take values considered when comparing the baseline model with the vapour cycle system. The two off-takes considered are the pneumatic bleed air (Out Pneumatic) and mechanical shaft power (Out Rotational). In case of the pneumatic off-take, this is set equal to zero in both cases. As mentioned above, the cruise phase was identified as the critical design condition, in which case the shaft power extraction is equal to 553 shp in case of the baseline model, while for the technology demonstrator it is equal to 316 shp. The results are presented graphically in Figure 5.7.

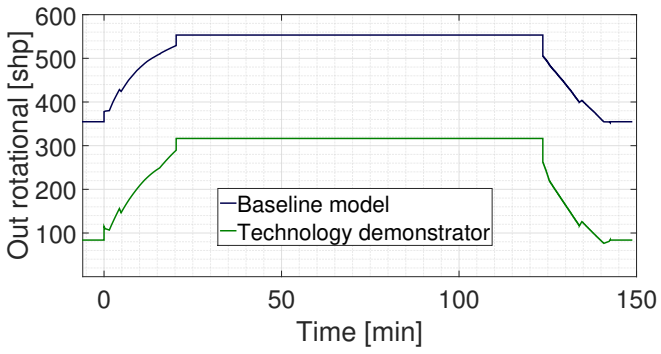

Figure 5.7: Secondary shaft power extraction variation with mission timeline

Table 5.12: Secondary power off-takes and electrical power demand during cruise flight segment

Secondary power off-takes and system's electrical power demand	Baseline model	Technology demonstrator
Out Pneumatic [kg/s]	0	0
Out Rotational [shp]	553	316

5.4. TRIP FUEL COMPARISON

A trip fuel comparison study between the baseline model and technology demonstrator has been carried out for different scenarios. Starting from a first set of results, the effect of assumptions on results has been investigated, followed by the effect of a possible weight penalty.

5.4.1. FIRST SET OF RESULTS

Taking into account the critical power demand of both architectures, a comparison of trip fuel consumption can be performed between the baseline model and the technology demonstrator where variations in trip fuel are recorded for different flight missions ranging from 500 nm to 2000 nm, also covering the selected baseline mission of 1000 nm. The resulting fuel savings vary from 1.52 % for a 500 nm flight mission up to 1.70 % for a 2000 nm flight mission.

Table 5.13: Trip fuel comparison results with baseline model air cycle system running at $P_{cac,exit}$=2.75 bar

Parameter	Unit	Value			
Distance	nm	500	1000	1500	2000
Trip fuel baseline model	kg	3575	6586	9693	12916
Trip fuel technology demonstrator	kg	3521	6480	9533	12698
Delta trip fuel	kg	54	106	160	218
Fuel savings	%	1.52	1.62	1.66	1.70

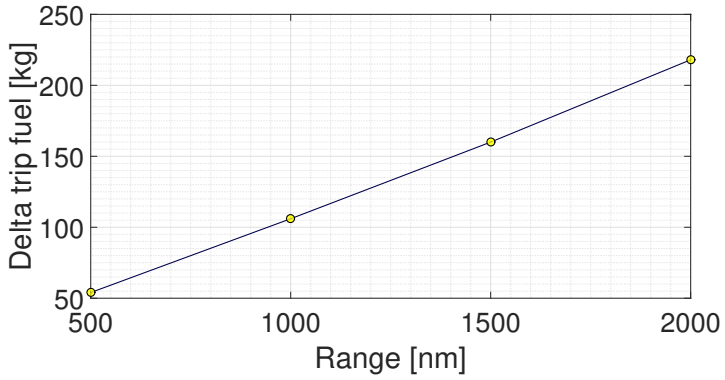

Figure 5.8: Delta trip fuel comparison, initial set of results

5.4.2. EFFECT OF ASSUMPTIONS ON RESULTS

The effect of assumptions on results is investigated by running additional simulations. Based on the sensitivity study the parameters could be classified as either negligible or having a large impact on results. An example of a parameter having high linear effects on results is the cabin air compressor exit pressure, which was set at a default value of 2.75 bar in case of the baseline model. It was noticed that the air cycle machine can also operate at other pressure levels, ranging from 1.73 bar to 4 bar. Since it was already highlighted that for a pressure level of 2.75 bar air cycle system integrated at aircraft level is less efficient in terms of fuel consumption than the vapour cycle system, an additional computation of trip fuel this time setting the pressure at the exit of the cabin air compressor at the minimum value of 1.73 bar is investigated with results shown in Table 5.14. The results show a decrease in trip fuel for the baseline model throughout the four simulated missions ranging from 500 nm to 2000 nm. For a common design mission of 1000 nm, the delta trip fuel

between the baseline model and technology demonstrator was decreased from 109 kg to 57 kg, resulting in a fuel savings of 0.92 % in case of the vapour cycle system equipped technology demonstrator.

Table 5.14: Trip fuel comparison results with baseline model air cycle system running at $P_{cac,exit}$=1.73 bar

Parameter	Unit	Value			
Distance	nm	500	1000	1500	2000
Trip fuel baseline model	kg	3550(-0.70%)	6537(-0.76%)	9620(-0.76%)	12816(-0.78%)
Trip fuel technology demonstrator	kg	3521	6480	9533	12698
Delta trip fuel	kg	29	57	87	118
Fuel savings	%	0.82	0.87	0.91	0.93

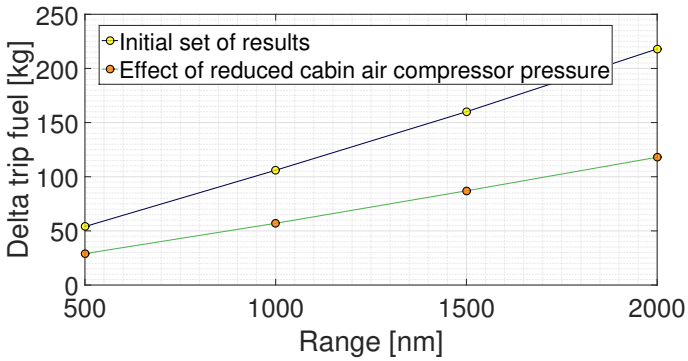

Figure 5.9: Delta trip fuel comparison accounting for the effect of a reduced cabin air compressor exit pressure in case of the baseline model

5.4.3. EFFECT OF WEIGHT PENALTY

Up to this point the assumption of no difference in mass between the two systems has been applied. It is interesting to investigate what would be the effect of a weight penalty on the difference in fuel trip comparison. For this study a most pessimistic weight penalty of 150 kg was considered. This value has been chosen according to data found in literature regarding the two options of environmental control systems applied to the Lockheed Constellation. For this aircraft an air cycle system with a mass of 114 kg was available, with an alternative of a vapour cycle system with a mass of 265 kg [76]. This approximate 150 kg difference in mass between the two systems can be associated with the technology of years 1946-1958 when vapour cycle systems were still using heavy reciprocating compressors.

Table 5.15: Trip fuel comparison results with baseline model air cycle system running at $P_{cac,exit}$=2.75 bar

Parameter	Unit	Value			
Distance	nm	500	1000	1500	2000
Trip fuel baseline model	kg	3575	6586	9693	12916
Trip fuel technology demonstrator	kg	3526(+0.14%)	6489(+0.14%)	9548(+0.16%)	12718(+0.16%)
Delta trip fuel	kg	49	97	145	198
Fuel savings	%	1.38	1.48	1.51	1.54

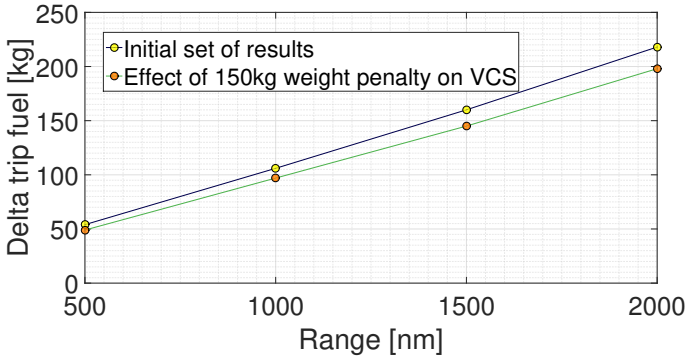

Figure 5.10: Delta trip fuel comparison accounting for the effect of weight penalty of 150kg applied to the VCS model

6

CONCLUSIONS

A design and assessment study for a novel environmental control system using the vapour compression refrigeration cycle was carried out with the aim of quantifying its impact on aircraft performance and compare it with that of an electric driven air cycle machine based system. The three main design driving functions to be met by both systems were defined part of the requirements engineering process as temperature control to be maintained between 18° and 23 °Celsius, a maximum cabin pressure altitude of 6000 ft and ventilation control with a minimum fresh air mass flow rate of 10 ft^3/min.

Using a heat transfer model the cabin was discretised in three compartments for which the total heat load was computed by taking into account the effects heat transfer mechanisms such as conduction, convection and solar radiation. For ground operations a heat load of 46.3 kW was obtained, while for the cruise flight segment a heat load of 40.4 kW was obtained, representing the cooling load required to size the refrigeration units.

The conventional environmental control system unit to be installed onboard the baseline model consists of a dual heat exchanger air cycle machine assembly in combination with an electrically driven cabin air compressor. The two heat exchangers were chosen accordingly to the most used type employed in air to air heat exchangers, namely compact heat exchangers with plate fin geometry, off-set strip fins and counter-flow arrangement. For the air cycle machine a compressor isentropic efficiency of 75% was considered, while for the cooling turbine isentropic efficiency a value of 80% was set.

The novel system to be installed onboard the technology demonstrator consists of an advanced vapour compression refrigeration cycle taking into account both the effects of superheating and subcooling. The evaporator assembly was discretised in two zones in order to account for the sensible heat transfer as well as for the the latent heat transfer occurring prior to compression. The condenser assembly was discretised in three zones allowing to model the sensible heat transfer occurring as the refrigerant exits the compression phase, the latent heat transfer occurring inside the two phase region of the refrigerant saturation curve and the sensible heat transfer associated with subcooling.

The architecture of both systems was verified part of a sensitivity study using the MOAT method which has highlighted the parameters having a significant impact on the trip fuel for a baseline mission of 1000 nm and 12000 kg payload. In case of the technology demonstrator it was shown that the refrigerant mass flow rate has a large linear impact on the resulting trip fuel as this variable was directly affecting the power demand of the refrigerant compressor. Using R134a refrigerant the cooling capacity of the vapour cycle system was met by a refrigerant mass of 0.34 kg/s during ground and 0.30 kg/s during cruise operations.

Sensitivity of the system to secondary power off-takes was verified by varying the out rotational power extraction from each engine and noticing the change in specific fuel consumption. Increasing power off-takes from 0 to 300 shp resulted in an increased specific fuel consumption from 16.7 to 17.1 g/(kN.s). Comparing the engine data with an alternative performance deck model allowed to also verify the slope of the line between specific fuel consumption correction factor and out rotational off-takes, showing a similar increasing trend between the two.

The obtained results can be directly linked to the proposed research question *"What is the impact on the trip fuel when replacing a conventional electrically driven air management system with an electrically driven vapour cycle refrigeration system?"*. The impact of the two environmental control systems architectures on trip fuel was determined by first quantifying the power demand of the systems. Taking into account both

pressurisation and refrigeration effects the efficiency of the systems were assessed and compared based on coefficient of performance calculations. The calculated coefficient of performance during cruise was equal to 0.29 for the vapour cycle system and 0.12 for the electrically driven air cycle machine, highlighting the newly designed system as the more efficient of the two. This effect was confirmed again at aircraft level as the installation of the vapour cycle system resulted in a fuel saving of up to 106 kg (-1.62%) for a baseline mission of 1000 nm and 12000 kg payload. The initial set of results is based on the assumption that both system architectures have the same weight. In case of a most pessimistic weight penalty of 150 kg added to the VCS architecture, the fuel saving reduces to 97 kg (-1.48%), still indicating that the novel vapour cycle system is more efficient. Taking into account the effect of assumptions on results, different cabin air compressor exit pressure values were considered for the air cycle machine architecture as this parameter was identified as having large linear effects on results. It was determined that the air cycle machine can function at different inlet pressure levels ranging from 1.73 bar to 4 bar. Even when operating at the lowest inlet pressure of 1.73 bar it was shown that the air cycle machine is still less efficient than the vapour cycle system, with a delta trip fuel of 57 kg (-0.87%) in favour of the vapour cycle refrigeration unit.

7

RECOMMENDATIONS

The current research provides insights into the development and integration at aircraft level of a vapour compression refrigeration unit which remains an open challenge. The major obstacle identified during the configuration process was the transition from the requirements to the technology implementation. Designing a system with a duty capacity in the range of 40-45 kW using a centrifugal compressor offers the freedom to consider numerous system architectures starting from simple single-stage cycles up to advanced cycles including subcooling, expansion loss recovery and multi-stage configurations.

The results obtained from the thermodynamic analysis of the vapour cycle system indicate that a system meeting the refrigeration requirements must have a design mass flow rate ranging from 0.36 kg/s to 0.41 kg/s depending on whether the system operates while the aircraft is on ground or during cruise phase. The pressure ratio for the resulting system is equal to 5.5, taking the low pressure level at 2.9 bar and the high pressure level at 16 bar. The presented data translates into a mass flow rate requirement and a pressure ratio requirement.

7.1. MASS FLOW RATE REQUIREMENT

Based on the literature review on miniature compressors summarised in Appendix A, the mass flow rates of such compressors attain values in the range of 1-30 g/s. Thus it is clear that a system using only one centrifugal miniature compressor would not meet the mass flow rate requirement. In order to increase the overall mass flow rate of the system, two or more compressors can be placed in parallel. This configuration will allow to increase the overall mass flow rate while keeping the pressure ratio of the system equal to that of a single compressor set-up.

7.2. PRESSURE RATIO REQUIREMENT

Based on the literature review on miniature compressors summarised in Appendix C typical pressure ratios for a single stage centrifugal compressors operating at speeds from 50,000 to 500,000 rom ranges between 1 and 2, much below the pressure ratio requirement of 5.5. In order to increase the pressure ratio, two or more compressors can be placed in series. The resulting mass flow rate will be the same but the resulting pressure ratio will be higher than in the case of a single compressor configuration and can be computed by multiplying the pressure ratios of each compressor stage, as shown by Equation 7.1

$$\beta = \beta_1 \cdot \beta_2 ... \beta_n \tag{7.1}$$

7.3. PROPOSED SYSTEM TO BE INVESTIGATED

For detailed weight calculations a vapour cycle system using miniature centrifugal compressors must be designed taking into account both the mass flow rate and pressurisation requirement. The resulting system shown in Figure 7.1 shows a multi stage compressor configuration with n compressors placed in parallel (to meet the mass flow rate requirement) and m compressors placed in series (to meet the pressure ratio requirement). Placing more compressors in series results in additional heat produced after each compression stage. To minimise this the integration of an additional heat exchanger named a flash inter-cooler may be required, increasing further the overall system mass [67, pp. 122-141].

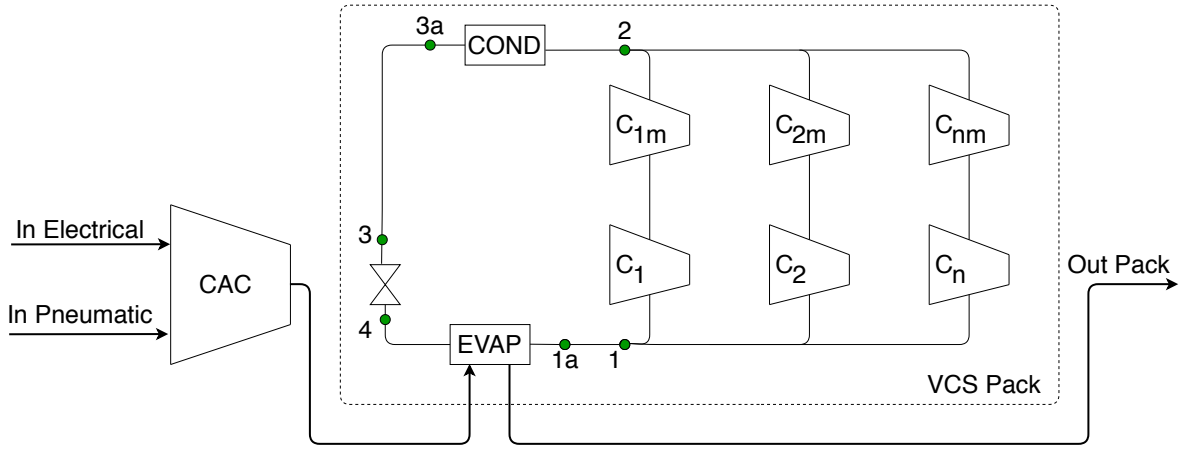

Figure 7.1: VCS schematic proposal with a number of n miniature centrifugal compressors placed in parall and a number of m placed in series

Different types of compressor configurations integrated in multistage cycles were already investigated in various studies. A summary of data has been gathered in Appendix C including rotary and centrifugal compressors. Compared to 1998 technology when a dual stage vapour compression system using a centrifugal compressor could reach a pressure ratio of 4 for a compressor speed of 47,000 rpm [77] a shift towards higher compressor rotational speeds of up to 500,000 rpm has been noticed from research performed between 2009 and 2013 [78] [21].

A

REFERENCE DATA REFRIGERANT R134A

The reference state for refrigerant R134a thermophysical properties corresponds to SI units as given by ASHRAE 2017 Fundamentals (SI Edition) [16, pp. 811-812], being set to 0 ° Celsius for a saturated liquid enthalpy of h_f = 200 kJ/kg and an associated entropy of s_f = 1 kJ/(kg.K). It was noticed in other references such as Yunes et al. [79, p. 966] that the reference state was linked to the imperial units, in which the saturated liquid enthalpy and entropy values were set to zero at -40 ° Celsius.

Figure A.1 contains the thermopyhsical properties of the R134a refrigerant in the temperature range from -100 ° to 2 ° Celsius, while Figure A.2 contains the remaining properties in the range from 4 ° to 100 ° Celsius. Figure A.3 contains the pressure-enthalpy diagram including the saturation curve of the refrigerant.

Temp.,* °C	Pressure, MPa	Density, kg/m³ Liquid	Volume, m³/kg Vapor	Enthalpy, kJ/kg Liquid	Enthalpy, kJ/kg Vapor	Entropy, kJ/(kg·K) Liquid	Entropy, kJ/(kg·K) Vapor	Specific Heat c_p, kJ/(kg·K) Liquid	Specific Heat c_p, kJ/(kg·K) Vapor
–103.30[a]	0.00039	1591.1	35.4960	71.46	334.94	0.4126	1.9639	1.184	0.585
–100	0.00056	1582.4	25.1930	75.36	336.85	0.4354	1.9456	1.184	0.593
–90	0.00152	1555.8	9.7698	87.23	342.76	0.5020	1.8972	1.189	0.617
–80	0.00367	1529.0	4.2682	99.16	348.83	0.5654	1.8580	1.198	0.642
–70	0.00798	1501.9	2.0590	111.20	355.02	0.6262	1.8264	1.210	0.667
–60	0.01591	1474.3	1.0790	123.36	361.31	0.6846	1.8010	1.223	0.692
–50	0.02945	1446.3	0.60620	135.67	367.65	0.7410	1.7806	1.238	0.720
–40	0.05121	1417.7	0.36108	148.14	374.00	0.7956	1.7643	1.255	0.749
–30	0.08438	1388.4	0.22594	160.79	380.32	0.8486	1.7515	1.273	0.781
–28	0.09270	1382.4	0.20680	163.34	381.57	0.8591	1.7492	1.277	0.788
–26.07[b]	0.10133	1376.7	0.19018	165.81	382.78	0.8690	1.7472	1.281	0.794
–26	0.10167	1376.5	0.18958	165.90	382.82	0.8694	1.7471	1.281	0.794
–24	0.11130	1370.4	0.17407	168.47	384.07	0.8798	1.7451	1.285	0.801
–22	0.12165	1364.4	0.16006	171.05	385.32	0.8900	1.7432	1.289	0.809
–20	0.13273	1358.3	0.14739	173.64	386.55	0.9002	1.7413	1.293	0.816
–18	0.14460	1352.1	0.13592	176.23	387.79	0.9104	1.7396	1.297	0.823
–16	0.15728	1345.9	0.12551	178.83	389.02	0.9205	1.7379	1.302	0.831
–14	0.17082	1339.7	0.11605	181.44	390.24	0.9306	1.7363	1.306	0.838
–12	0.18524	1333.4	0.10744	184.07	391.46	0.9407	1.7348	1.311	0.846
–10	0.20060	1327.1	0.09959	186.70	392.66	0.9506	1.7334	1.316	0.854
–8	0.21693	1320.8	0.09242	189.34	393.87	0.9606	1.7320	1.320	0.863
–6	0.23428	1314.3	0.08587	191.99	395.06	0.9705	1.7307	1.325	0.871
–4	0.25268	1307.9	0.07987	194.65	396.25	0.9804	1.7294	1.330	0.880
–2	0.27217	1301.4	0.07436	197.32	397.43	0.9902	1.7282	1.336	0.888
0	0.29280	1294.8	0.06931	200.00	398.60	1.0000	1.7271	1.341	0.897
2	0.31462	1288.1	0.06466	202.69	399.77	1.0098	1.7260	1.347	0.906

Figure A.1: R134a refrigerant properties from -100 ° to 2 ° Celsius , adapted from ASHRAE 2017 Fundamentals (SI Edition) [16, p. 812]

Temp.,* °C	Pressure, MPa	Density, kg/m³ Liquid	Volume, m³/kg Vapor	Enthalpy, kJ/kg Liquid	Enthalpy, kJ/kg Vapor	Entropy, kJ/(kg·K) Liquid	Entropy, kJ/(kg·K) Vapor	Specific Heat c_p, kJ/(kg·K) Liquid	Specific Heat c_p, kJ/(kg·K) Vapor
4	0.33766	1281.4	0.06039	205.40	400.92	1.0195	1.7250	1.352	0.916
6	0.36198	1274.7	0.05644	208.11	402.06	1.0292	1.7240	1.358	0.925
8	0.38761	1267.9	0.05280	210.84	403.20	1.0388	1.7230	1.364	0.935
10	0.41461	1261.0	0.04944	213.58	404.32	1.0485	1.7221	1.370	0.945
12	0.44301	1254.0	0.04633	216.33	405.43	1.0581	1.7212	1.377	0.956
14	0.47288	1246.9	0.04345	219.09	406.53	1.0677	1.7204	1.383	0.967
16	0.50425	1239.8	0.04078	221.87	407.61	1.0772	1.7196	1.390	0.978
18	0.53718	1232.6	0.03830	224.66	408.69	1.0867	1.7188	1.397	0.989
20	0.57171	1225.3	0.03600	227.47	409.75	1.0962	1.7180	1.405	1.001
22	0.60789	1218.0	0.03385	230.29	410.79	1.1057	1.7173	1.413	1.013
24	0.64578	1210.5	0.03186	233.12	411.82	1.1152	1.7166	1.421	1.025
26	0.68543	1202.9	0.03000	235.97	412.84	1.1246	1.7159	1.429	1.038
28	0.72688	1195.2	0.02826	238.84	413.84	1.1341	1.7152	1.437	1.052
30	0.77020	1187.5	0.02664	241.72	414.82	1.1435	1.7145	1.446	1.065
32	0.81543	1179.6	0.02513	244.62	415.78	1.1529	1.7138	1.456	1.080
34	0.86263	1171.6	0.02371	247.54	416.72	1.1623	1.7131	1.466	1.095
36	0.91185	1163.4	0.02238	250.48	417.65	1.1717	1.7124	1.476	1.111
38	0.96315	1155.1	0.02113	253.43	418.55	1.1811	1.7118	1.487	1.127
40	1.0166	1146.7	0.01997	256.41	419.43	1.1905	1.7111	1.498	1.145
42	1.0722	1138.2	0.01887	259.41	420.28	1.1999	1.7103	1.510	1.163
44	1.1301	1129.5	0.01784	262.43	421.11	1.2092	1.7096	1.523	1.182
46	1.1903	1120.6	0.01687	265.47	421.92	1.2186	1.7089	1.537	1.202
48	1.2529	1111.5	0.01595	268.53	422.69	1.2280	1.7081	1.551	1.223
50	1.3179	1102.3	0.01509	271.62	423.44	1.2375	1.7072	1.566	1.246
52	1.3854	1092.9	0.01428	274.74	424.15	1.2469	1.7064	1.582	1.270
54	1.4555	1083.2	0.01351	277.89	424.83	1.2563	1.7055	1.600	1.296
56	1.5282	1073.4	0.01278	281.06	425.47	1.2658	1.7045	1.618	1.324
58	1.6036	1063.2	0.01209	284.27	426.07	1.2753	1.7035	1.638	1.354
60	1.6818	1052.9	0.01144	287.50	426.63	1.2848	1.7024	1.660	1.387
62	1.7628	1042.2	0.01083	290.78	427.14	1.2944	1.7013	1.684	1.422
64	1.8467	1031.2	0.01024	294.09	427.61	1.3040	1.7000	1.710	1.461
66	1.9337	1020.0	0.00969	297.44	428.02	1.3137	1.6987	1.738	1.504
68	2.0237	1008.3	0.00916	300.84	428.36	1.3234	1.6972	1.769	1.552
70	2.1168	996.2	0.00865	304.28	428.65	1.3332	1.6956	1.804	1.605
72	2.2132	983.8	0.00817	307.78	428.86	1.3430	1.6939	1.843	1.665
74	2.3130	970.8	0.00771	311.33	429.00	1.3530	1.6920	1.887	1.734
76	2.4161	957.3	0.00727	314.94	429.04	1.3631	1.6899	1.938	1.812
78	2.5228	943.1	0.00685	318.63	428.98	1.3733	1.6876	1.996	1.904
80	2.6332	928.2	0.00645	322.39	428.81	1.3836	1.6850	2.065	2.012
85	2.9258	887.2	0.00550	332.22	427.76	1.4104	1.6771	2.306	2.397
90	3.2442	837.8	0.00461	342.93	425.42	1.4390	1.6662	2.756	3.121
95	3.5912	772.7	0.00374	355.25	420.67	1.4715	1.6492	3.938	5.020
100	3.9724	651.2	0.00268	373.30	407.68	1.5188	1.6109	17.59	25.35

Figure A.2: R134a refrigerant properties from 4 ° to 100 ° Celsius, adapted from ASHRAE 2017 Fundamentals (SI Edition) [16, p. 812]

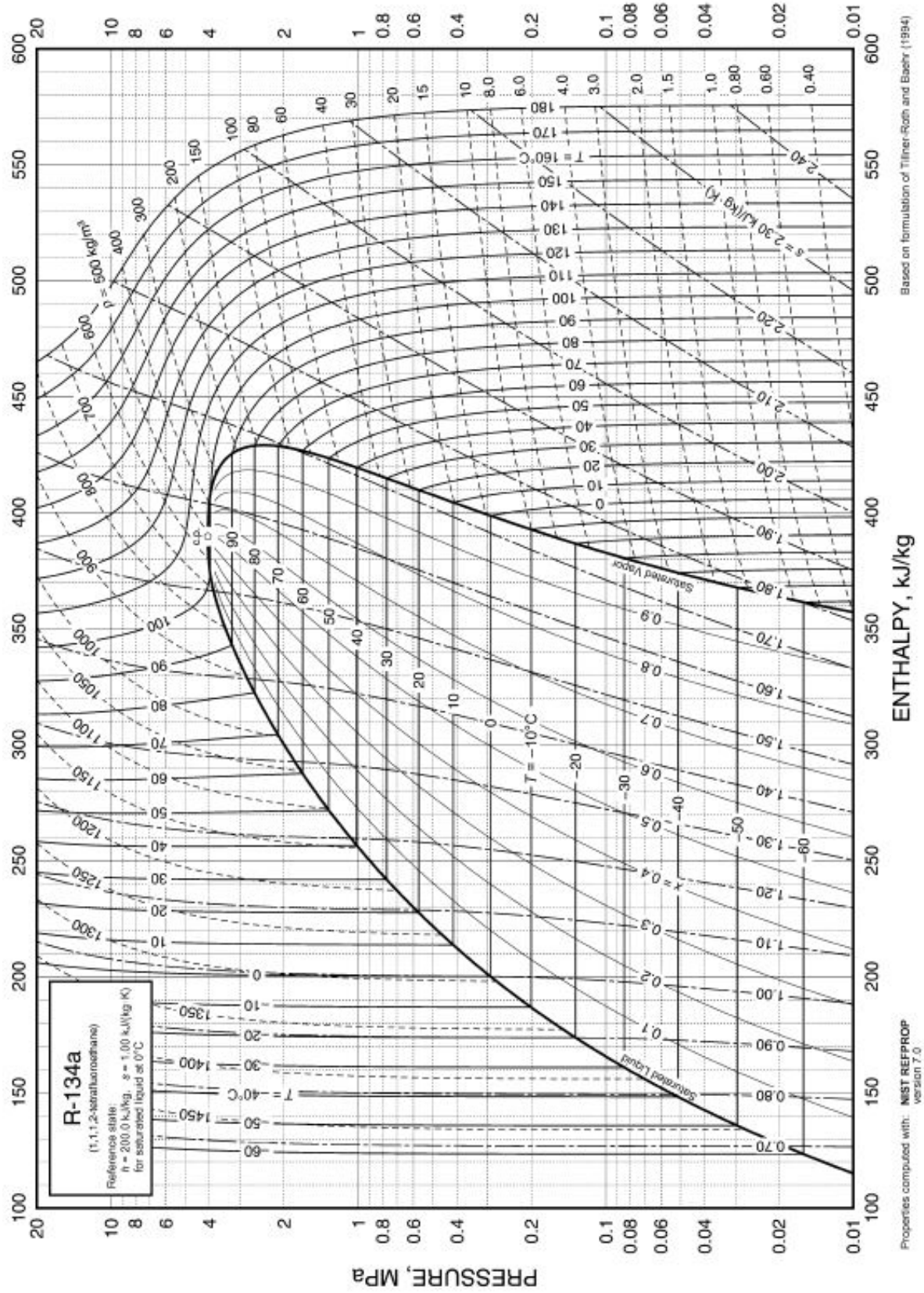

Figure A.3: R134a Pressure-Enthalpy diagram, copied from ASHRAE 2017 Fundamentals (SI Edition) [16, p. 811]

The constant pressure tables (superheated refrigerant tables) are used for two main reasons. Firstly the specific heat capacities required in calculating the sensible heat transfer in the condenser and evaporator are extracted. For the compressor suction a pressure a value of 290 kPa is used (shown in Figure A.4), the same table being implemented in Sysarc under the name of *Pace.Sysarc.SysArcDataStructure.R134aCp_290kPa*. Secondly the enthalpy at the suction and discharge points can be extracted at a fixed pressure as a function of temperature, allowing to calculate the work done by the compressor. For the suction pressure of 290 kPa, the enthalpy values are copied from the table shown in Figure A.4 and implemented in the Sysarc Knowledge Designer database under the name of *Pace.Sysarc.SysArcDataStructure.R134a_h_290kPa*. At this point the MDT's are part of the project however in order to use the stored data additional parameters have to be defined under SysarcDataStructure.AircraftSystems.Parameters to which the MDT data will be assigned. These parameters of type multidimensional data tables are named *R134a_h_290kPa* and *R134a_Cp_290kPa*.

PRESSURE = 290.00 kPa (abs)						TEMP
V	H	S	Cp	Cp/Cv	v_s	°C
0.00077	199.6	0.9986	1.3403	1.5214	626.4	–0.28
0.06995	398.6	1.7280	0.8871	1.1774	147.0	–0.28
0.07005	398.9	1.7289	0.8870	1.1770	147.1	0
0.07183	403.3	1.7449	0.8864	1.1690	149.1	5
0.07359	407.8	1.7607	0.8869	1.1620	151.0	10
0.07531	412.2	1.7763	0.8885	1.1558	152.8	15
0.07701	416.6	1.7916	0.8909	1.1503	154.6	20
0.07867	421.1	1.8067	0.8939	1.1454	156.4	25
0.08033	425.6	1.8216	0.8976	1.1409	158.1	30
0.08196	430.1	1.8363	0.9018	1.1369	159.7	35
0.08358	434.6	1.8508	0.9064	1.1332	161.3	40
0.08517	439.1	1.8652	0.9113	1.1298	162.9	45
0.08676	443.7	1.8795	0.9166	1.1267	164.4	50
0.08835	448.3	1.8936	0.9221	1.1239	166.0	55
0.08990	452.9	1.9076	0.9279	1.1212	167.4	60
0.09145	457.6	1.9215	0.9338	1.1187	168.9	65
0.09301	462.3	1.9352	0.9399	1.1164	170.3	70
0.09455	467.0	1.9489	0.9462	1.1143	171.8	75
0.09606	471.7	1.9624	0.9525	1.1123	173.1	80
0.09760	476.5	1.9758	0.9590	1.1104	174.5	85
0.09911	481.3	1.9892	0.9656	1.1086	175.9	90
0.10062	486.2	2.0024	0.9722	1.1069	177.2	95
0.10213	491.0	2.0156	0.9788	1.1053	178.5	100
0.10363	496.0	2.0286	0.9855	1.1038	179.8	105
0.10512	500.9	2.0416	0.9923	1.1024	181.1	110
0.10663	505.9	2.0546	0.9990	1.1010	182.4	115
0.10812	510.9	2.0674	1.0058	1.0997	183.7	120
0.10960	515.9	2.0801	1.0126	1.0985	184.9	125
0.11107	521.0	2.0928	1.0194	1.0973	186.1	130
0.11256	526.1	2.1054	1.0262	1.0961	187.4	135
0.11404	531.3	2.1180	1.0329	1.0950	188.6	140
0.11550	536.5	2.1304	1.0397	1.0940	189.8	145
0.11697	541.7	2.1428	1.0464	1.0930	191.0	150

Figure A.4: R134a refrigerant properties: constant pressure table (superheated refrigerant table) at 290 kPa (2.9 bar)

For the compressor discharge a pressure estimation of 1600 kPa is used corresponding to a chosen condensation temperature of 58 ° Celsius (shown in Figure A.5). The constant pressure table is implemented in Sysarc as an MDT under the name of *Pace.Sysarc.SysArcDataStructure.R134aCp_1600kPa* which is called by the parameter *R134a_cp_1600kPa* used in the calculation of the actual cp value as a function of temperature. In an analogue way the enthalpy values are extracted and stored in Sysarc as an MDT under the name of *Pace.Sysarc.SysArcDataStructure.R134a_h_1600kPa*. The corresponding parameters used to access the MDT data at a constant pressure of 1600 kPa are defined under the names of *R134a_h_1600kPa* and *R134a_Cp_1600kPa*.

PRESSURE = 1600.00 kPa (abs)						TEMP
V	H	S	Cp	Cp/Cv	v_s	°C
0.00094	284.5	1.2759	1.6468	1.6959	351.6	57.88
0.01215	426.5	1.7050	1.3227	1.4142	132.8	57.88
0.01239	429.3	1.7134	1.2953	1.3888	134.7	60
0.01294	435.6	1.7323	1.2448	1.3412	138.7	65
0.01344	441.7	1.7503	1.2083	1.3056	142.3	70
0.01392	447.7	1.7675	1.1811	1.2779	145.6	75
0.01437	453.6	1.7842	1.1604	1.2556	148.7	80
0.01480	459.3	1.8004	1.1447	1.2373	151.5	85
0.01522	465.0	1.8162	1.1325	1.2220	154.2	90
0.01562	470.6	1.8316	1.1233	1.2090	156.8	95
0.01602	476.2	1.8467	1.1163	1.1978	159.2	100
0.01640	481.8	1.8616	1.1112	1.1881	161.5	105
0.01677	487.4	1.8761	1.1077	1.1796	163.7	110
0.01714	492.9	1.8905	1.1054	1.1721	165.9	115
0.01750	498.4	1.9046	1.1042	1.1653	167.9	120
0.01785	503.9	1.9186	1.1038	1.1593	169.9	125
0.01820	509.5	1.9323	1.1042	1.1539	171.8	130
0.01854	515.0	1.9460	1.1053	1.1489	173.7	135
0.01887	520.5	1.9594	1.1069	1.1444	175.5	140
0.01921	526.0	1.9728	1.1090	1.1403	177.3	145
0.01954	531.6	1.9860	1.1115	1.1365	179.0	150
0.01986	537.2	1.9990	1.1144	1.1330	180.7	155
0.02018	542.7	2.0120	1.1176	1.1298	182.4	160
0.02050	548.3	2.0248	1.1211	1.1268	184.0	165
0.02082	554.0	2.0376	1.1248	1.1240	185.5	170
0.02113	559.6	2.0502	1.1287	1.1214	187.1	175
0.02144	565.2	2.0627	1.1328	1.1190	188.6	180
0.02175	570.9	2.0752	1.1370	1.1167	190.1	185
0.02206	576.6	2.0876	1.1414	1.1145	191.6	190
0.02236	582.3	2.0998	1.1458	1.1125	193.1	195
0.02267	588.1	2.1121	1.1504	1.1106	194.5	200
0.02297	593.8	2.1242	1.1551	1.1088	195.9	205
0.02327	599.6	2.1362	1.1598	1.1070	197.3	210

Figure A.5: R134a refrigerant properties: constant pressure table (superheated refrigerant table) at 1600 kPa (16 bar)

B

ADDITIONAL RESULTS

Additional results belonging to the thermodynamic cycle of the vapour cycle system are presented below including pressure-enthalpy and temperature-entropy diagrams. Regarding the flight mission report profile data a summary of mission related parameters is presented together with the mach variation with mission timeline as well as the total propulsive power variation.

B.1. THERMODYNAMIC ANALYSIS OF SIMPLE VCS

For a simple VCS cycle equipped with a non isentropic compressor, the resulting p-h diagram is presented in Figure B.1 and the T-s diagram is presented in Figure B.2.

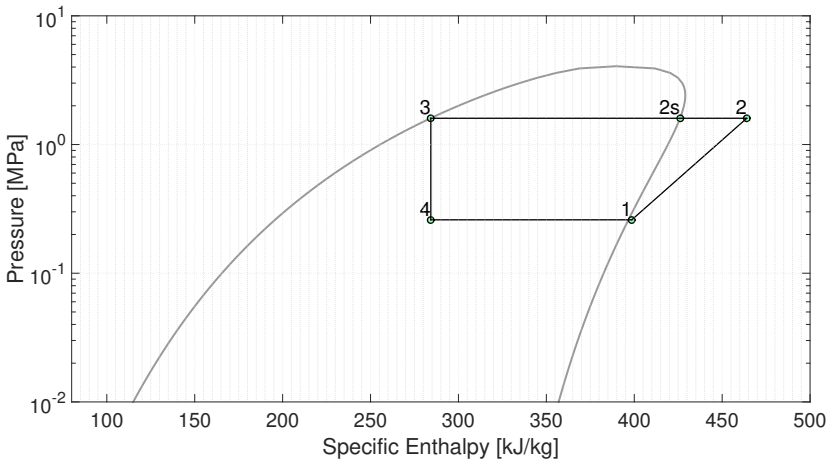

Figure B.1: Pressure-enthalpy diagram for a simple VCS with evaporation temperature of 0° Celsius and condensation temperature of 58° Celsius (with compressor isentropic efficiency 75%) h_2 = 464 kJ/kg

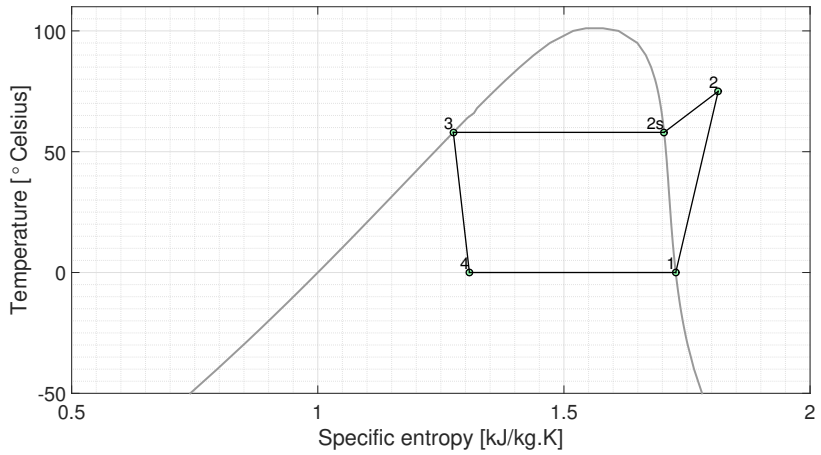

Figure B.2: Temperature-entropy diagram for a simple VCS with evaporation temperature of 0° Celsius and condensation temperature of 58° Celsius (with compressor isentropic efficiency 75%)

B.2. FLIGHT MISSION PROFILE DATA

The data belonging to the defined mission used to generate the flight mission report is summarised in Table B.1. The aim is to apply the same mission to both the baseline model and technology demonstrator, facilitating an unbiased estimation of trip fuel impact for both architectures. The mach variation with mission time is presented in Figure B.3 while the total propulsive power variation is presented in Figure B.4.

Table B.1: Mission profile parameters summary

Parameter	Unit	Value
Takeoff weight	kg	73500
Payload	kg	12000
$N_{pax} + N_{crew}$	-	180+6
Range	nm	1000
Cruise altitude	ft	35000
Cruise speed	Mach	0.78

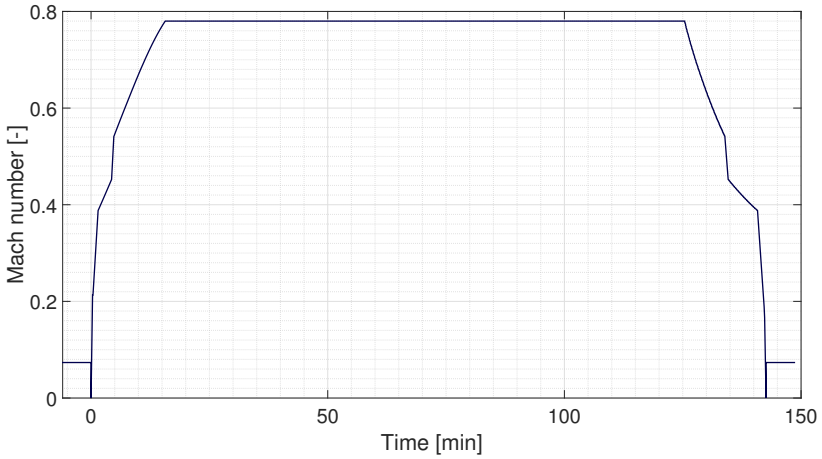

Figure B.3: Mach number variation with time

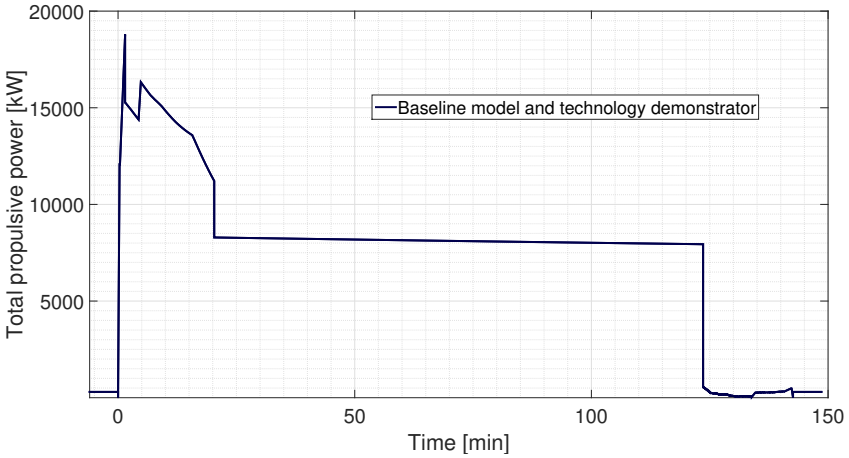

Figure B.4: Total propulsive power variation with time

C

REFERENCE DATA REFRIGERANT COMPRESSORS

Refrigerant compressors can be classified as either rotary, reciprocating or centrifugal. Rotary compressors can be further classified as screw, scroll or vane. A summary of performance related parameters for a selection of parameters identified part of the literature study is presented in Table C.1, followed by a number of miniature centrifugal compressors maps. The potential weight savings of miniature centrifugal compressors can be appreciated by looking at the compressor data in the fifth column of Table C.1, showing a compressor weight of 0.5 kg which is approximately fifty times lower than a comparable scroll compressor.

Table C.1: Reference data compressors (miniature and small scale)

	Compressor				
	1 [78] (2009)	2 [80] (2006)	3 [81] (2002)	4 [21] (2013)	5 [22] (2012)
Application/ working fluid	Air	R134a, 100g	R134a	R600	Air
Compressor type	centrifugal	rotary	rotary	centrifugal	centrifugal
System configuration	2 stage	-	-	1 stage	-
N (krpm)	500	2-3.5	-	250	250
$\dot{m}$ (g/s)	1	0.8-1.7	-	2.5	11.4
PR (-)	2.25	1.9-3.2	3.1-3.6	1.5	1.5
Inlet volume flow rate (m^3/s)	-	-	-	-	-
Isentropic enthalpy rise (kJ/kg)	-	-	-	-	-
Compressor maximum power consumption (W)	350	103	7-22	-	-
Compressor design cooling capacity (W)	-	75-140	130	-	-
Diameter (mm)	35	85	64	21	21
Weight compressor (kg)	0.14	-	1.36	-	0.6
Weight cooling unit (kg)	-	-	-	-	-
Efficiency (%)	74	-	-	65, in air	-
Condenser air flow rate (g/s)	-	-	10-15	-	-
COP	-	3-5.5	2.2-5.8	-	-

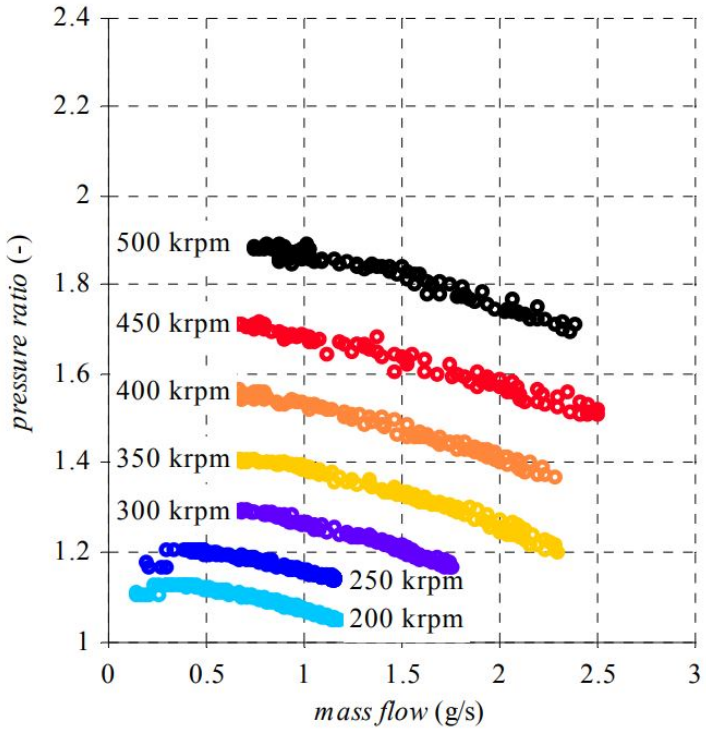

Figure C.1: Compressor map for dual stage miniature centrifugal compressor with impeller diameter of 35mm, corresponding to Compressor #1 from Table C.1, copied from Krahenbuhl et al. [21]

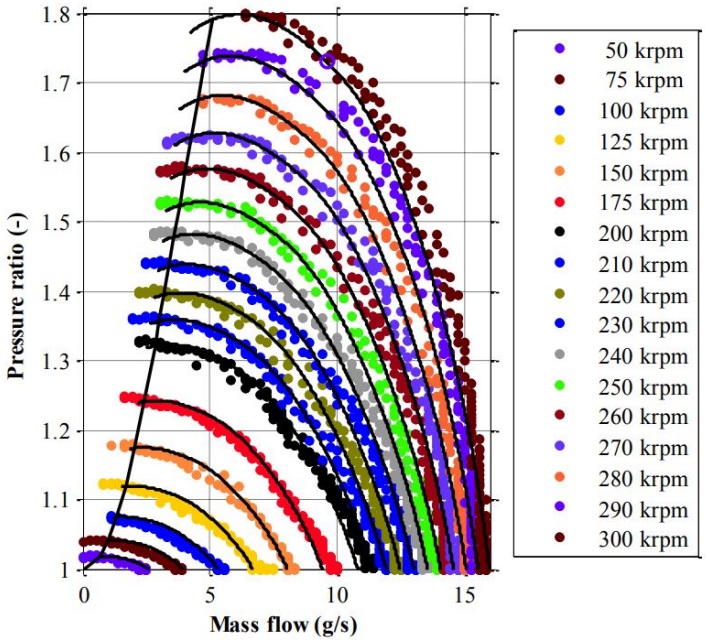

Figure C.2: Compressor map for single stage miniature centrifugal compressor with impeller diameter of 21mm, corresponding to Compressor #4 from Table C.1, copied from Casey et al. [21]

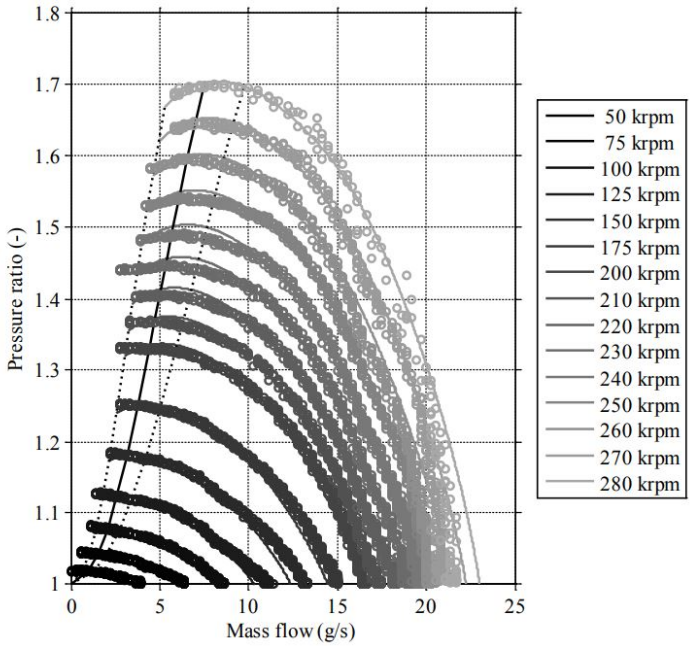

Figure C.3: Compressor map for single stage miniature centrifugal compressor with impeller diameter of 21mm, corresponding to Compressor #5 from Table C.1, copied from Zhao et al. [22]

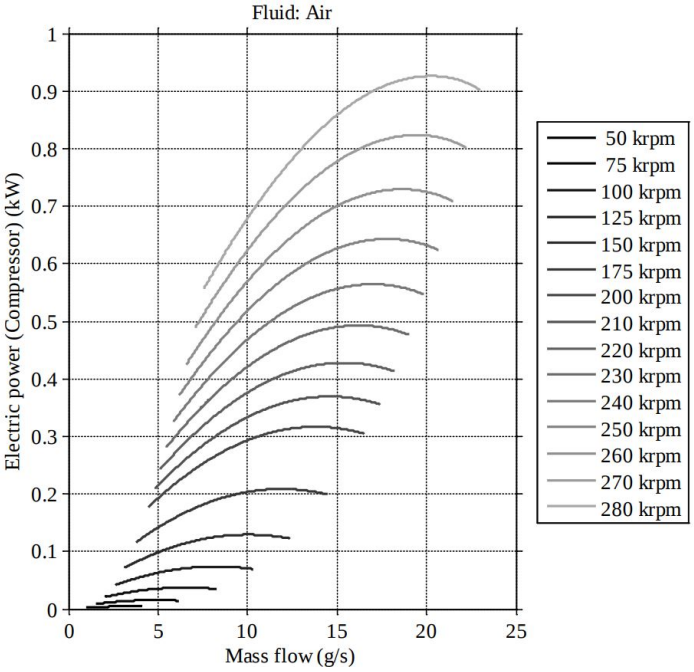

Figure C.4: Power map for single stage miniature centrifugal compressor with impeller diameter of 21mm, corresponding to Compressor #5 from Table C.1, copied from Zhao et al. [22]

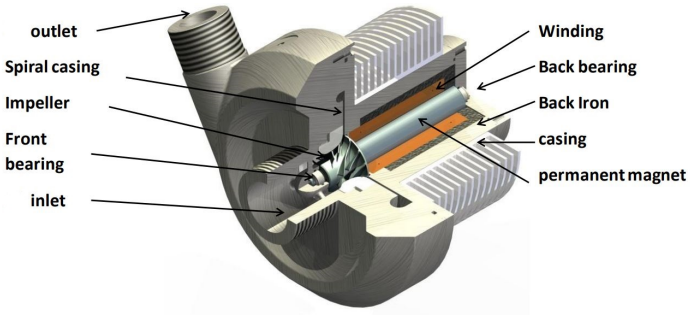

Figure C.5: Centrifugal compressor assembly [21]

Figure C.6: Impeller with diameter of 21 mm and length of 69 mm [21]

An example of a scroll compressor for vapour cycle systems is shown in Figure C.7 [1]. Manufactured by Enviro Systems, this compressor is rated at 20,500 BTU/h (6 kW) and weighs 29.5 lbs (13.4 kg). The suction pressure is 38 PSIG (262 kPa) and the discharge pressure is 220 PSIG (1516 kPa), resulting in a pressure ratio of 5.8.

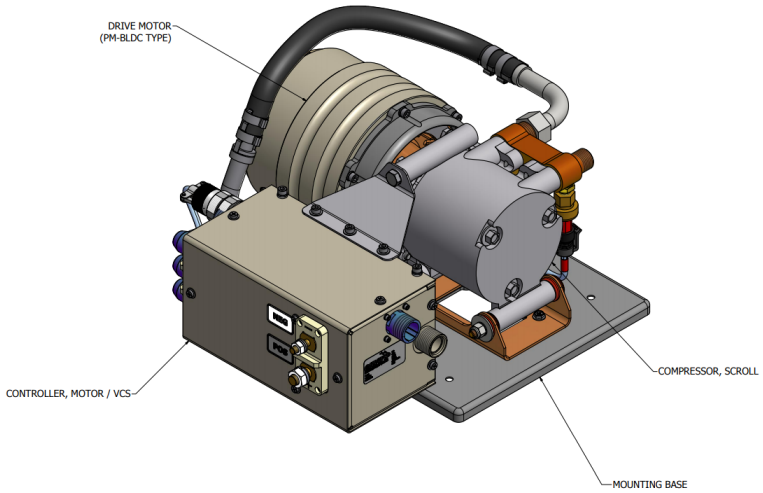

UNIT DESIGN SPECIFICATIONS	
RATED CAPACITY	20,500 BTUH
COMPRESSOR TYPE	INVOLUTE SCROLL COMPRESSOR
COMPRESSOR	60 CC/REV.
REFRIGERANT	R134a
DISCHARGE PRESSURE	220 PSIG (NOM.) @ 105°F O.A.T.
SUCTION PRESSURE	38 PSIG (NOM.) @ 105°F O.A.T.
VOLTAGE	28 VDC
RATED CURRENT	125 AMPS (NOM.) @ 105°F O.A.T.
CURRENT LIMIT	135 AMPS MAX
ALTITUDE	(-)1000 TO 51,000 FT
AMBIENT ENVIRONMENT	(-)67°F TO 165°F
OPERATION	CONTINUOUS
WEIGHT	29.5 LBS. MAX (VENTED)

Figure C.7: Scroll compressor assembly and specifications

[1] URL http://www.enviro-ok.com/wp-content/uploads/Product%20PDFs/3%20Vapor%20Cycle%20Components/1133910-CAT.pdf [cited July 1, 2019]

D

REFERENCE DATA APPLICATIONS OF VAPOUR CYCLE SYSTEMS IN AIRCRAFT

A summary of vapour cycle system applications for naval aircraft is presented in Table D.1. The applications are aimed at either cabin or avionics temperature control, with different types of compressors used including screw, centrifugal and piston compressors.

Table D.1: Vapour cycle systems applications, data adapted from Springer and Delson [24]

Platform	Application	Refrigerant type	Refrigerant quantity (kg)	Cooling capacity (W)	System/ Compressor manufacturer	Compressor type
1. VH-60N	Cabin	R500/R134a	2.7	15.2k	Aero Aire	Rotating vane
2. VH-3D	Cabin	R12/R134a	5.9	21.1k	Fairchild	Helical-rotary (screw)
3. VH-3A	Cabin	R12/R134a	3.7	18.0k	Aero Aire	Rotating vane
4. E-2C	Avionics	R114/R134a	13.2	45.7k	AlliedSignal	Centrifugal
5. TH-57	Cabin	R12/R134a	1.4	8.7k	Keith Products	Piston
6. ES-3A	Avionics	R12/R134a	9.5	21.1k	Parker-Hannifin	Rotating vane
7. EC-24A	Avionics	R12/R134a	13.2	103k	Carrier	Centrifugal
8. C-12	Cabin	R12/R134a	4.3	9.37k	Frigidaire or Harrison Radiator	Piston
9. T-34C	Cabin	R12/R134a	1.4	7.03k	Abacus International	Piston
10. T-44	Cabin	R12/R134a	1.8	4.69k	Borg-Warner	Piston

E

SYSARC KNOWLEDGE DESIGNER

Defining new EO Concepts in Sysarc Knowledge Designer is not a trivial task. In this appendix several difficulties encountered while setting up the EO Concept ECSPackVCS are described. Other aspects covered are the argument notation, heat transfer methods and multi dimensional tables definition.

E.1. POSITIONING EO CONCEPTS

By default after defining the ECSPackVCS EO Concept as a function of the IECSPackVCS Category, adding it to the project file in Engineering Workbench will not automatically position it under the Pneumatic node, although it was defined under the Pneumatic node in Sysarc. The additional step to position it under the Pneumatic node is to open the EO Family Components_Pneumatic under the SysArcDataStructure and add the IECSPackVCS category to the Addable Item Types in the Component List accessable through the properties view. By default only the category IPneumaticComponent is added, thus only EO Concepts inheriting from this EO Category initally appear under the Pneumatic node. Figure E.1 presents the location of the Pneumatic assembly accessable through the Knowledge Designer.

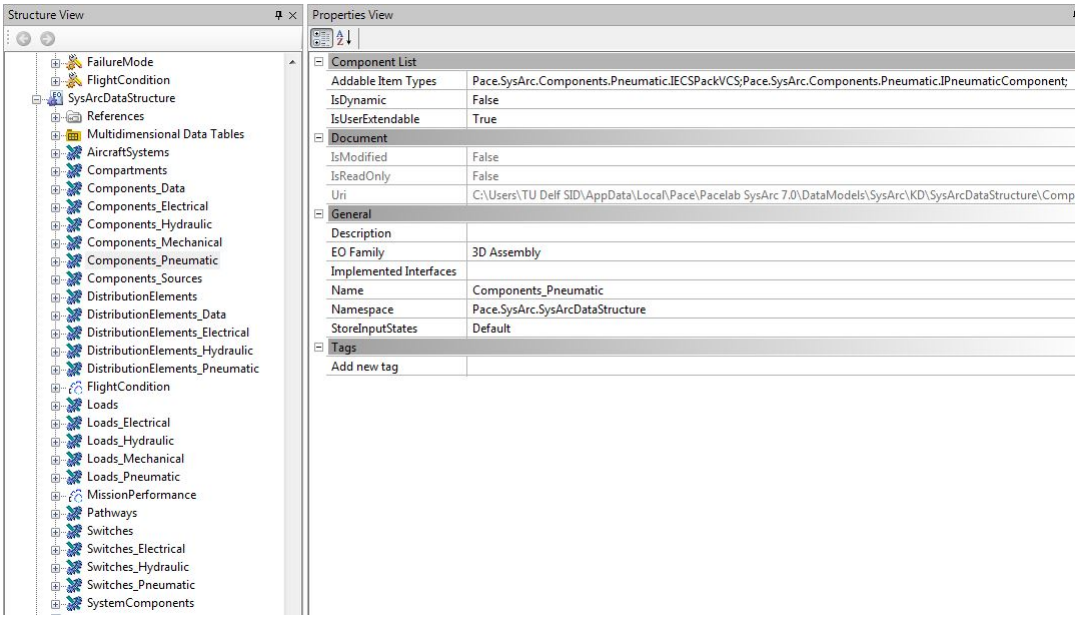

Figure E.1: Components_Pneumatic accessable through SysArcDataStructure

E.2. ARGUMENT NOTATION: METHOD VS FUNCTION

When defining a method in Sysarc the name of the arguments have to be different than those of the function in order to avoid confusion. Then the following question comes in mind: when calling the method in a function, how should the order of arguments be in order for the formula to activate the method in the desired way? When defining a method, the arguments and their type need to be added manually. Consider the method CalcNTU shown in Figures E.2 and E.3. It can be seen that the order of the arguments defined manually does not match the order in which they appear in the method. This does not affect in any way how the method function. The trick is to define them in the same order when calling the method through the

function of the **HXNTUFormula**, in the form of **CalcNTU**(HXOverallHeatTransferCoefficient, HXHeatTransferArea, HXPackHeatCapacityRate, HXCoolantHeatCapacityRate). The function will associate its arguments to those of the method in the order shown in Table E.1.

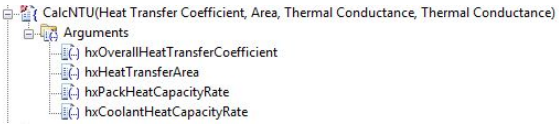

Figure E.2: CalcNTU method arguments

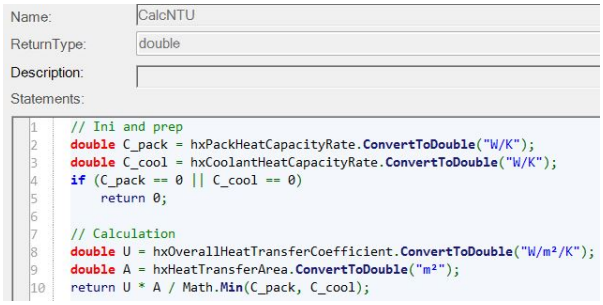

Figure E.3: CalcNTU method statements

Table E.1: Matching arguments between method and function

Method argument	Function argument
hxOverallHeatTransferCoefficient	HXOverallHeatTransferCoefficient
hxHeatTransferArea	HXHeatTransferArea
hxPackHeatCapacityRate	HXPackHeatCapacityRate
hxCoolantHeatCapacityRate	HXCoolantHeatCapacityRate

E.3. HEAT TRANSFER METHODS

Heat transfer between the refrigerant and the cooling air is quantified in Sysarc as the parameter HXHeatTransfered, defined by the formula HXHeatTransferedFormula which calls the method CalcHeatTransferred. The variables appearing in parenthesis represent the arguments of the function and of the method respectively. The methodology for computing the heat transfer in the condenser is summarised in Table E.2.

Table E.2: Method to compute HXHeatTransfered

Parameter	HXHeatTransfered
Formula's name	HXHeatTransferedFormula
Formula's function	CalcHeatTransferred(HXPackHeatCapacityRate, HXCoolantHeatCapacityRate, HXPackEntryTemperature, HXCoolantEntryTemperature, HXEffectiveness)
Method	

```
1  // Ini and prep
2  double C_pack = hxPackHeatCapacityRate.ConvertToDouble("W/K");
3  double C_cool = hxCoolantHeatCapacityRate.ConvertToDouble("W/K")
       ;
4  double T_pack = packTemperature.ConvertToDouble("K");
5  double T_cool = coolantTemperature.ConvertToDouble("K");
6
7  // Calc and check
8  double Q = Math.Min(C_pack, C_cool) * (T_pack - T_cool) *
       effectiveness.ConvertToDouble("");
9
10 // Return
11 return new Power(Q, "W");
```

Table E.3: Method to compute HXPackHeatCapacityRate

Parameter	HXPackHeatCapacityRate
Formula's name	HXPackHeatCapacityRateFormula
Formula's function	CalcHeatCapacityRate(InPack.FlowRate, HXPackEntryTemperature)
Method	

```
1  // Ini
2  double mcp = 0;
3
4  //
5  if (flowRate.Value > 0)
6  {
7          double cp = Pace.Atmosphere.Air.
               CalcMassicHeatCapacityAtConstantPressure(temperature
               ).ConvertToDouble("J/kg/K");
8          mcp = flowRate.ConvertToDouble("kg/s") * cp;
9  }
10
11 // Return
12 return new ThermalConductance(mcp, "W/K");
```

Table E.4: Method to compute HXCoolantHeatCapacityRate

Parameter	HXCoolantHeatCapacityRate
Formula's name	HXCoolantHeatCapacityRateFormula
Formula's function	CalcHeatCapacityRate(InCoolant.FlowRate, HXCoolantEntryTemperature)
Method	

```
1  // Ini
2  double mcp = 0;
3
4  //
5  if (flowRate.Value > 0)
6  {
7          double cp = Pace.Atmosphere.Air.
               CalcMassicHeatCapacityAtConstantPressure(temperature
               ).ConvertToDouble("J/kg/K");
8          mcp = flowRate.ConvertToDouble("kg/s") * cp;
9  }
10
11 // Return
12 return new ThermalConductance(mcp, "W/K");
```

E.4. CALCULATIONS OF SPECIFIC ENTHALPY OF SATURATED FLUID (HF) AND GAS (HG)

Table E.5: Formula used to compute specific enthalpy at evaporation dew point (h1s)

Parameter	h1s
Associated formula	h1sformula
Formula's function	CalcMassicEnthalpy(navigator.SelectEOParam<MDTValue>("/AircraftSystems/@R134a_hg"),Liquid,T1s)

Table E.6: Formula used to compute specific enthalpy at condensation dew point (h2s)

Parameter	h2s
Associated formula	h2sformula
Formula's function	CalcMassicEnthalpy(navigator.SelectEOParam<MDTValue>("/AircraftSystems/@R134a_hg"),Liquid,T2s)

Table E.7: Formula used to compute specific enthalpy at condensation bubble point (h3s)

Parameter	h3s
Associated formula	h3sformula
Formula's function	CalcMassicEnthalpy(navigator.SelectEOParam<MDTValue>("/AircraftSystems/@R134a_hf"),Liquid,T3s)

Table E.8: Method used to compute massic enthalpy of refrigerant

Method

```
1  // Ini and prep
2
3  MassicEnthalpy hg = new MassicEnthalpy(200, "kJ/kg");
4
5  //Check
6  if (liquidProperties.IsDefinedAndHasRows())
7  {
8          if (liquidProperties.MDT.InputValues[0].Cast<string>().
               Contains(liquid))
9                  hg = liquidProperties.MDT.GetOutputByParams(
                       liquid, temperature)[0] as MassicEnthalpy;
10         else
11                 this.GetEOInstancesProject().
                       MessageAndErrorHandlingService.Add("The '
                       LiquidProperties'-Database does not contain
                       a liquid called '" + liquid + "' at '"+this.
                       GetEOInstancesProject().EONavigationService.
                       GetID(this)+"' !", ErrorLevel.Error);
12 }
13
14 //Return
15
16 return hg;
```

BIBLIOGRAPHY

[1] R. Slingerland and S. Zandstra, *Bleed air versus electric power off-takes from a turbofan gas turbine over the flight cycle,* 7^{th} AIAA Aviation Technology, Integration and Operations Conference, Paper nr. AIAA 2007-7848 , pp. 1–12 (September 2007).

[2] I. Moir and A. Seabridge, *Aircraft Systems: Mechanical, Electrical and Avionics Subsystems Integration*, 3rd ed. (John Wiley & Sons, 2008).

[3] I. Chakraborty and D. N. Mavris, *Assessing impact of epistemic and technological uncertainty on aircraft subsystem architectures,* Journal of Aircraft, Vol. 54, Nr. 4, pp. 757–758 (July-August 2017).

[4] V. Madonna, P. Giangrande, and M. Galea, *Electrical power generation in aircraft: Review, challenges and opportunities,* IEEE TRANSACTIONS ON TRANSPORTATION ELECTRIFICATION, Vol. 4, Nr. 3, pp. 646–659 (September 2018).

[5] M. Sielemann, T. Giese, B. Öhler, and M. Otter, *A flexible toolkit for the design of environmental control system architectures,* Proceedings of the First CEAS European Air and Space Conference, Berlin , pp. 1–10 (January 2007).

[6] C. L. Dwight and H. J. Sauer, *Engineering Thermodynamics*, SI ed. (Van Nostrand Reinhold International Co. Ltd, 1988).

[7] Y. M. Shustrov, *Specific features of high pressure water separation in aircraft environmental control systems,* 24^{th} INTERNATIONAL CONGRESS OF THE AERONAUTICAL SCIENCES , pp. 1–5 (2004).

[8] L. Chen, X. Zhang, C. Wang, and C. Yang, *Analysis on high-pressure water separator,* 9^{th} International Symposium on Heating, Ventilation and Air Conditioning (ISHVAC) and the third International Conference on Building Energy and Environment (COBEE) , pp. 558–566 (July 2015).

[9] D. M., *The Standard Handbook of Aeronautical and Astronautical Engineers* (Mcgraw-Hill Education Professional, 2003).

[10] G. Warwick, *Boeing 777 The inside story,* Flight International , p. 33 (December 1991 - January 1992).

[11] H. Yang, X. Zhang, C. Wang, and C. Yang, *Experimental and theoretical study on a novel energy saving ECS for commercial airliners,* Journal of Applied Thermal Engineering, Vol. 127, pp. 1372–1381 (December 2017).

[12] B. Neese, *Aircraft Environmental Control Systems* (Endeavor Books, 1999).

[13] M. Koerner, A. MacKnight, S. Nikbin, M. Quan, and D. R. Robles, *Integrated air and vapor cycle cooling system,* US Patent 2017/0057641 A1 (March 2017).

[14] R. S. Figliola, R. Tipton, and H. Li, *Exergy approach to decision-based design of integrated aircraft thermal systems,* Journal of Aircraft, Vol. 40, Nr. 1, pp. 49–55 (January-February 2003).

[15] C. Park, H. Lee, Y. Hwang, and R. Radermacher, *Recent advances in vapor compression cycle technologies,* International Journal of Refrigeration, Vol. 60, pp. 118–134 (December 2015).

[16] W. S. Comstock, M. S. Owen, and H. E. Kennedy, *ASHRAE Handbook Fundamentals* (ASHRAE, 2017).

[17] S. Baakeem, J. Orfi, and A. Alabdulkarem, *Optimization of a multistage vapor-compression refrigeration system for various refrigerants,* Journal of Applied Thermal Engineering, Vol. 136, pp. 84–96 (May 2018).

[18] D. Han, L. Hao, and J. Yang, *Dynamic characteristics of air cycle machine rotor system,* Journal of Shock and Vibration Vol. 2018, pp. 1–16 (September 2018).

[19] M. Shi, I. Chakraborty, and J. Tai, *Integrated gas turbine and environmental control system pack sizing and analysis,* AIAA SciTech Forum, Paper nr. AIAA 2018-1748 , pp. 1–29 (January 2018).

[20] J. Zamboni, *A Method For The Conceptual Design Of Hybrid Electric Aircraft* (Delft University of Technology, 2018).

[21] M. V. Casey, D. Krahenbuhl, and C. Zwyssig, *The design of ultra-high-speed miniature centrifugal compressors,* European Conference on Turbomachinery Fluid Dynamics and Thermodynamics, Paper nr. ETC2013-004 , pp. 1–13 (April 2013).

[22] D. Zhao, D. Krähenbühl, B. Blunier, C. Zwyssig, M. Dou, and A. Miraoui, *Design and control of an ultra high speed turbo compressor for the air management of fuel cell systems,* Transportation Electrification Conference and Expo (ITEC), Paper nr. ETC2013-004 , pp. 1–6 (July 2012).

[23] C. Long, Z. Xingjuan, and Y. Chunxin, *A new concept environmental control system with energy recovery considerations for commercial aircraft,* 44^{th} International Conference on Environmental Systems, Paper nr. ICES-2014-099 , pp. 1–10 (July 2014).

[24] T. A. Springer and L. Delson, *Retrofit of u.s. navy aircraft vapor cycle systems to accommodate non-cfc-based refrigerants,* SAE Transactions Vol. 104, pp. 405–412 (1995).

[25] J. Eichler, *Simulation study of an aircraft's environmental control system dynamic response,* Journal of Aircraft, Vol. 12, Nr. 10, pp. 757–758 (October 1975).

[26] M. Darecki, C. Edelstenne, T. Enders, E. Fernandez, P. Hartman, J. P. Harteman, M. Kerkloh, I. King, P. Ky, M. Mathieu, G. Orsi, G. Schotman, C. Smith, and J. D. Worner, *Flightpath 2050 Europe's vision for aviation,* Report of the High Level Group on Aviation Research, European Commission , pp. 1–28 (2011).

[27] R. I. Jones, *The more electric aircraft - assessing the benefits,* Proceedings of the Institution of Mechanical Engineers, Part G: Journal of Aerospace Engineering, Vol. 216, Nr. 5, pp. 259–269 (May 2002).

[28] S. Liscouet-Hanke, S. Pufe, and J.-C. Mare, *A simulation framework for aircraft power management,* Proceedings of the Institution of Mechanical Engineers, Part G: Journal of Aerospace Engineering, Vol. 222, Nr. 6, pp. 749–756 (September 2008).

[29] I. Moir, A. Seabridge, and M. Jukes, *Civil Avionics Systems,* 2nd ed. (Wiley, 2008).

[30] B. Sarlioglu and C. T. Morris, *More electric aircraft: Review, challenges and opportunities for commercial transport aircraft,* IEEE TRANSACTIONS ON TRANSPORTATION ELECTRIFICATION, Vol. 1, Nr. 1, pp. 54–64 (June 2015).

[31] Z. Zhang, J. Li, Y. Liu, Y. Xu, and Y. Yan, *Overview and development of variable frequency AC generators for more electric aircraft generation systems,* Chinese Journal of Electrical Engineering, Vol. 3, Nr. 2, pp. 32–40 (September 2017).

[32] J. Dollmayer, N. Bundschuh, and U. B. Carl, *Fuel mass penalty due to generators and fuel cells as energy source of the all-electric aircraft,* Journal of Aerospace Science and Technology, Vol. 10, Nr. 8, pp. 686–694 (December 2006).

[33] J. Wei, Q. Zheng, and Y. Yang, *Integrated AC and DC excitation method for brushless synchronous machine,* IEEE Energy Conversion Congress and Exposition (ECCE), Vol. 1, Nr. 1, pp. 2322–2325 (September 2012).

[34] J. Chang and A. Wang, *New vf-power system architecture and evaluation for future aircraft,* IEEE Transactions on Aerospace and Electronic Systems, Vol. 42, Nr. 2, pp. 527–539 (April 2006).

[35] J. C. Ordonez and A. Bejan, *Minimum power requirement for environmental control of aircraft,* Journal of Energy, Vol. 28, Nr. 12, pp. 1183–1202 (October 2003).

[36] D. Bender, *Integration of exergy analysis into model-based design and evaluation of aircraft environmental control systems,* Journal of Energy, Vol. 137, pp. 739–751 (October 2017).

[37] J. R. Davis, R. Johnson, J. Stepanek, and J. A. Fogarty, *Fundamentals of Aerospace Medicine*, 4th ed. (Lippincott Williams & Wilkins, 2008).

[38] H. Zhao, Y. Hou, Y. Zhu, L. Chen, and S. Chen, *Experimental study on the performance of an aircraft environmental control system,* Journal of Applied Thermal Engineering Vol. 29, pp. 3284–3288 (November 2009).

[39] M. A. Jonqueres, *Air cycle environmental control systems with two stage compression and expansion and separate ambiend air fan,* US Patent 6,128,909 (October 2000).

[40] M. J. Cronin, *The prospects and potential of all electric aircraft,* AIAA Aircraft Design, Systems and Technology Meeting, Paper no. AIAA-83-2478 , p. 1 (October 1983).

[41] J. F. Asfia, K. R. Williams, W. A. Atkey, C. J. Fiterman, S. M. Loukusa, and C. Y. Sammamish, *Electric air conditioning system for an aircraft,* US Patent 6,526,775 B1 (March 2003).

[42] M. Sinnet, *787 No-bleed systems: Saving fuel and enhancing operational efficiencies,* Aero Quarterly , pp. 1–6 (Quarter 4 2007).

[43] L. P. Pellegrini, R. Gandolfi, G. A. L. da Silva, and S. Oliveira, *Exergy analysis as a tool for decision making in aircraft systems design,* 45^{th} AIAA Aerospace Sciences Meeting and Exhibit, Paper nr. AIAA 2007-1396 , pp. 1–12 (2007).

[44] A. Santos, C. Andrade, and E. Zaparoli, *A thermodynamic study of air cycle machine for aerospace applications,* International Journal of Thermodynamics, Vol. 17, Nr. 3, pp. 117–126 (September 2014).

[45] A. Bejan, *Advanced Engineering Thermodynamics*, 3rd ed. (John Wiley & Sons, 2006).

[46] G. K. Payne, *Hybrid vapor cycle/air cycle environmental control system,* US Patent 4,963,174 (October 1990).

[47] M. Ghanekar, *Vapor cycle system for the F-22 raptor,* SAE Technical Paper 2000-01-2268 , pp. 1–7 (2000).

[48] T. Michalak, S. Emo, and J. Ervin, *Control strategy for aircraft vapor compression system operation,* International Journal of Refrigeration, Vol. 48, pp. 10–18 (December 2014).

[49] M. J. Moran, H. N. Shapiro, D. D. Boettner, and M. B. Bailey, *Fundamentals of Engineering Thermodynamics*, EIGHT ed. (Wiley, 2014).

[50] M. Preissner, B. Cutler, B. Radermacher, and C. A. Zhang, *Suction line heat exchanger for r134a automotive air-conditioning system,* Proceedings of the International Refrigeration Conference , pp. 289–294 (2000).

[51] S. A. Klein, D. T. Reindl, and K. Brownell, *Refrigeration system performance using liquid-suction heat exchangers,* International Journal of Refrigeration, Vol. 23, pp. 588–596 (December 2000).

[52] S. M. Zubair, *Thermodynamics of a vapor-compression refrigeration cycle with mechanical subcooling,* Journal of Energy, Vol. 19, Nr. 6, pp. 707–715 (June 1994).

[53] J. Winkler, V. Aute, B. Yang, and R. Radermacher, *Potential benefits of thermoelectric element used with air-cooled heat exchangers,* International Refrigeration and Air Conditioning Conference, Paper nr. R091 , pp. 1–9 (2006).

[54] H. J. Huff, D. Lindsay, and R. Radermacher, *Positive displacement compressor and expander simulation,* International Compressor Engineering Conference, Paper nr. C9-2 , pp. 1–8 (2002).

[55] D. Li and E. A. Groll, *Transcritical CO2 refrigeration cycle with ejector expansion device,* International Journal of Refrigeration, Vol. 28, Nr. 5, pp. 766–773 (August 2014).

[56] Z. Q. Wang, N. J. Zhou, J. Guo, and X. Wang, *Fluid selection and parametric optimization of organic Rankine cycle using low temperature waste heat,* Journal of Engineering for Gas Turbines and Power, Vol. 40, Nr. 1, pp. 107–115 (April 2012).

[57] V. W. Bhatkar, V. M. Kriplani, and G. K. Awari, *Alternative refrigerants in vapour compression refrigeration cycle for sustainable environment: a review of recent research,* International Journal of Environment Science and Technology, Vol. 10, Nr. 4, pp. 871–880 (July 2013).

[58] G. Ding, *Recent developments in simulation techniques for vapur-compression refrigeration systems,* International Journal of Refrigeration, Vol. 30, Nr. 7, pp. 1119–1133 (November 2007).

[59] I. R. M. Dominguez, *Correlations for some saturated thermodynamic and transport properties of refrigerant r22,* ASHRAE Transactions , pp. 344–348 (January 1993).

[60] G. L. Ding, Z. Wu, K. Wang, and M. Fukaya, *Extension of the applicable range of the implicit curve-fitting method for refrigerant thermodynamic properties to critical pressure,* International Journal of Refrigeration, Vol. 30, Nr. 3, pp. 418–432 (July 2013).

[61] A. J. Wurmstein, R. Wood, and S. Zarr, *Cabin cruising altitudes for regular transport aircraft,* Aviation Space and Environmental Medicine, Vol. 79, Nr. 4, pp. 433–439 (April 2008).

[62] F. A. A. (FAA), *FAR/AIM 2019: Up-to-Date FAA Regulations / Aeronautical Information Manual (FAR/AIM Federal Aviation Regulations)* (Skyhorse, Skyhorse Publishing, Inc. 307 West 36th Street, 11th Floor New York, 2019).

[63] S. United States. Congress. Senate. Committee on Commerce and T. S. on Aviation, *Airliner cabin safety and health standards* (Washington : U.S. Government Printing Office, Getzville, New York, 1982).

[64] B. Zohuri, *Compact heat exchangers* (Springer, The Boulevard, Langford Lane, Kidlington, Oxford, OX5 1 GB, UK, 2017).

[65] M. A. Boda, S. S. Deshetti, and M. A. Gavade, *Design and development of parallel-counterflow heat exchanger,* International Journal of Innovative Research in Advanced Engineering (IJIRAE), Vol. 4, Nr. 2, pp. 29–35 (February 2017).

[66] R. K. Shah and D. P. Sekulic, *Fundamentals of heat exchanger design* (John Wiley & Sons, Inc., Hoboken, New Jersey, 2003).

[67] M. Prasad, *Refrigeration and Air Conditioning* (New Age International Publishers, 7/30 A, Daryaganj, New Delhi-110002, 2015).

[68] D. Krahenbuhl, C. Zwyssig, H. Weser, and J. W. Kolar, *A miniature 500000 rpm electrically driven compressor,* 2009 IEEE, Paper nr. 10.2514/6.2014-3012 , pp. 3602–3608 (September 2009).

[69] D. M. N. Milewski, *Effect of Electric Environmental Control System Retrofit on Fuel Burn of a Medium-Range Aircraft* (Delft University of Technology, 2019).

[70] D. Scholz, *An optional APU for passenger aircraft,* CEAS 2015 (September 2015).

[71] J. Yu, T. Zhang, and J. Qian, *Electrical Motor Products - International Energy-Efficiency Standards and Testing Methods*, FIRST ed. (Woodhead Publishing, 2011).

[72] B. Iooss and P. Lemaitre, *A review on global sensitivity analysis methods,* Operations Research/Computer Science Interfaces Series, Vol. 59, pp. 101–122 (April 2014).

[73] S. van Haver and R. Vos, *A practical method for uncertainty analysis in the aircraft conceptual design phase,* AIAA SciTech Forum, Paper nr. AIAA 2015-1680 , pp. 1–14 (November 2014).

[74] R. L. Jenkinson, *Civil jet aircraft design* (Elsevier/Butterworth-Heinemann, 1999).

[75] M. Bodie, T. Pamphile, and J. Zumberge, *Air cycle machine for transient model validation,* SAE Technical paper, Paper nr. AIAA 2016-01-2000 , pp. 1–9 (September 2016).

[76] B. L. Messinger, *Refrigeration for air conditioning pressurized transport aircraft,* SAE Technical paper, Paper nr. AIAA 460200 , pp. 93–119 (January 1946).

[77] D. C. Brondum, J. E. Materne, F. Biancardi, and D. Pandy, *High-speed, direct-drive centrifugal compressors for commercial hvac systems,* International Compressor Engineering Conference , pp. 921–926 (1998).

[78] D. Krahenbuhl, C. Zwyssig, H. Weser, and J. W. Kolar, *A miniature, 500 000 rpm, electrically driven turbocompressor,* IEEE Energy Conversion Congress and Exposition , pp. 3602–3608 (September 2009).

[79] C. A. Yunus and M. A. Boles, *Thermodynamics: An Engineering Approach*, eighth ed. (Mcgraw-Hill Education - Europe, 2015).

[80] S. Trutassanawin, E. A. Groll, S. V. Garimella, and L. Cremaschi, *Experimental investigation of a miniature-scale refrigeration system for electronics cooling,* IEEE TRANSACTIONS ON COMPONENTS AND PACKAGING TECHNOLOGIES, Vol. 29, pp. 678–687 (September 2006).

[81] J. G. M. et al., *Thermal management for electronics cooling using a miniature compressor,* Proc. Int. Microelectron. Packag. Soc. (IMAPS) (2002).